STRUCTURE AND BI-MAGNETISM OF NANOCOMPOSITES AND NANOALLOYS SYNTHESIZED BY REDUCTION OF (Co, Ni) Fe_2O_4 NANO-FERRITES

by

Ezekiel Itegbeyogene Patrick

BSc (Hons) (Kogi State University, Nigeria)

Submitted in fulfilment of the academic
requirements for the degree of
Master of Science in the
School of Chemistry and Physics,
University of KwaZulu-Natal
Durban
South Africa

March 2014

Abstract

Structural and magnetic properties of $CoFe_2O_4$, $NiFe_2O_4$ nano-ferrites, $CoFe_2O_4$ /$CoFe_2$, $NiFe_2O_4$/NiFe bi-magnetic nanocomposites and $CoFe_2$, NiFe alloys were studied. The nano-ferrites were synthesised using the glycol-thermal method at 200 °C for 6 hours. The nanocomposites and alloys were produced by the reduction of the ferrites using different amounts of activated charcoal. The reduction reaction was performed at 900 °C for 3 hours in high purity flowing argon atmosphere. Complete reduction yields the alloy phases while partial reduction produces the nanocomposites. The samples were studied using X-ray diffraction (XRD), high resolution transmission electron microscopy (HRTEM), high resolution scanning electron microscopy (HRSEM), ^{57}Fe Mössbauer spectroscopy, LakeShore vibrating sample magnetometer and a mini cryogen free system. XRD measurements of the nano-ferrites showed a single phase spinel structure with average crystallite sizes of about 10 nm. the $CoFe_2$ alloy was obtained at an activated charcoal to ferrite molar ratio $n_C = 6$ while the NiFe alloy was obtained at $n_C = 5$. XRD results of the reduced samples of $NiFe_2O_4$ showed the coexistence of bcc α-Fe and fcc γ-Fe lattice structures for NiFe alloy. The HRTEM and HRSEM measurements of all the reduced samples showed clear differences between the morphology of the parent nano-ferrites and the reduced samples. ^{57}Fe Mössbauer spectra measurements of the reduced samples showed the transformation of the spinel structure to the alloy phase. The presence of mixed phases in the nanocomposites was revealed. A small amount of mixed phase in $CoFe_2$ and NiFe alloys which was not detected by XRD was revealed by Mössbauer measurement for $n_C = 6$ and $n_C = 5$ respectively. The Mössbauer fits showed that Fe^{3+} was reduced to Fe^{2+} with lower magnetic hyperfine fields observed in the reduced samples. High field (50 kOe) magnetization measurements at room temperature for $CoFe_2O_4$/$CoFe_2$ nanocomposite show significant enhancement of saturation magnetization from 63 emu/g of the parent nano-ferrite to 221 emu/g at $n_C = 5$. In the $NiFe_2O_4$/NiFe nanocomposite the in magnetization increased from 57 emu/g to 141 emu/g at $n_C = 6$. Low temperature measurements performed on the nanocomposites exhibited higher magnetizations. The coercivity of the fully reduced samples of the nano-ferrites were observed to be less dependent on temperature.

PREFACE

The experimental work described in this dissertation was carried out in the Condensed Matter Physics Lab, School of Chemistry and Physics, Westville Campus, University of KwaZulu-Natal, Durban from January 2013 to December 2013, under the supervision of Dr. Thomas Moyo.

These studies represent original work by the author and have not otherwise been submitted in any form for any degree or diploma to any tertiary institution. Where use has been made of the work of others it is duly acknowledged in the text.

COLLEGE OF AGRICULTURE, ENGINEERING AND SCIENCE

DECLARATION 1 - PLAGIARISM

I, EZEKIEL ITEGBEYOGENE PATRICK declare that

1. The research reported in this dissertation, except where otherwise indicated, is my original research.

2. This dissertation has not been submitted for any degree or examination at any university.

3. This dissertation does not contain other person's data, pictures, graphs or other information, unless specifically acknowledged as being sourced from other persons.

4. This dissertation does not contain other persons writings, unless specifically acknowledged as being sourced from other researchers. When other written sources have been quoted, then:

5. Their words have been re-written but general information attributed to them has been referenced.

6. Where their exact words have been used, their writing has been placed in italics and inside quotation, and referenced.

7. This dissertation does not contain text, graphics or tables copied and pasted from internet, unless specifically acknowledged, and the source being detailed in the dissertation and in the reference sections.

Signed: .....

COLLEGE OF AGRICULTURE, ENGINEERING AND SCIENCE

DECLARATION 2 - PUBLICATIONS

1. Magnetic properties of $CoFe_2O_4/CoFe_2$ nanocomposites synthesized by activated charcoal in argon atmosphere. Oral presentation at the 58th Annual Conference of the South African Institute of Physics (SAIP). Currently under review. Book of abstract ID 515. **Itegbeyogene P. Ezekiel**, Thomas Moyo and Hafiz M. I. Abdallah.

2. Investigation of phase formation of $(Zn, Mg)_{0.5}Co_{0.5}Fe_2O_4$ nanoferrites, J.Z. Msomi, W.B. Dlamini, T. Moyo, **P. Ezekiel**, Journal of Magnetism and Magnetic Materials, In Press, Corrected Proof, Available online 29 January 2014.

Signed: .....

Dedication

I dedicate this thesis to my most caring and lovely parents Mr Ojiekethe Ezekiel Isaac and Mrs Ojiekethe Bose.

Contents

Acknowledgments

My profound gratitude and appreciation goes to my supervisor Dr. Thomas Moyo who took his time to explain every unclear concept not minding how elementary they might look. You are one in a million. An overwhelming thank you to Dr. Hafiz M. I. Abdallah for providing me footing in this work. Many thanks to Dr J. Z. Msomi for your listening ear, care and support. Thumbs up for Nadir Shams-Aldeen and Wendy Dlamini your encouragement kept me going in my hard times. To Patrick Masina, thanks for your software usage guide. Mr. Pradeep Suthan, thank you for your XRD measuring skills which gave me speed in my study.

To my siblings, I could not have asked for more. God bless you for being there right from the foundation of this journey. To my dearest supporters, Mr and Mrs Dele, Mr and Mrs Okita, Mr and Mrs Aminu. God bless you all. Many thanks to Olakunle Ogunjobi for the foundational role you played in this programme. To Oshoja Gilbert, how can I ever repay you for your sacrifices? I owe you so much and thank you. And to my well wishers; Pastor John Praise, Elvis, Francis, Godson, Jennifer to mention a few, thank you. My beloved Nelly Abu thank you for all the moments that you strengthened me with your words and love. God bless you all including all my family members and friends not mentioned here.

I thank the National Research Foundation (NRF) of South Africa for providing the resources for magnetization measurements in the Condensed Matter Physics Lab at Westville Campus. I am also grateful for the opportunity to use the HRTEM and HRSEM facility at the Electron Microscopy Unit, Westville campus. Thanks to the National Center for Technology Management Nigeria for granting me study leave.

List of Figures

List of Tables

Chapter 1

Introduction

1.1 Ferrites

Ferrite is derived from the Latin word *ferrum* meaning iron. The term was first used in the 20^{th} century [1]. Iron-containing materials such as iron oxides known as magnetite (Fe_3O_4) were found to be naturally magnetic. Ferrites can be defined as ceramic magnetic oxides consisting of ferric ions as the main constituent. Generally, they consist of three crystal types namely; spinel, garnet and magnetoplumbite. While garnets can accommodate trivalent elements such as Sm, Gd, Tm and Lu with twelve atoms of oxygen, magnetoplumbites have up to nineteen atoms of oxygen for one molecule of the ferrite [2]. However, our emphasis shall be on the spinel crytal type because of current intense research interest with promising and viable possible applications. Spinels possess the cubic spinel structure with a general formula of AFe_2O_4 where A could be one or more elements such as Co, Ni, Fe, Cu, Mn, Mg and Zn [3, 4]. An example is $CoFe_2O_4$ and $MgZnCoFe_2O_4$ ferrites. The diverse combination of metallic elements in the structure even at nano-scale level provides novel magnetic and electrical properties which make spinels attractive for practical technological applications. These unique properties derived at nano-scale level rest on a number of factors such as elemental composition, cationic distribution, particle size, synthesis method and phase composition. In the absence of the intermediary oxygen atoms metallic alloy phases can form. A combination of the ferrite phase and its alloy phases form bi-magnetic nanocomposites which usually have enhanced

properties. This chapter gives a brief explanation of the spinel ferrites structure, diverse synthesis methods and magnetic properties of ferrites. Possible applications of ferrites and their bi-magnetic nanocomposites are discussed and conclude the chapter with the dissertation outline for the present work.

1.1.1 Spinel structure of ferrites

The cubic spinel structure of ferrites has a unit cell consisting of 8 smaller cubes known as octants as shown in Figure 1.1. It has 32 oxygen anions, 16 trivalent and 8 divalent metal cations [2]. The 32 oxygen ions forms a face centred cubic (fcc) lattice with the existence of two kinds of interstitial sites namely; tetrahedral A-sites surrounded by 4 oxygen atoms and octahedral B-sites surrounded by 6 oxygen atoms. There are 64 of such A-sites of which 8 are occupied by the divalent metal ions and 32 B-sites of which 16 are occupied by the trivalent cations [5]. The magnetic and electrical properties of spinel ferrites are determined by the structural distribution of metal ions in the A- and B-sites. The distribution of these ions is influenced by the synthesis method and temperature. The structure can follow a number of possible distributions generally represented by $A^{2+}_{\gamma}\ Fe^{3+}_{1-\gamma}\ [A^{2+}_{1-\gamma}\ Fe^{3+}_{1+\gamma}]O_4$ where γ is known as the limiting case [2]. The ions in brackets are located at B-sites while the ions outside the bracket are located in A-sites. When the limiting case γ is 1, the spinel is known as normal spinel. When it is 0, it is known as inverse spinel. However, there are cases of random distribution of the divalent and trivalent ions over both A- and B-sites where γ has intermediate values. These are known as mixed spinels [2]. Hence, the mixed spinel ferrites are usually considered as intermediate between extreme cases of normal and inverse spinel ferrites. Structural and experimental factors have been reported that influence the coordination preference of divalent and trivalent metal ions in spinel crystals [6]. Since not all the sites are filled with either the divalent or trivalent metal ions, spinels usually have their tetrahedral sites occupied by divalent ions and the octahedral sites occupied by trivalent ions with a total positive charge of +64 needed to balance the negative charge of -64 for oxygen ions. This make the structure electrically neutral [7]. $CoFe_2O_4$ and $NiFe_2O_4$ ferrites are typical examples of inverse spinel structure [8].

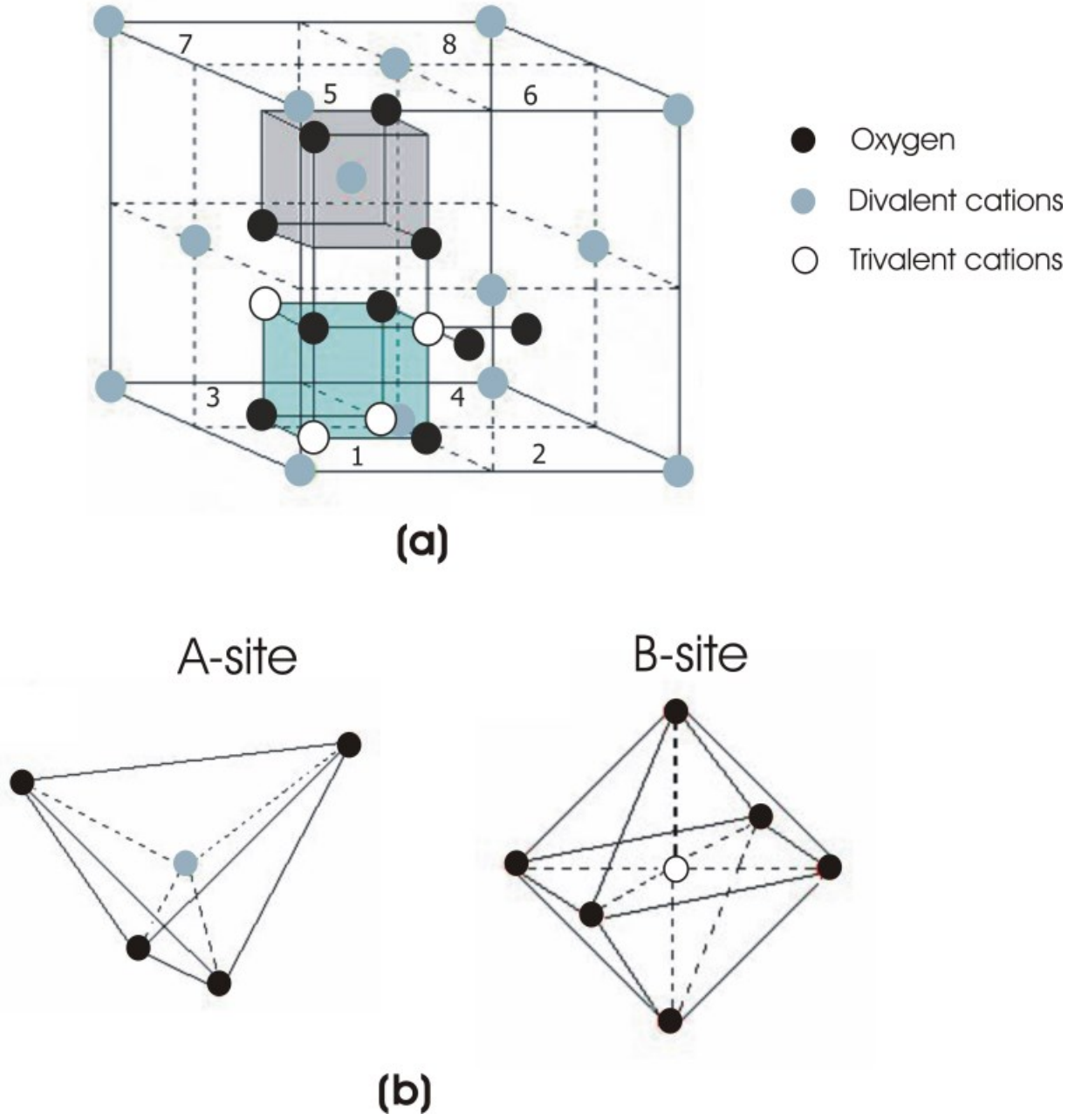

Figure 1.1: Spinel unit cell structure [6, 9].

1.1.2 Synthesis of ferrites

The synthesis method of bulk and nano-structured ferrites is key in determining the structural, magnetic and electrical properties. Bulk ferrites have been conventionally synthesized by solid state reaction technique where the raw materials are usually oxides or carbonates of the required ferrites. The precursors materials require rigorous mixing usually done by hand grinding, turbine blade or high energy planetary ball milling to form a homogeneous mixture. This technique requires prolonged annealing time at relatively high temperature because of the slow diffusional process of atoms [10]. This causes some loss of control over the morphology and chemical composition of the final product. Possible contamination of the samples is also inevitable as a result of mechanical wear and tear of the mixing parts. Hence there may be some level of inconsistencies in the properties of the samples. Wet chemical synthesis methods such as glycol-thermal, hydro-thermal, sol-gel and co-precipitation [11] have been pioneered in recent times and are now widely used. This techniques involve chemical reactions of atoms or molecules in an appropriate solvent media and good crystalline samples can be formed at relatively low temperatures. The wet chemistry methods have been proven to be advantageous over the solid state reaction for the synthesis of the transition metals ferrites as they provide better control of the morphology and particle size of the samples with negligible amount of impurities. The relative flexibility of these techniques allows the fine tuning of the required properties such as saturation magnetization, coercivity, permeability, biocompatibility, electrical resistivity and thermal resistivity for potential technological applications [12]. The glycol-thermal synthesis method was used in the present work and its details are given in Chapter 3.

1.1.3 Magnetic properties of ferrites

The magnetic properties of materials are essentially generated by magnetic moments of electrons in incomplete shells of atoms due to unpaired or net d electrons. Uncompensated spins create net magnetic moments responsible for magnetism as illustrated in Table 1.1. The electrons possess intrinsic spin and are paired in atomic

Table 1.1: Unbalanced magnetic spins [5].

	K	**Ca**	**Sc**	**Ti**	**V**	**Cr**	**Mn**	**Fe**	**Co**	**Ni**	**Cu**	**Zn**
4s	↑	↑↓	↑↓	↑↓	↑↓	↑	↑↓	↑↓	↑↓	↑↓	↑	↑↓
$3d\uparrow$	-	-	1	2	3	5	5	5	5	5	5	5
$3d\downarrow$	-	-	-	-	-	-	-	1	2	3	5	5
Net $3d\uparrow$	-	-	1	2	3	5	5	4	3	2	0	0

orbits in spin-up or spin-down states. The filled $3d$ elements such as Fe, Co, Ni, Cu and Zn have their $3d$ sub-shells occupied with a net or unpaired electron(s). The other elements only have an incomplete or just complete first sub-shell occupied. The magnetism in ferrites depends on the exchange interaction between magnetic moments on A- and B-sites by the intervening oxygen ions. The interaction is a function of the ionic nature of the metal atoms located at these sites of the spinel structure and their relative positions and angles with the oxygen ions. The interaction is strongest at 180° angular position and where the interatomic distances are the shortest. An ideal spinel has an A-O-B angular positions of about 125° and 154°, where -O- represents the intermediate oxygen ion between the two sites A- and -B [13]. The B-O-B angles are 90° and 125° with one of the B-O distances very large [7]. However, the interaction between moments in the A- and B-sites is strongest compared to the weaker BB interaction. The strong exchange interaction gives rise to ferrimagnetism in ferrites [7]. An extensive discussion of various types of magnetic order in materials is made in Chapter 2.

1.2 Nanocomposites

Nanocomposites are composite materials where one of the phases has a dimension in the manometer range of 0.1-100 nm [14]. They have been reported in recent times to be materials of the 21^{st} century owing to their superior properties that are not found in monolithic microscale composites or convectional composites [15]. Recent progress in enhancing the properties of novel nanostructured materials has

intensified research efforts in producing multi-functional nanomaterials to suit technological applications such energy efficiency, light weight materials, reliability in extreme environment, stable magnetic and electrical properties. Nanocomposites material are basically classified into three categories based on their matrix material namely; ceramic-matrix, metal-matrix and polymer-matrix nanocomposites. The present work deals with ceramic-matrix nanocomposites. The materials can exhibit improved magnetic, optical and electrical properties [16], surface protection properties such as tribological and corrosion resistance. Chemical compound from the oxide, nitride or boride groups form a majority of matrices into which metal ions can form secondary phases. Ferrites are part of the oxide group and their respective metals can be formed into alloys to produce ferrite/alloy nanocomposites with the unique properties arising from both the ferrite and the alloy phase.

1.3 Applications

Ferrites and their alloy nanocomposites are highly promising materials for technological applications in medicine, telecommunications, electronics, aviation, security and environmental remediation. Cobalt ferrite ($CoFe_2O_4$) is a hard ferrimagnetic material with possible applications in high density storage, magnetic resonance imaging, ferrofluid, drug delivery and magneto caloric refrigeration [17]. The alloy $CoFe_2$ is used in magneto-resistive devices [18]. The nanocomposites of $CoFe_2O_4/CoFe_2$ bi-magnet are potential materials for spintronics-based devices in sensor and magnetic random access memories application [19]. Nickel ferrite ($NiFe_2O_4$) is a soft magnetic ferrite which finds applications in areas such as microwave devices, catalysis, photomagnetic materials, gas-sensors and site-specific drug delivery [8]. The invar composition of iron nickel FeNi allows their usage in precision mechanical systems and opto-mechanical engineering application [20]. This is because they exhibit anomalous low thermal expansion. The nanocomposites of $NiFe_2O_4$/NiFe are also promising materials for high frequency applications [21].

1.4 Motivation for present work

The properties of nanomaterials such as magnetic and structural properties have been shown to be dependent on synthesis method [8]. The cationic distribution between the A- and B-sites of spinel ferrites also plays an important role in determining the observed magnetic properties. Ferrites and their alloy nanocomposites will exhibit properties depending on the constituting ferrite and alloy phases. Therefore, in the synthesis of nanocomposites, the properties of the various phases contribute to the overall properties of the final product. Different approaches to synthesis methods and the novel applications have encouraged a great deal of interest with objective of optimizing better understanding of the properties. $CoFe_2O_4$ and $NiFe_2O_4$ ferrites with their nanocomposites and alloys produced from reduction reaction of the ferrites by using activated carbon have not been widely reported. Liete et al [22] reported the synthesis of $CoFe_2O_4$ using hydro-thermal synthesis method and produced $CoFe_2O_4/CoFe_2$ nanocomposites by reduction reaction using activated carbon. The magnetic properties were explored at 300 K and 50 K. $NiFe_2O_4$ reduced by activated carbon has not been reported to the best of our knowledge. Jun et al [23] reported the reduction of $NiFe_2O_4$ using hydrogen gas. The motivation of this work is to use glycol-thermal synthesis method in the synthesis of the ferrites and to use a less expensive and safer reducing agent in order to study the structural and magnetic properties of the nanocomposites and alloys formed. We also intend to make a systematic investigation of the properties as a function of temperature and the ferrite to activated charcoal ratio. In this case the selection of $CoFe_2O_4$ and $NiFe_2O_4$ is an optune choice with significant difference in anisotropies due to Co and Ni ions.

1.5 Dissertation outline

The dissertation comprises of six (6) chapters. Chapter 1 gives a brief introduction to ferrites, its structure, synthesis and magnetic properties. It also introduces nanocomposites and possible applications. Chapter 2 introduces the fundamentals of magnetic order in solids which provides background information for analysis of

the results presented in Chapters 4 and 5. Energy in magnetic materials and magnetic hysteresis loop are also discussed. Chapter 3 provides a brief discussions of the experimental techniques used in this work for synthesis to structural and magnetic characterization of the samples. The results for $CoFe_2O_4$, its nanocomposites and alloy are discussed in Chapter 4. Chapter 5 is devoted to $NiFe_2O_4$, its nanocomposites and alloy. Concluding remarks are presented in Chapter 6.

Chapter 2

Magnetic order in solids

Magnetic moments arising from electrons in atoms are responsible for magnetic properties of materials. This chapter elucidates the theoretical basis of magnetic phenomena. The magnetic ordering pattern formed and the energy of interaction between magnetic moments helps to determine the type of magnetic order that forms.

2.1 Origin of magnetic moment

Following a report by J. J. Thompson in 1903, it was generally known that the source of magnetism in materials was as a result of electrons circulating in atoms [7]. Niels Bohr in 1913 gave an atomic perspective of electrons revolving round the nuclei of atoms in orbits which were assumed to be responsible for magnetic behavior. The motion of an electron in an orbit is assumed to constitute a current *I*. The magnitude of the orbital magnetic moment μ_l associated with the charge -e moving in circular motion with angular frequency ω at an orbital radius of r is given by

$$\mu_l = I\pi r^2 = \frac{-e\omega\pi r^2}{2\pi} = \frac{-e\omega r^2}{2}. \tag{2.1.1}$$

For an electron with mass m_e, the magnitude of the orbital angular momentum $|\vec{l}|$ is given by

$$|\vec{l}| = m_e \omega r^2. \tag{2.1.2}$$

Hence, the orbital magnetic moment $\vec{\mu_l}$ of an electron can be expressed in terms of its angular momentum

$$\vec{\mu_l} = \frac{-e}{2m_e}\vec{l}. \tag{2.1.3}$$

Figure 2.1 shows a diagrammatic representation of the orbital moment $\vec{\mu_l}$ of an electron.

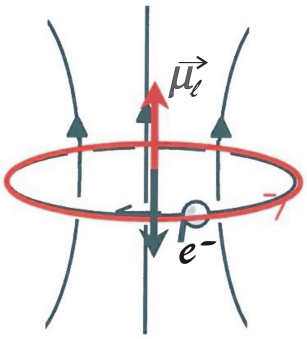

Figure 2.1: Diagrammatic representation of the orbital moment $\vec{\mu_l}$ [24].

An electron also possesses an intrinsic spin angular momentum $\vec{s}$ with an associated magnetic moment $\vec{\mu_s}$. Its origin is from relativistic quantum mechanics. The spin magnetic moment has a proportionality constant that is twice that of orbital momentum. Similar to equation 2.1.3, the pure spin angular momentum is expressed as

$$\vec{\mu_s} = \frac{-e}{m_e}\vec{s}. \tag{2.1.4}$$

In quantum mechanics the orbital angular momentum is quantized in a particular direction z giving

$$L_z = m_l \hbar, \tag{2.1.5}$$

where $\hbar$ is related to the Planck's constant h by $\hbar = h/2\pi$ and the magnetic quantum number $m_l = 0, \pm 1, \pm 2, \pm 3, ...$ Hence in the direction z, the magnetic moment can be expressed as

$$\mu_z = \frac{-e\hbar}{2m_e} m_l = -\mu_B m_l, \tag{2.1.6}$$

where $\mu_B = e\hbar/2m_e$ is the Bohr magneton which also defines the natural unit for magnetic moments.

In the presence of the magnetic field in the z-direction μ_z for spin is also quantized giving

$$\mu_z = -2\mu_B m_s, \tag{2.1.7}$$

where the magnetic quantum number due to the spin $m_s = \pm\ 1/2$. In a multi-electron system we assume that orbital momenta couple together to give the total orbital momentum

$$\vec{L} = \sum \vec{l_i}.$$

Similarly for spins we get

$$\vec{S} = \sum \vec{s_i}.$$

Finally $\vec{L}$ and $\vec{S}$ couple to give the total angular momentum

$$\vec{J} = \vec{L} + \vec{S}. \tag{2.1.8}$$

The total magnetic moment of an atom can therefore be shown to be

$$\vec{\mu}_J = -g\mu_B \vec{J}, \tag{2.1.9}$$

where the parameter g is called the Landé g-factor which is defined as

$$g = 1 + \frac{J(J+1) + S(S+1) - L(L+1)}{2J(J+1)}. \tag{2.1.10}$$

For pure orbital motion $g = 1$ and for pure spin $g = 2$ [25]. The total magnetic moment of an atom can therefore be calculated from the total angular momentum arising from both the spin and orbital angular momenta of the electrons. This is achieved by using Hund's rules and Russell-Saunders coupling [25].

2.2 Magnetization

The magnetization $\vec{M}$ is the total magnetic moments of a sample per unit volume determined usually under the influence of a magnetic field [24]. This is expressed as

$$\vec{M} = \frac{1}{V}\sum_{i=1}^{n}\vec{\mu_i}, \tag{2.2.1}$$

where V is the volume of the sample of mass m. The volume of a sample can vary with temperature. This implies that thermal expansion and magnestostriction effects can occur in a sample. Hence, defining the total magnetic moments per unit mass σ is more appropriate. This can therefore be expressed as

$$\vec{\sigma} = \frac{1}{m}\sum_{i=1}^{n}\vec{\mu_i}. \tag{2.2.2}$$

The response of magnetization of a sample under the influence of a magnetic field is called its susceptibility χ which is defined as

$$\chi = \frac{\mu_0 M}{B_0}, \tag{2.2.3}$$

where μ_0 is the permeability of free space and B_0 is the magnetic induction related to the applied magnetic field H_0 by $B_0 = \mu_0\ H_0$.

2.3 Classification of magnetic order in solids

The classification of magnetic order in solids arises from the interaction of microscopic magnetic moments in solids. This depends on the internal arrangement and orientation of the magnetic moments [26]. The common classifications such as diamagnetism, paramagnetism, ferromagnetism, antiferromagnetism, ferrimagnetism

and superparamagnetism are discussed in this section. In a classic review Hurd [26] has discussed the details of other classifications such as metamagnetism, incipient ferromagnetism, speromagnetism, asperomagnetism, helimagnetism, ideal spin glass, mictomagnetism and sperimagnetism which have been observed to occur.

2.3.1 Diamagnetism

Diamagnetism is a very weak magnetic effect and a fundamental property found in all materials. It occurs due to induced moments produced by induced eddy currents due to applied magnetic fields. The orbital motion of an electron is modified slightly to create an induced moment opposite to an applied field which gives rise to a negative susceptibility. This affects all orbital electrons [7, 27]. The atomic diamagnetic susceptibility which results is sometimes referred to as Larmor diamagnetic susceptibility [25] is given by

$$\chi = -\mu_0 n \frac{e^2}{6m_e} \sum_i^Z < r_i^2 >, \tag{2.3.1}$$

where n is the number of atoms per unit volume, Z is the atomic number and r_i are the orbital radii. In Figure 2.2 we show the magnetization M and susceptibility χ dependence on magnetic field H and temperature T respectively.

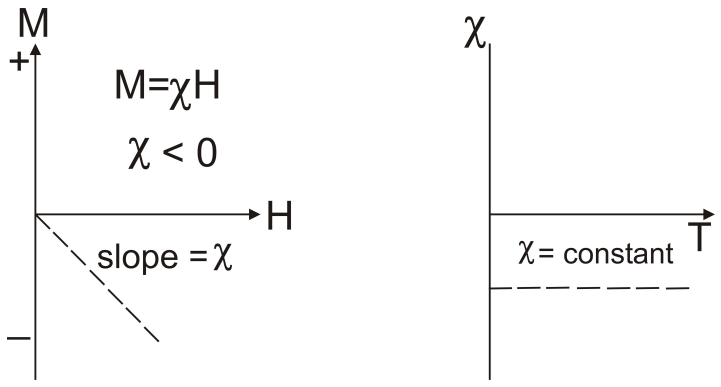

Figure 2.2: Magnetization M dependence on magnetic field H and susceptibility χ dependence on temperature T of a diamagnetic material [28].

2.3.2 Paramagnetism

Paramagnetism occurs in atoms with permanent and induced moments. Paramagnetic materials have atoms with net magnetic moments due to unpaired electrons in partially filled orbits. Each atom acts as an individual magnet in a magnetic field. Ideal paramagnetism is associated with non-interacting or a weakly interacting magnetic moments. Figure 2.3 shows the random orientation of the magnetic moments in a paramagnetic material. The application of the magnetic field causes the alignment of the atomic magnetic moments in the direction of the applied field which produce a net positive magnetization *M*. In the presence of an applied field B_0 the magnetic energy E_{m_J} of an atom is given by

$$E_{m_J} = -\vec{\mu_J}.\vec{B_0} = -g\mu_B m_J B_0, \tag{2.3.2}$$

where $\vec{\mu_J}$ is the magnetic moment of the atom. The azimuthal quantum number m_J = -*J*, -*J*+1, ... *J*-1, *J*. The thermal average of the magnetic moments is expressed as

$$< \mu_J >= \sum g m_J \mu_B P(E_{m_J}), \tag{2.3.3}$$

where $P(E_{m_J})$ is the probability for the occupation of a given energy level E_J. This is expressed in terms of Maxwell-Boltzmann distribution

$$P(E_{m_J}) = \frac{e^{-E_{mJ}/k_B T}}{\sum_{m_J} e^{-E_{m_J}/k_B T}}, \tag{2.3.4}$$

where k_B is the Boltzmann constant. Hence the average magnetic moment is given as

$$< \mu_B >= g\mu_B J F(J, x), \tag{2.3.5}$$

where *F(J,x)* is known as the Brillouin function expressed as

$$F(J, x) = (1 + \frac{1}{2J}) \coth[(1 + \frac{1}{2J})x] - \frac{1}{2J} \coth(\frac{x}{2J}). \tag{2.3.6}$$

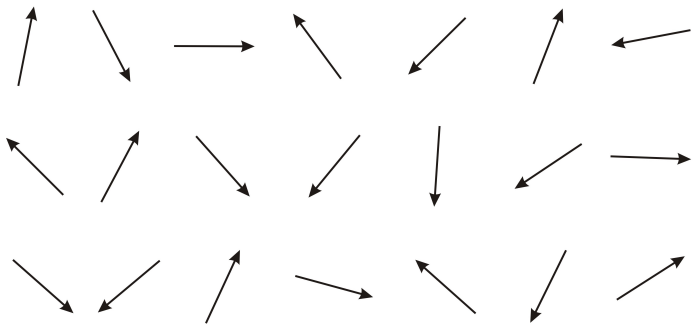

Figure 2.3: Magnetic moments of a paramagnetic material in a random orientation.

The parameter $x = g\mu_B JB_0/k_B T$ expresses the ratio of the Zeeman energy to the thermal energy. At high temperatures and low fields, x is so small that the Brillouin function can be approximated by

$$F(J, x) \simeq \frac{x(J+1)}{3J}. \tag{2.3.7}$$

The magnetization M for n non-interacting moments per unit volume assumes the expression

$$M = \frac{ng^2\mu_B^2 J(J+1)B_0}{3k_B T}. \tag{2.3.8}$$

The corresponding Curie law for susceptibility is expressed as

$$\chi = \frac{n\mu_0 g^2\mu_B^2 J(J+1)}{3k_B T} = \frac{C}{T}, \tag{2.3.9}$$

where C is the Curie constant defined as

$$C = \frac{n\mu_0 g^2\mu_B^2 J(J+1)}{3k_B}. \tag{2.3.10}$$

In Figure 2.4 we illustrate the magnetization and susceptibility dependences on the applied field and temperature respectively for non-interacting magnetic moments. Typical examples of materials that follow Curie law are rare earth compounds and salts which are associated with localised moments of $4f$ electrons. When interactions between magnetic moments exist, the Curie-Weiss law is observed which has the form

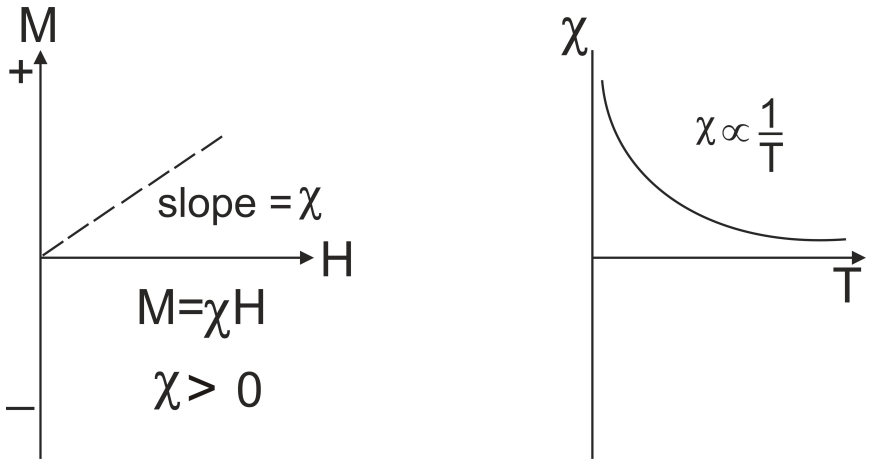

Figure 2.4: Magnetization M dependence on magnetic field H and magnetic susceptibility χ dependence on temperature T of a paramagnetic material [28].

$$\chi = \frac{C}{T - \theta_p}, \tag{2.3.11}$$

where θ_p is known as the paramagnetic Curie temperature.

2.3.3 Ferromagnetism

This is characterized by the spontaneous parallel alignment of atomic magnetic moments with long range order and large net magnetization even without the application of a magnetic field. The atomic moments of the materials in this class exhibit strong positive exchange interactions between them. Figure 2.5 shows the parallel arrangement of magnetic moments at $T = 0$ K . The alignment of the magnetic moments decrease continuously with increase in temperature and is completely destroyed at a particular temperature known as the Curie point T_C due to thermal agitation. Below T_C the samples have a net spontaneous magnetization with a perfect order achieved at 0 K. Above T_C the material looses its ferromagnetism and becomes paramagnetic. The susceptibility obeys the Curie-Weiss law. In the Weiss mean field theory the origin of ferromagnetic orders is assumed to be due to a strong internal magnetic field B_{in} that is responsible for ordering the magnetic moments. The size of the internal field is assumed to be proportional to the magnetization M_S that results. Hence

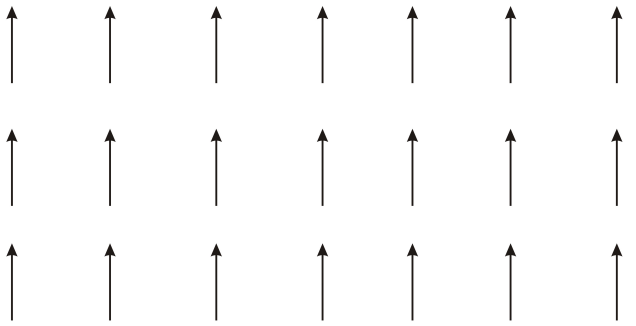

Figure 2.5: Magnetic moments of a ferromagnetic material at $T = 0$ K.

$$B_{in} = \lambda M_S, \tag{2.3.12}$$

where λ is referred to as the molecular field coefficient. In general, the effective magnetic field in an externally applied magnetic field in a sample is given by

$$B_{eff} = B_0 + B_{in} = B_0 + \lambda M_S. \tag{2.3.13}$$

In a similar manner to a paramagnet, the magnetization $M_S(B_0,J)$ of a ferromagnet can be expressed in terms of the Brillouin function *F(J,x)* where

$$M_S(B_0, T) = ng\mu_B JF(J, x). \tag{2.3.14}$$

The ratio of the Zeeman energy to thermal energy x in a ferromagnetic material is now defined as

$$x = \frac{g\mu_B J(B_0 + \lambda M_S)}{k_B T}. \tag{2.3.15}$$

The spontaneous magnetic order exists even without application of an external field ($B_0 = 0$). Hence the spontaneous magnetization at $T > 0$ K for $B_0 = 0$ can be expressed as

$$M_S(0, T) = M_S(0, 0)F(J, x), \tag{2.3.16}$$

where $M_S(0,0)$ is the saturation magnetization and x is expressed as

$$x = \frac{g\mu_B J\lambda M_S(0,T)}{k_B T}. \tag{2.3.17}$$

From equation 2.3.16 the spontaneous magnetization of a ferromagnetic material can be written in terms of the reduced magnetizations

$$\frac{M_S(0,T)}{M_S(0,0)} = F(J,x) \tag{2.3.18}$$

and

$$\frac{M_S(0,T)}{M_S(0,0)} = (\frac{k_B T}{ng^2\mu_B^2\lambda J^2})x. \tag{2.3.19}$$

The variation of the reduced magnetization as a function of x is shown in Figure 2.6. The curve C_1 represents equation 2.3.18 and it is independent of temperature while curve C_2 represents equation 2.3.19 varies proportionately to the temperature. The ferromagnetic state of the sample is represented by the intersection point of curves C_1 and C_2. The Weiss theory predicts the collapse of magnetization at T_C. Figure 2.7 shows the temperature T dependence of the saturation magnetization M_S and the inverse susceptibility above the Curie point of a ferromagnetic material. The solid line represents the temperature dependence due to itinerant electrons while the broken line represents that due to localized moments. Some typical examples of ferromagnetic materials are iron, cobalt, nickel, gadolinium and most of their alloys and oxides. The $3d$ electrons responsible for ferromagnetism in Fe, Co, Ni and their alloys are not localized. Interesting Physics related to critical phenomena can also be studied in the vicinity of T_C.

2.3.4 Antiferromagnetism

Antiferromagnetic materials have equal but opposite alignment of atomic magnetic moments resulting into zero net magnetization [29] as shown Figure 2.8. The alignment occurs due to strong negative exchange interaction between magnetic moments. The antiferromagnetic structure consist of two sublattices A and B each with saturation magnetization M_A and M_B in opposite directions. Antiferromagnetic materials have a critical ordering temperature called the Néel temperature (T_N).

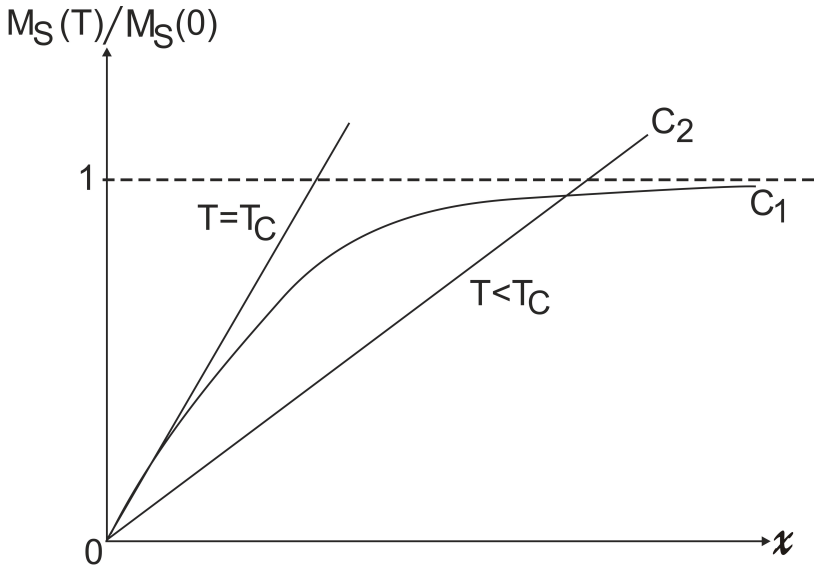

Figure 2.6: Graphical illustration of solution of equations 2.3.18 and 2.3.19.

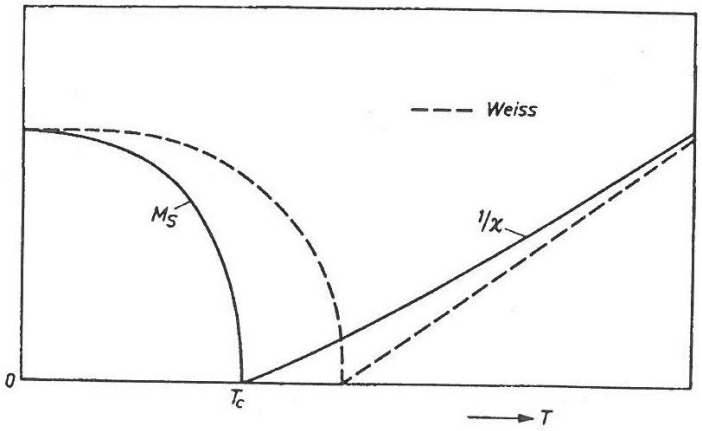

Figure 2.7: Temperature T dependence of the saturation magnetization M_S and the inverse susceptibility above the Curie point of a ferromagnetic material [7].

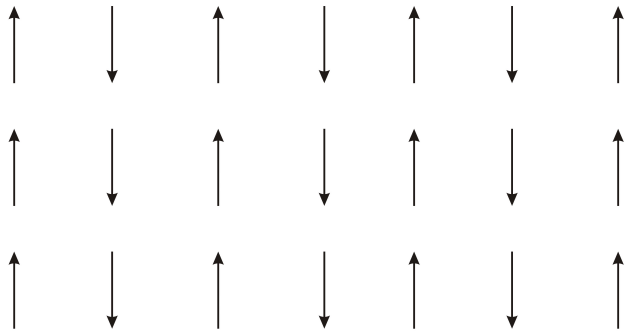

Figure 2.8: Magnetic moments of an antiferromagnetic (AF) material in an antiparallel orientation.

Above T_N, the moments are disordered and in paramagnetic state. Below T_N, the moments align such that $M_S(T) = 0$ at all temperatures $T < T_N$. At absolute zero temperature, each sublattices acquires the highest saturation magnetization. The internal magnetic fields at the sublattices are given by

$$B_{in}^{A} = \lambda_{AA} M_A + \lambda_{AB} M_B \tag{2.3.20}$$

and

$$B_{in}^{B} = \lambda_{BB} M_B + \lambda_{BA} M_A. \tag{2.3.21}$$

The effects of the intrasublattice and intersublattice interactions are represented by the molecular field coefficients $\lambda = \lambda_{BB,AA}$ and $\lambda_{AB} = \lambda_{BA}$ respectively. Using mean-field theory the magnetization at each sublattice M_A and M_B can therefore be determined in terms of the Brillouin function *F(J,x)*

$$M_i = \frac{ng\mu_B JB}{2} F(J, x_i), \tag{2.3.22}$$

where i = A, B and $x_A = \frac{g\mu_B J}{k_B T}(B_0 + B_{in}^{A})$, $x_B = \frac{g\mu_B J}{k_B T}(B_0 + B_{in}^{B})$. In the absence of an applied field the net magnetization

$$\vec{M} = \vec{M_A} + \vec{M_B} = 0 \tag{2.3.23}$$

for $T \leq T_N$. For $T > T_N$, the magnetization M depends on the applied field B_0 with an effective field B_{eff}^{A} given as

$$B_{eff}^{A} = B_0 + B_{in}^{A} = B_0 + \lambda_{AA} M_A + \lambda_{AB} M_B \tag{2.3.24}$$

and

$$B_{eff}^{B} = B_0 + B_{in}^{B} = B_0 - \lambda_{BB} M_B - \lambda_{BA} M_A. \tag{2.3.25}$$

The χ for $T > T_N$ follows the Curie-Weiss law

$$\chi = \frac{C}{T - \theta_P}, \tag{2.3.26}$$

where $C = 2C' = 2(\frac{\mu_0 (n/2) g^2 \mu_B^2 J(J+1)}{3k_B})$ and the paramagnetic Curie temperature θ_P $= C'(\lambda_{AA} + \lambda_{BB})$. The $1/\chi$ behaviour above T_N follows a linear dependence with a negative Curie temperature θ_p indicating a negative exchange with T_N = - θ_p [24] as shown in Figure 2.9.

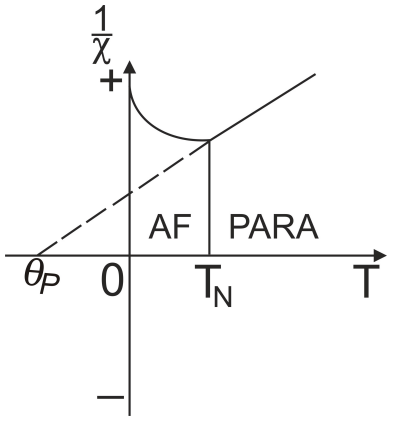

Figure 2.9: Susceptibility χ dependence on temperature T of an antiferromagnetic material with discontinuity at the Néel temperature T_N showing a negative Curie temperature T [26].

For χ at $T < T_N$ consideration has to be given to the direction of the applied field with respect to the directions of the spins. The susceptibility depends on B_0 being either perpendicular $\chi_\perp$ or parallel $\chi_\parallel$ to the orientation of the spins. For a polycrystaline sample below T_N the susceptibility is expressed as [24]

$$\chi = \frac{2}{3}\chi_\perp + \frac{1}{3}\chi_\parallel. \tag{2.3.27}$$

From Figure 2.9 we can deduce that a plot of χ against T has a maximum at T_N.

2.3.5 Ferrimagnetism

Ferrimagnetism is also known as the uncompensated antiferromagnetism exhibited by materials whose magnetic order consists of two or more unequal magnetic moments on sublattices resulting in a net magnetic moment [7] as shown in Figure 2.10. Ionic compounds of oxides such as magnetites are typical examples of ferrimagnetic materials. This is the magnetic order associated with ferrites. The exchange interaction between the A- and B-sites of these materials are mediated by oxygen anions. The spins on A-sites are antiparallel to those on B-sites. A curie temperature T_C exists such that at temperatures above T_C paramagnetism occurs and below T_C spontaneous magnetization takes place [24]. The net saturation magnetization can be modelled by an equation of the form

$$M = M_A - (1 - \lambda)M_B, \tag{2.3.28}$$

where $M_A \neq M_B$. The two possible states of λ that define ferromagnetism are λ = 1 or 2. When $\lambda = \frac{1}{2}$ antiferromagnetism occurs. Ferrimagnetism occurs when $\lambda \neq 0$, $\frac{1}{2}$ or 1. Below T_C, the net magnetization of ferrimagnets has a non-zero value except when the sublattices cancels out at a temperature known as the compensating temperature T_{comp}. Figure 2.11 shows the sublattice magnetization of a ferrimagnet. Above T_C the magnetization at the sublattices is given as

$$M_A = (\frac{C_A}{T})(\lambda_{AA}M_A + \lambda_{AB}M_B + B_0) \tag{2.3.29}$$

and

$$M_B = (\frac{C_B}{T})(\lambda_{AB}M_A + \lambda_{BB}M_B + B_0), \tag{2.3.30}$$

where λ_{AA}, λ_{AB} and λ_{BB} are the Weiss coefficients for the inter- or intra-sublattice interactions.

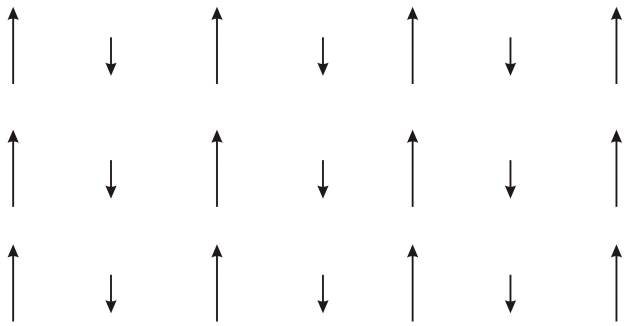

Figure 2.10: Orientation of the magnetic moments in a ferrimagnetic material.

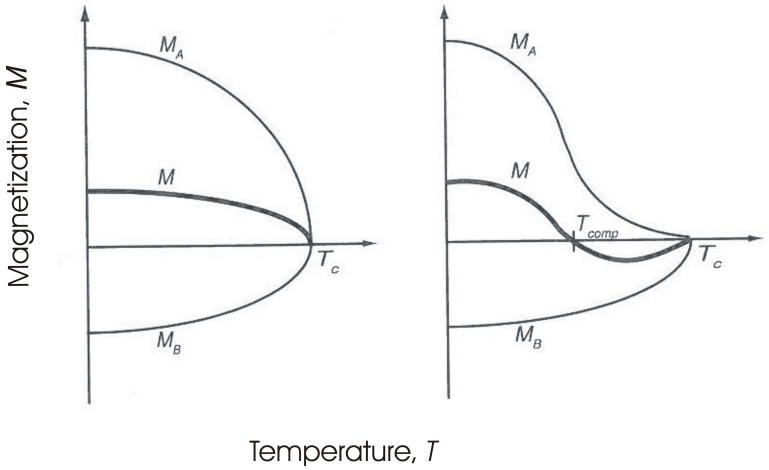

Figure 2.11: Sublattice magnetization of a ferrimagnet [24].

2.3.6 Superparamagnetism

Superparamagnetism is the magnetic order that is characterized by small domain particles usually associated with ferromagnetic or ferrimagnetic nanoparticles. The magnetic moments of the particles can be about 10^5 larger than that of an individual atom [25]. Some amount of energy is usually required to overcome the crystal field anisotropy of the material as a result of thermal fluctuations that exist within the moments at a microscopic level. This energy is given as

$$\Delta E = KV \sin^2 \theta, \tag{2.3.31}$$

where V represents the volume of the nanoparticle, K is the uniaxial anisotropy energy density and θ is the angle between the direction of the moments and the easy axis. The magnetization of these materials can randomly flip direction under the influence of temperature. Néel relaxation time τ_N defines the typical time between two of such flips. It is mathematically expressed by the Néel-Arrhenius equation given as

$$\tau_N = \tau_0 \exp(\frac{KV}{k_B T}), \tag{2.3.32}$$

where τ_0 is a length of time characteristics of the material, k_B is the Boltzmann constant and T is the temperature. Below a certain temperature called the blocking temperature T_B, time-scale measurement τ_M of the nanoparticle magnetization is much longer than the Néel relaxation time τ_N. This causes the moments to appear frozen. Hence the blocking temperature of a superparamagnetic material occurs at a temperature where $\tau_M = \tau_N$. The Langevin classical function *L(x)* that best describes the magnetic behaviour of superparamagnetism is expressed as

$$L(x) = \coth x - \frac{1}{x}, \tag{2.3.33}$$

where

$$x = \frac{\mu B_0}{k_B T} \tag{2.3.34}$$

and μ is the magnetic moment of single domain particles. The *L(x)* function is the classical analog of the Brillouin function which describes the magnetization of small particles. Figure 2.12 shows the reduced magnetization of a superparamagnet that can be described by the classical Langevin function [25].

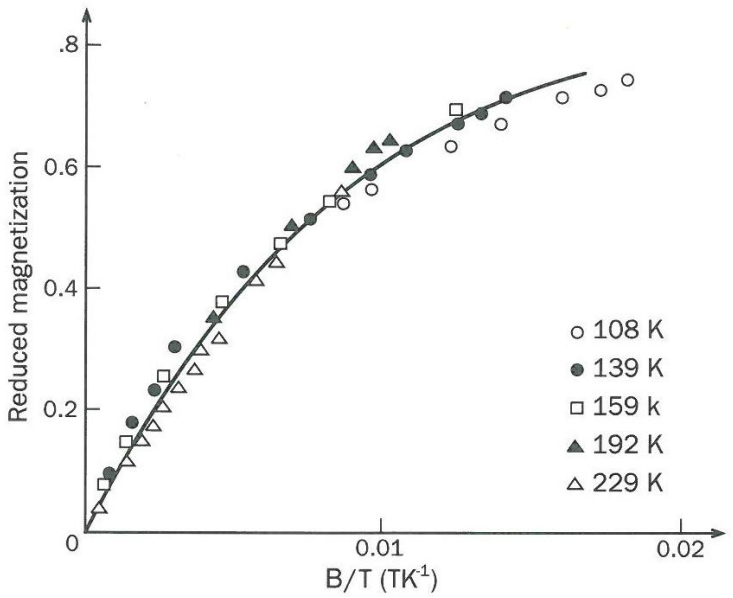

Figure 2.12: Experimental variation of the reduced magnetization of superparamagnetic ferrite materials obtained at different temperatures, versus B/T, where the continuous line is the Langevin function [25].

2.4 Energy in magnetic materials

The magnetic behaviour of ferromagnetic materials such as ferrites, iron, cobalt, nickel and their alloys is largely influenced by their magnetic domain structure. A domain is a uniformly magnetised region within a magnetic material. It contains about 10^{12} to 10^{15} atoms [7]. A material can consist of several of these domains with magnetization of individual domain pointing in a particular direction while the collective domains may point in different directions. Domains are separated by domain walls (Bloch walls) with thickness δ. The thickness of a domain wall consisting of atoms with spins S can be expressed as

$$\delta = \pi S \sqrt{\frac{J}{Ka}}, \tag{2.4.1}$$

where J is an exchange parameter, K is the anisotropy constant and a is the distance between atoms. The domain structure is a natural consequence of various energies such as exchange energy E_{ex}, magnetostatic energy E_D, magnetoelastic anisotropy energy E_λ, magnetocrystalline anisotropy energy E_K and Zeeman energy E_H [30]. These energies contribute towards the total energy of a magnetic material expressed as

$$E = E_{ex} + E_D + E_\lambda + E_K + E_H. \tag{2.4.2}$$

The domain structure that forms is that which minimizes the total energy of the system.

2.4.1 Exchange energy

Exchange energy E_{ex} is the energy due to the exchange interaction between the atomic spins responsible for magnetic order in ferromagnetic, ferrimagnetic and antiferromagnetic materials. For a pair of neighbouring atoms having spins S_i and S_j, Heisenberg showed that the exchange energy between the atoms is given by

$$E_{ex} = -2J_{ij}\vec{S_i}.\vec{S_j}, \tag{2.4.3}$$

where the exchange parameter J_{ij} gives a measure of the extent to which the electronic charge distribution of electrons overlaps. This parameter is also known as the exchange integral. $J_{ij} > 0$ for ferromagnetic interaction and $J_{ij} < 0$ for antiferromagnetic interaction. For one-dimensional chain of $N + 1$ neighbour atoms, the increase in the exchange energy due to the formation of domain walls is given by

$$E_{ex} = JS^2 \sum_{i}^{N} \phi_i^2, \tag{2.4.4}$$

where ϕ is the angle between the spins.

The probability of direct overlap of the electron charge distribution between moments in ferrites tends to be very small. Hence the exchange mechanism between magnetic moments occurs through indirect exchange interaction with intermediary oxygen ions. The indirect exchange interaction is known as superexchange interaction. The indirect exchange interaction is able to couple moments that are at relatively large distances apart. This is the dominant exchange interaction when there is little or no direct overlap between neighboring moments. When the indirect exchange is mediated by conduction electrons, the interaction between magnetic moments far apart is known as the Ruderman, Kittel, Kasuya and Yoshida (RKKY) interaction. Super-exchange interaction therefore defines the interaction between relatively long distance moments coupled through a non-magnetic ion. This is a typical type of exchange interactions in ferrites where the metal cations interact through an intermediary of oxygen anion, while the RKKY interaction is common to alloys.

2.4.2 Magnetostatic energy

The magnetostatic energy E_D defines the self-energy arising from the interaction of a particle with the magnetic field created by the particle or an external field. The energy is a demagnetizing energy which is required to align magnetic poles in certain geometry [7, 24]. It is expressed as

$$E_D = -\frac{1}{2}\mu_0 \vec{H}_d . \vec{M}, \tag{2.4.5}$$

where H_d is the demagnetizing field. This energy is reduced by minimizing the length of the loops of magnetic field lines outside the domains. Néel and Kittel calculated the E_D of flat strips of thickness d magnetized to intensity M as

$$E_D = 0.85dM^2. \tag{2.4.6}$$

Consequently other shapes may be considered giving a general formula for self-energy as

$$E_D = CdM_S^2, \tag{2.4.7}$$

where C is a constant [7].

2.4.3 Magnetoelastic anisotropy energy

Magnetoelastic anisotropy energy E_λ is the energy due to changes in the dimensions of crystals when magnetized. The field produces elastic strains in the lattice and the magnetization favours the direction that minimizes this strain energy. When the direction of magnetization of the domains in a crystal are all parallel this energy tends to be minimized. The magnetoelastic energy in a cubic crystal can be expressed as

$$E_\lambda = B_1(\alpha_1^2 \in_{xx} + \alpha_2^2 \in_{yy} + \alpha_3^2 \in_{zz}) + B_2(\alpha_1\alpha_2 \in_{xy} + \alpha_2\alpha_3 \in_{yz} + \alpha_3\alpha_1 \in_{zx}), \tag{2.4.8}$$

where the B_i are known as magnetoelastic coupling constants, α is the direction cosines and $\in$ is the strain along the x, y and z directions [25].

2.4.4 Magnetocrystalline anisotropy energy

Magnetocrystalline anisotropy energy E_K is the energy difference between the magnetization of a material along an easy preferred axis and a hard axis. It defines the energy required to rotate the moment of a material from its easy axis. Magnetocrystaline anisotropy is the main source of intrinsic anisotropy. The energy is generated mainly from the interaction of orbital angular momenta with the electric

field at the site of the magnetic ions [25]. The general expression of the energy for cubic crystals is given as

$$E_K = K_0 + K_1(\alpha_1^2\alpha_2^2 + \alpha_2^2\alpha_3^2 + \alpha_3^2\alpha_1^2) + K_2(\alpha_1\alpha_2\alpha_3)^2 + ..., \tag{2.4.9}$$

where α_i are the direction cosines. K_0, K_1 and K_2 are the anisotropy constants which can be derived from the areas of the magnetization curves obtained for each direction. The constants are temperature dependent and tends to zero at T_C. At room temperature measurement for bulk bcc Fe, the magnetocrystalline anisotropy is minimum when the magnetization is along the easy direction (100) and hard directions along (111) with the intermediate directions along (110). Bulk fcc Ni under the same conditions makes easy directions along (111) and hard directions along (100) with the intermediate directions along (110) [31].

2.4.5 Zeeman energy

The Zeeman energy E_H defines the energy added to or subtracted from the magnetostatic energy as result of interactions between a magnetic material and an externally applied magnetic field. When the magnetic moments in a domain are aligned parallel to applied magnetic field the Zeeman energy is reduced. The Zeeman energy is increased when the moment and magnetic field are in opposite alignment. The Zeeman energy of the magnetic moment m in an external field B is expressed as

$$E_B = -\vec{m}.\vec{B}. \tag{2.4.10}$$

In a uniform field, there will be no net force on a magnetic moment. However, a net force will be experienced in a nonuniform magnetic field [24] which is expressed as

$$F_B = -\bigtriangledown E_B = \bigtriangledown(\vec{m}.\vec{B}). \tag{2.4.11}$$

This force minimizes the E_B for ferromagnets or paramagnets by pulling the magnetic moments in the direction of the greatest field [24].

2.5 Magnetic hysteresis loop

The magnetization process that gives rise to the shape of a magnetic hysteresis loop comes from the displacement of domain walls. The magnetization is uniform inside a domain and non-uniform across a domain wall [24]. A hysteresis loop is a graphical representation of the magnetization of a sample against an applied field H. It consist of curves in four quadrants depending on the direction of the magnetic field to as magnetic hysteresis loop or magnetization curve. This is referred to as M-H curve or sometime called B-H curve. The loop traces response of the domains due to the effect of an applied magnetic field. Important magnetic properties of a sample can be deduced from the loop. The presence of impurities, defects or grain boundaries in a sample will affect the shape of the hysteresis loop [25]. A typical hysteresis loop is shown for one of our samples in Figure 2.13.

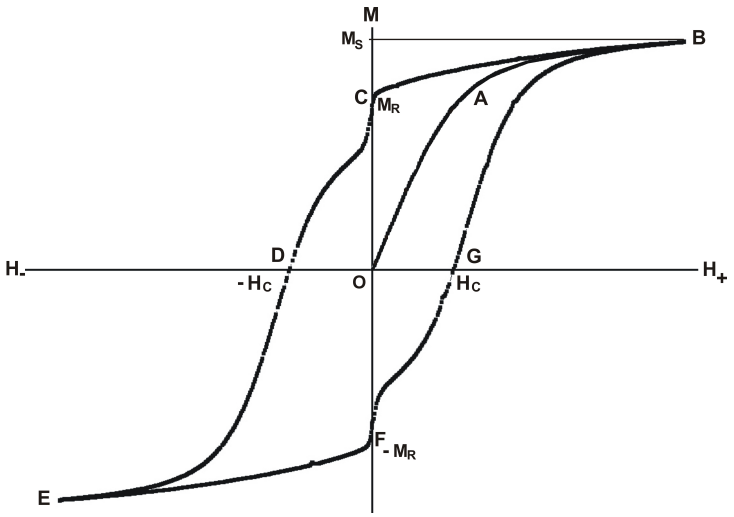

Figure 2.13: Magnetic hysteresis loop of $CoFe_2O_4$ measured at 4 K in the current work.

The curve OB shows the gradual increase of the initial magnetization of the sample under the influence of applied magnetic field. At B we assume that the sample is subjected to a saturating field. Samples with high saturation magnetization find applications in high frequency devices. The magnetization $M(H)$ can be described by an empirical formula of the form

$$M(H) = M_S(0)(1 - \frac{a}{H} - \frac{b}{H^2} - ....) + \chi H, \tag{2.5.1}$$

where a and b are fit parameters and χ is the high-field susceptibility [32]. When the applied field is reduced to zero and increased in the reverse direction we get curve BCDE. Reducing the field to zero and increasing the field in the reverse direction we get EFGB which completes the hysteresis loop. When the field decreases from maximum to 0, the magnetization reduces to a finite value M_R (OC). This is known as the retentivity, remanence or remanent magnetization of the sample. This is a critical parameter for possible applications such as random access memory in computers. The modulus of the field OD or OG gives another magnetic property of the sample called coercivity or coercive field H_C. Materials with large coercivity usually possess large maximum energy product $(BH)_{max}$. Such materials are usually hard magnetic materials or permanentmagnets which have important applications in magnetic data recording and storage. Soft magnetic materials have low coercivity but tend to have high saturation magnetization and are characterized by narrow hysteresis loops.

2.5.1 Soft and hard magnetic materials

Magnetic materials are usually categorized into two types namely, soft and hard magnetic materials. The magnetism of soft magnetic materials characterized by their magnetism can easily be revealed by application of a small magnetic field. Soft magnetic materials are easy to magnetize and demagnetize [5]. Amongst other characteristics of these materials are low coercive fields and anisotropy, high susceptibility, permeability and saturation magnetization. Soft ferrites therefore have low energy loss making them ideal for several applications such as enhancing the flux generated by current carrying coils in power devices, components in microwave devices, computers, magnetic amplifiers and high frequency devices [33]. A typical example of a soft ferrite is $NiFe_2O_4$.

Hard magnetic materials possess a net magnetization and do not easily demagnetize. They have a high potential to retain their magnetization after the application

of a magnetic field unlike soft magnetic materials [5]. This unique property arises from the restriction of domain wall movements because of the existence of large anisotropy. Some characteristics associated with these materials are high coercivity, high energy product (BH), low susceptibility, permeability and high eddy current loss. Hard magnetic materials are commonly used in permanent magnets applications. A typical example of a hard ferrites is $CoFe_2O_4$. $CoFe_2O_4$ and $NiFe_2O_4$ nano-ferrites are the parent materials in the current study.

Chapter 3

Experimental details

3.1 Introduction

Research efforts for scalable and efficient synthesis method of nano-materials have increased in recent times. This has happened mainly because of targeted properties of these materials for specific applications. The properties are usually influenced by the synthesis method of the nano-material and constituent atoms. The synthesis of nano-ferrite materials by solid state reaction has been reported to be less efficient in gaining control of consistent morphology of the materials. Inconsistencies in properties have been reported [3]. Wet chemical synthesis methods on the other hand such as glycol thermal, hydro-thermal and co-precipitation has been more success in controlling the grain size, crystallinity, cationic distribution and morphology for transition metal ferrites [11]. The glycol-thermal method was used in the present work to synthesize the starting nano-ferrites. This method has been reported to produce single phase materials with small crystallite sizes at a relatively low temperature of about 200 °C [34]. Nanocomposites of ferrite/alloy were obtained by the reduction reaction of the ferrites with activated charcoal (carbon fine powder) in flowing high purity argon gas atmosphere in a tube furnace. We also attempted unsuccessfully to use high energy ball milling technique to perform the reduction reaction. The single phase formation of the ferrites and the evolution of the nanocomposites were confirmed by X-ray diffraction (XRD). The energy-dispersive X-ray spectroscopy (EDX) was used to visualize the elemental compositions of some

of the samples. Further structural characterizations employed high-resolution transmission electron microscopy (HRTEM) and Zeiss ultra plus high-resolution scanning electron microscopy (HRSEM). The magnetic characterizations of the samples were investigated by ^{57}Fe Mössbauer spectroscopy and by magnetization measurements. The relevant details for the experimental procedures and the equipment used in the present work are discussed in this chapter.

3.1.1 Glycol-thermal synthesis method

The glycol-thermal synthesis method is a wet chemical method that involves the use of stoichiometric precursors of metal chlorides or nitrates that are dissolved in de-ionized water to form a mixed solution of starting compounds. Ammonia, potassium hydroxide or sodium hydroxide can be used to precipitate the metal chlorides or nitrates from solutions. This is performed while continuously stirring the solution until a deserved pH of about 9 is reached. The precipitate is then washed several times in de-ionized water to get rid of the chlorides or nitrates. This is followed by the reaction of the precipitate in ethylene glycol in a high pressure reactor. A PARR 4843 stirred pressure reactor shown in Figure 3.1 was used for the synthesis of the materials. The reaction chamber houses a stirrer that enables the continuous stirring of the reactants during synthesis. The readings for the reaction conditions such as stirring speed, pressure and temperature are digitally displayed on the control unit.

The $CoFe_2O_4$ and $NiFe_2O_4$ nano-ferrites used in the present work were synthesized by the glycol-thermal method. $CoFe_2O_4$ nano ferrite was synthesised from 11.6390 g of $FeCl_3.6H_2O$ (99%) and 5.1740 g $CoCl_2.6H_2O$ (98%). All chemicals were used as purchased from Sigma-Aldrich Chemicals without further purification. The stoichiometry was calculated to yield a target mass of 5 g of $CoFe_2O_4$. The chlorides were initially dissolved in 400 ml of de-ionized water in a beaker placed on a magnetic stirrer. A pH value of 2.51 was initially recorded. After 20 minutes of continuous stirring for the homogeneous mixture, ammonium solution was gradually added to initiate precipitation of the metal chlorides until a pH of 9 which was maintained for 30 minutes while stirring. The precipitated solution was washed several times over a Whatman (GF/F 110 mm) glass microfibre filter in a Büchner

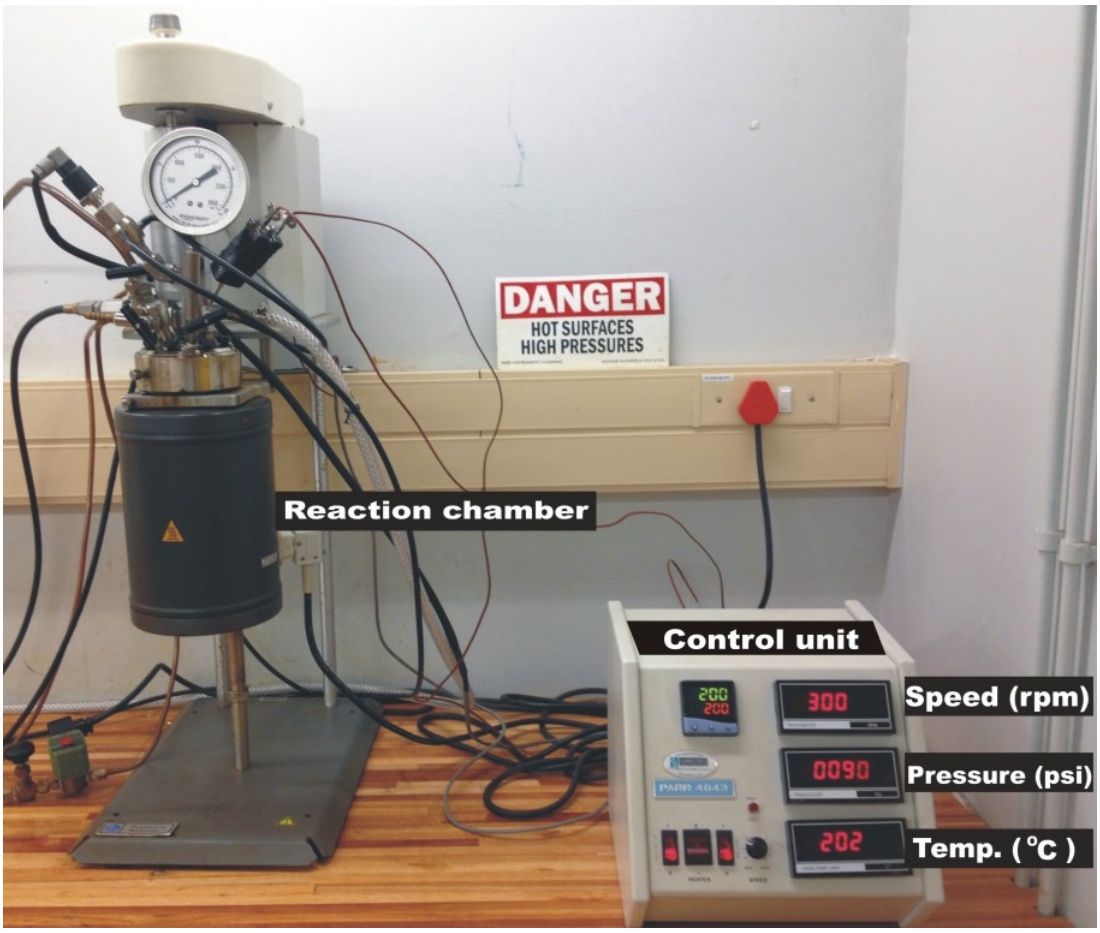

Figure 3.1: PARR 4843 stirred pressure reactor, Condensed Matter Physics Lab (WC), UKZN.

funnel with de-ionized water in order to get rid of chlorides. The absence of chlorides was confirmed by the addition of standard solution of $AgNO_3$ to the filtrate until no precipitate of $AgCl_2$ was detectable. The washed precipitate was recovered from the filter, mixed with 250 ml of ethylene glycol and transferred into the reaction chamber. The reactor was operated at a soak temperature of 200 °C for 6 hours at a stirring speed and pressure of 300 rpm and 80 psi respectively. Figure 3.2 shows the synthesis schedule in the pressure reactor. The cooled final product was finally filtered over a fresh Whatman filter and rinsed with 200 ml of ethanol. The sample was allowed to dry on the filter paper under a 200 W infrared light for 24 hours. The dried blackish sample was homogenized into fine powder by agate mortar and pestle. A mass of 4.6790 g of the ferrite was produced and stored at room temperature. The difference in the target mass and actual mass recorded was as a result of some samples being lost during synthesis process. $NiFe_2O_4$ nano-ferrite was synthesized following the same procedure used for $CoFe_2O_4$, except that the initial washing of the precipitate with de-ionized water was done using a centrifuge and the pressure

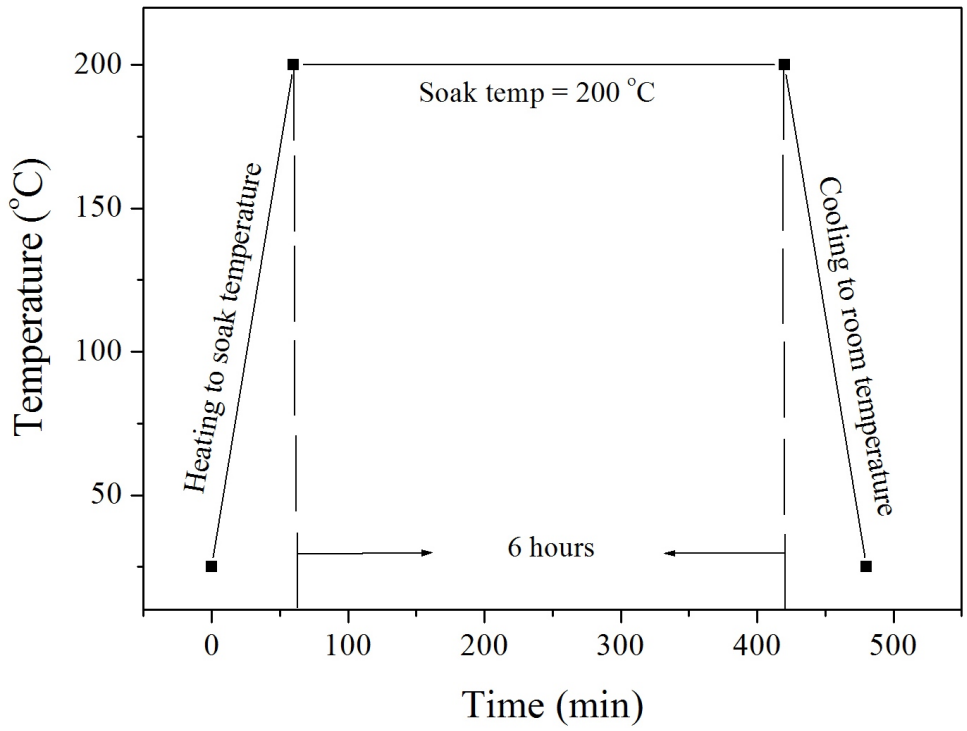

Figure 3.2: Synthesis schedule for the PARR 4843 stirred pressure reactor.

reactor maintained a pressure of 130 psi. The centrifuge was operated at a speed of 2.5 rpm for 3 minutes per time to test for the presence of chloride.

3.1.2 Reduction reaction technique

The nanocomposites and alloys were produced by the reduction of the ferrites with activated charcoal. This follows the reaction between ferrites and carbon based on chemical equations

$$\mathrm{CoFe_2O_4} + n_C\mathrm{C} \longrightarrow \mathrm{CoFe_2} + n_C\mathrm{CO_2}$$

and

$$\mathrm{NiFe_2O_4} + n_C\mathrm{C} \longrightarrow \mathrm{NiFe_2} + n_C\mathrm{CO_2}.$$

The amount of activated charcoal used for reductions was based on different molar ratios of activated charcoal n_C to ferrite according to the formula

$$n_C = \frac{m_C}{M_C}.\frac{M_f}{m_f}, \tag{3.1.1}$$

where m_f is the mass of ferrite, M_F is the molar mass of ferrite, m_c is the mass of activated charcoal used and M_C is the molar mass of activated carbon. The mass of ferrite used for each reduction was fixed to 0.5 g. All the reductions were performed in a Sentro Tech tube furnace (Figure 3.3) at 900 °C for 3 hours in high purity (99.999 %) flowing argon gas atmosphere. The ferrites were thoroughly mixed with specific amounts of activated carbon (as in Table 3.1) and loaded in a labelled crucible boats which were inserted in the furnace. Figure 3.4 shows the schedule for the reduction reaction process for the furnace.

3.2 X-ray diffraction

X-ray diffraction (XRD) is a structural characterization technique for the identification of the crystalline structure and identification of different phases in a sample. Information about the spacing between rows of atoms known as the d spacing can be derived. XRD data also provides the possibility of measuring the size, shape and internal stress of small crystalline regions and the orientation of a single crystal [35].

Figure 3.3: Sentro Tech high temperature tube furnace, Condensed Matter Physics Lab (WC), UKZN.

Table 3.1: Molar mass ratio n_C and mass of carbon m_c used with 0.5 g of $CoFe_2O_4$ or $NiFe_2O_4$.

n_C	m_c (g)	
	$CoFe_2O_4$	$NiFe_2O_4$
0.5	0.0123	-
1	0.0256	0.0256
2	0.0512	0.0512
4	0.1024	0.1025
5	0.1280	0.1281
6	0.1536	0.1537
8	0.2048	0.2050
10	0.2560	0.2562

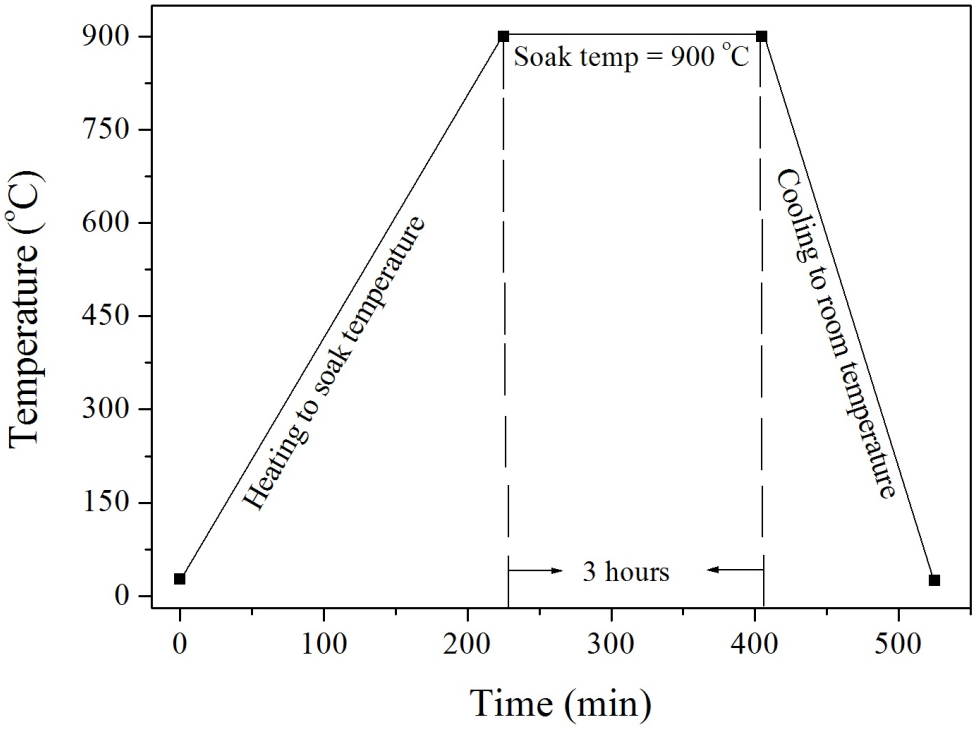

Figure 3.4: Schedule for the Sentro Tech high temperature tube furnace for the reduction reaction.

The technique operates on the principle of diffraction where the atomic planes of a crystal cause incident beams of X-rays to interfere with each another as they leave the crystal. Diffraction occurs only when Bragg's law is satisfied. Mathematically Bragg's law is expressed as

$$n\lambda = 2d\sin\theta, \tag{3.2.1}$$

where n is an integer, λ is the wavelength of the incident beam and θ is the angle between the incident beam and the scattering plane. The lattice constant a of a cubic crystal has a relationship with the d spacing of a sample by the following equation

$$a = d\sqrt{h^2 + k^2 + l^2}, \tag{3.2.2}$$

where h, k, and l are called the Miller indices. Therefore substituting Bragg's law into the equation 3.2.2 gives

$$a = \frac{\lambda}{2\sin\theta}\sqrt{h^2 + k^2 + l^2}. \tag{3.2.3}$$

The X-ray densities ρ_{XRD} of the ferrites can be calculated from the values of the lattice parameter a derived from equation 3.2.3 using the formula

$$\rho_{XRD} = \frac{8M}{N_A a^3}, \tag{3.2.4}$$

where M is the molecular weight, N_A is the Avogadro's number [34]. The crystallite sizes D can be computed by the Scherrer's formula

$$D = \frac{K\lambda}{W_{(hkl)}\cos\theta}, \tag{3.2.5}$$

where K is the shape factor usually taken as 0.9 for particles of unknown shape (0.89 for spherical particles and 0.94 for cubic particles), $\lambda = 1.7903$ Å is the wavelength of the monochromatic X-ray beam and W_{hkl} is the full-width at half-maximum of the line broadening diffraction peak derived from the most prominent (311) peak [34]. Figure 3.5 shows a schematic diagram of the mechanical assembly of an Empyrean PANalytical diffractometer type PW 1710 with CoKα radiation source operated

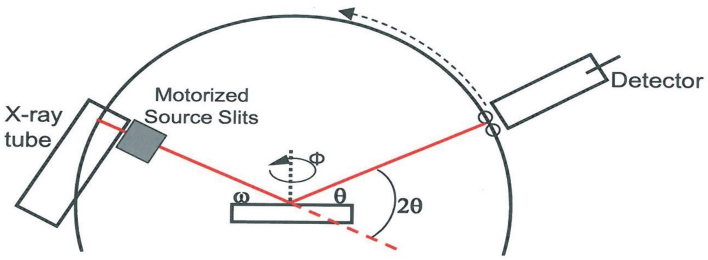

Figure 3.5: Mechanical assembly of a typical 2θ coupled X-ray diffractometer [36].

over a 2θ range from 10° to 80°. ω is the angle of incidence of the X-ray. Figure 3.6 shows the XRD machine used for the current set of measurements.

3.3 High resolution transmission and scanning electron microscopy

High resolution transmission electron microscopy (HRTEM) is an imaging technique that is used to perform size, shape and crystallographic structure analysis of samples in the micro, nano and sub-nanometer range. The basic principle of operation is such that images formed are generated from the interaction of electron beams transmitted through a thin sample. The images are usually magnified and focused by an objective lens and appears on an imaging screen detected by a sensor such as charge-coupled device camera. Sample preparation for HRTEM is crucial as the images can be affected by the thickness of the sample. A Joel-JEM-2100 high-resolution transmission electron microscope shown in Figure 3.7 was used to study our samples. A small sample size of about 0.0002 g was dispersed in ethanol and vibrated in a 80Hz\40 Watt transistorized sonic cleaner for 3 minutes. A copper thin film sample holder with diameter of about 0.0005 mm is dipped into the dispersed sample and loaded in the equipment in order to produce scanned images of the sample.

Figure 3.6: PW 1710 Empyrean PANalytical X-ray diffractometer, Geology (WC), UKZN.

Figure 3.7: Joel-JEM-2100 high-resolution transmission electron microscope, EM Unit (WC), UKZN.

High resolution scanning electron microscopy (HRSEM) is a technique that explores the surface morphology of a sample. The principle of its operation is similar to that of the HRTEM except that the electron beam is directed mainly at the surface of a sample. Signals are generated when the beam of electrons strikes the surface of a sample. This provides some energy level information about the elemental composition of the sample. The technique is also referred to as energy dispersive X-ray. A Zeiss ultra plus high resolution scanning electron microscope was used to perform measurements. Figure 3.8 shows the HRSEM equipment and the sample holder used in this work. In order to prepare sample for scanning, one side of a carbon tape with two-sided sticky surfaces is secured on the sample holder. The other surface is then lightly matched over the sample and wiped lightly with a filter paper to avoid particles dropping off or too much sample on the surface. To avoid charging of the sample by the electron beam, the sample is usually coated with gold using a Polaron SC 500 sputter coater shown in Figure 3.9.

3.4 Magnetization measurements

The magnetization measurements were obtained using a LakeShore model 735 vibrating sample magnetometer (VSM) and a Cryogenic Ltd 5 Tesla (50 kOe) mini cryogenic free system (CFS). In the LakeShore VSM, the sample rod was mounted into a Janis model helium cryostat and only a maximum applied magnetic field of about 14 kOe was available for this system. The mini CFS has capabilities for VSM, AC susceptibility, resistivity and Hall effect measurements from 1.6 K to 700 K. VSM measurements only were performed in this present work and details are of the magnetization measurements are given in subsequent sections.

3.4.1 LakeShore model 735 vibrating sample magnetometer

In Figure 3.10 we show the LakeShore model 735 VSM equipment. The system consists of a 735 VSM controller and the vibrating head which is mounted above the Janis helium cryostat. The bottom neck of the cryostat is centred between the pole faces of the electromagnet. Pick-up coils are mounted on the faces of the poles

Figure 3.8: Zeiss ultra plus high resolution scanning electron microscope, EM Unit(WC), UKZN.

Figure 3.9: Polaron SC 500 sputter coater, EM Unit (WC), UKZN.

Figure 3.10: LakeShore 735 vibrating sample magnetometer (VSM), Condensed Matter Physics Lab (WC), UKZN.

of the electromagnet. Other critical components of the system include a 642 bipolar electromagnet power supply, 340 temperature controller, 450 gaussmeter, a NESLAB ThermoFlex 2500 chiller and a National Instrument IEEE-488 interface card installed in a desktop computer for data collection. The principle of operation of a VSM is based on Faraday's law of induction which defines the induced voltage produced in the pick-up coils that is proportional to the magnetization of the sample. In Faraday's law

$$\frac{d\Phi}{dt} = -E, \tag{3.4.1}$$

where $\frac{d\Phi}{dt}$ is the rate of change of magnetic flux and E is the induced voltage. The technique measures the magnetic moment by detecting the AC field produced by the oscillation of a magnetized sample. Figure 3.11 shows a sample vibrating in between two pick-up coils. The arrows indicate magnetic field around the sample. The magnetization of the sample is proportional to the amplitude of the induced signal [37]. The VSM was calibrated using a standard nickel sphere. The sample to be measured is placed in a cylindrical sample holder which is screwed to the lower end of the vibrating sample rod. The rod is gently lowered into the sample space to the final position of the sample between the pick-up coils. The data is collected using the interface card and the data acquisition software installed on the computer. Only room temperature measurements were performed on this system.

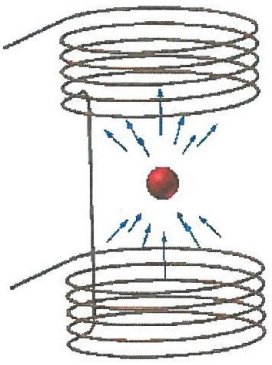

Figure 3.11: Schematic diagram of a magnetic sample in between VSM pick-up coils. The arrows indicate magnetic field lines associated with a magnetic sample [37].

3.4.2 Mini cryogen free system

The Cryogenic Ltd mini cryogen free system (CFS) comprises of a cryo-cooler system, variable temperature insert (VTI), electronics rack, measurement systems software installed on a desktop computer and superconducting magnet. It operates with the same principle as the VSM for magnetization measurements. However, it has the potential to measure magnetic fields up to 5 tesla with a temperature range of 1.6 K to 700 K. The VTI provides the option of varying the sample temperature. In addition the CFS has inserts for high temperature VSM, AC susceptibility, resistivity and Hall effect measurements. Only the VSM low temperature option was used in the present set of measurements. The calibration for magnetization measurement on this system was done using yttrium iron garnet sphere. Procedures such as evacuating the VTI, helium gas inlet, helium dump, vacuum, and recharging the dump were carried out to avoid possible contamination in the helium dump and sample space by air. The procedures are discussed in subsequent subsections. Figure 3.12 shows the schematic diagram of the VTI circuit. The operation of the system is carried out by software commands using a LabVIEW graphical programming software interface. Only procedures such as disconnection-reconnection of hoses and sample mounting are done manually. Figure 3.13 shows the set up of the mini cryogen-free VTI system used for measurements. An enlarged view of various parts are shown in Figure 3.14. The sample preparation and loading is different from that of the LakeShore VSM. A small amount of 0.005 g of sample is required for measurements. The sample is loaded into a Perspex cone and held fixed by cotton wool to avoid torque. The loaded Perspex cone is guided into an 80 mm length of straw through a slit made at a position of about 20 mm on the straw as shown in Figure 3.15. The position of the sample in the cone is fixed around the 20 mm position which is firmly held together with the straw by a piece of Kapton tape. The straw is then screwed to the probe rod using the adaptor provided on the rod and mounted into the airlock position shown in Figure 3.13. The lowering of the sample probe into the sample space is prompted by series of commands from the sample load option in the software menu shown in Figure 3.14. The commands are interactive.

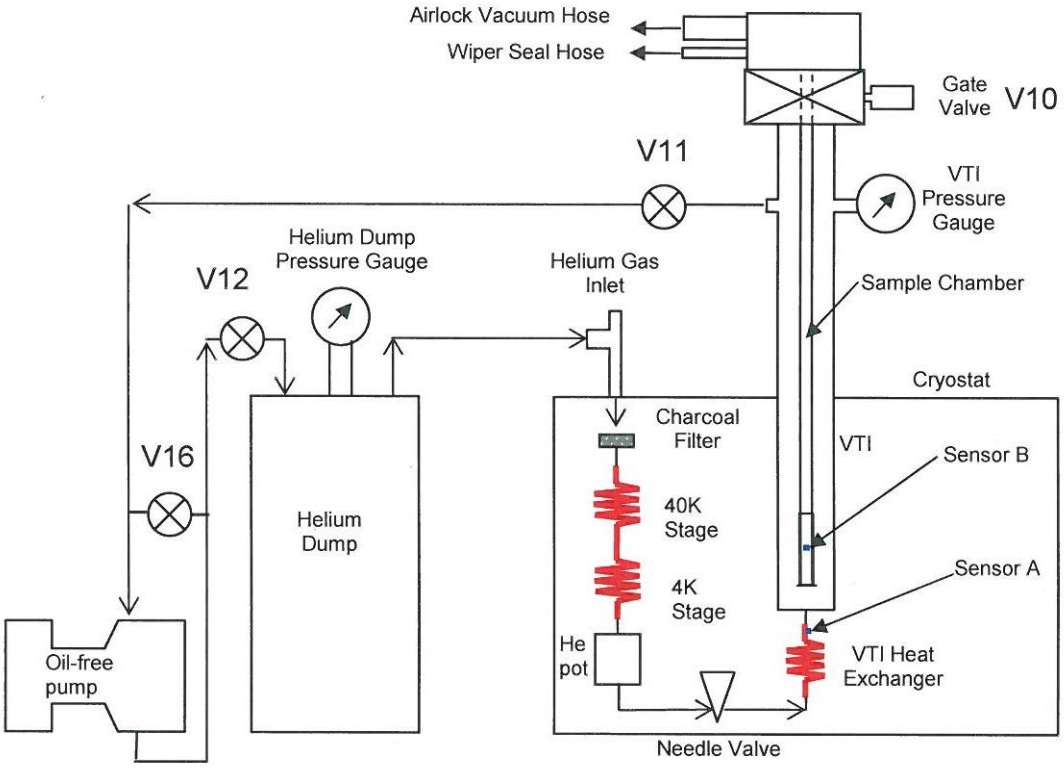

Figure 3.12: Schematic diagram of a VTI cooling circuit [37].

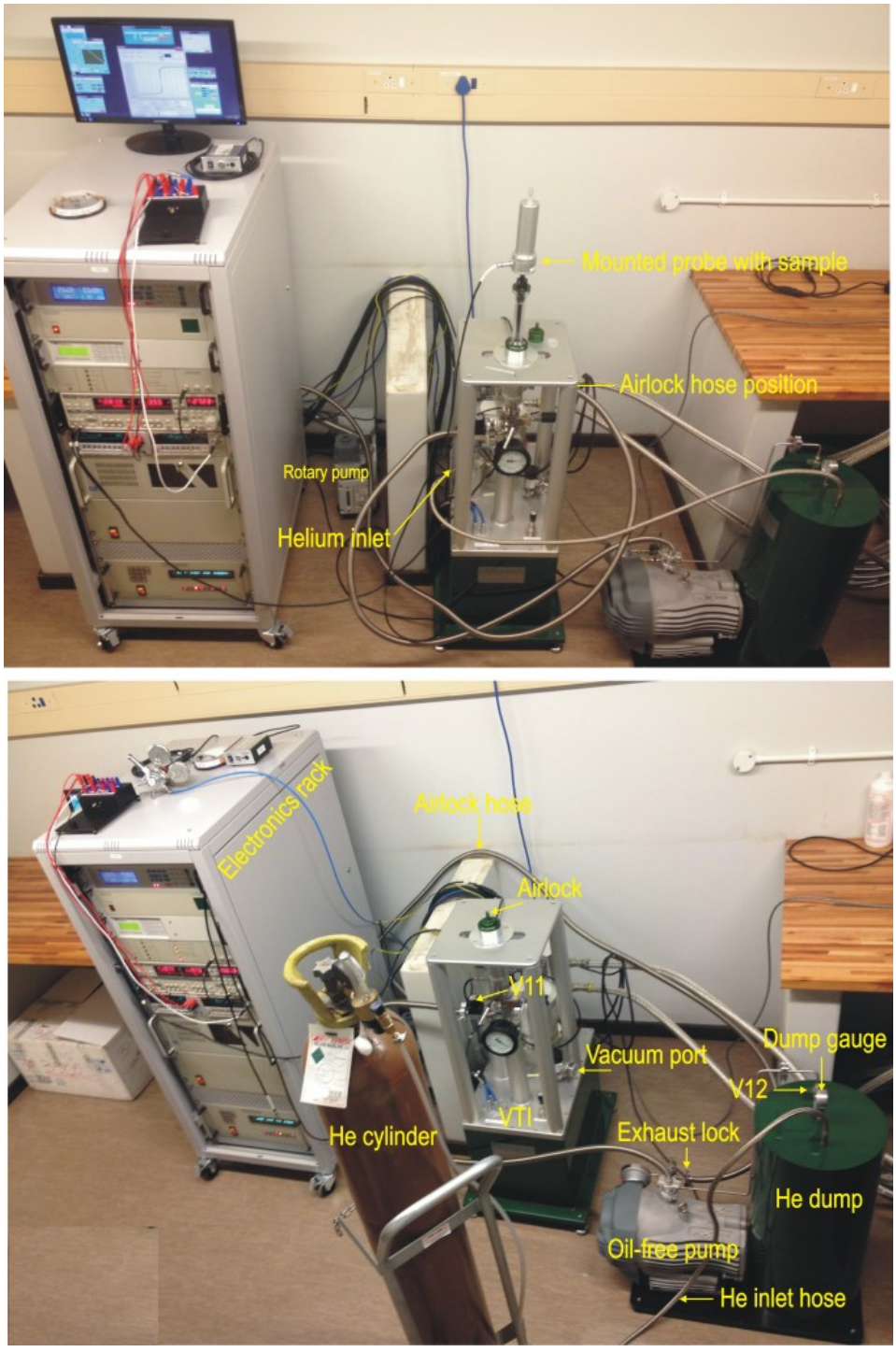

Figure 3.13: Mini cryogen-free VTI system, Condensed Matter Physics Lab (WC), UKZN.

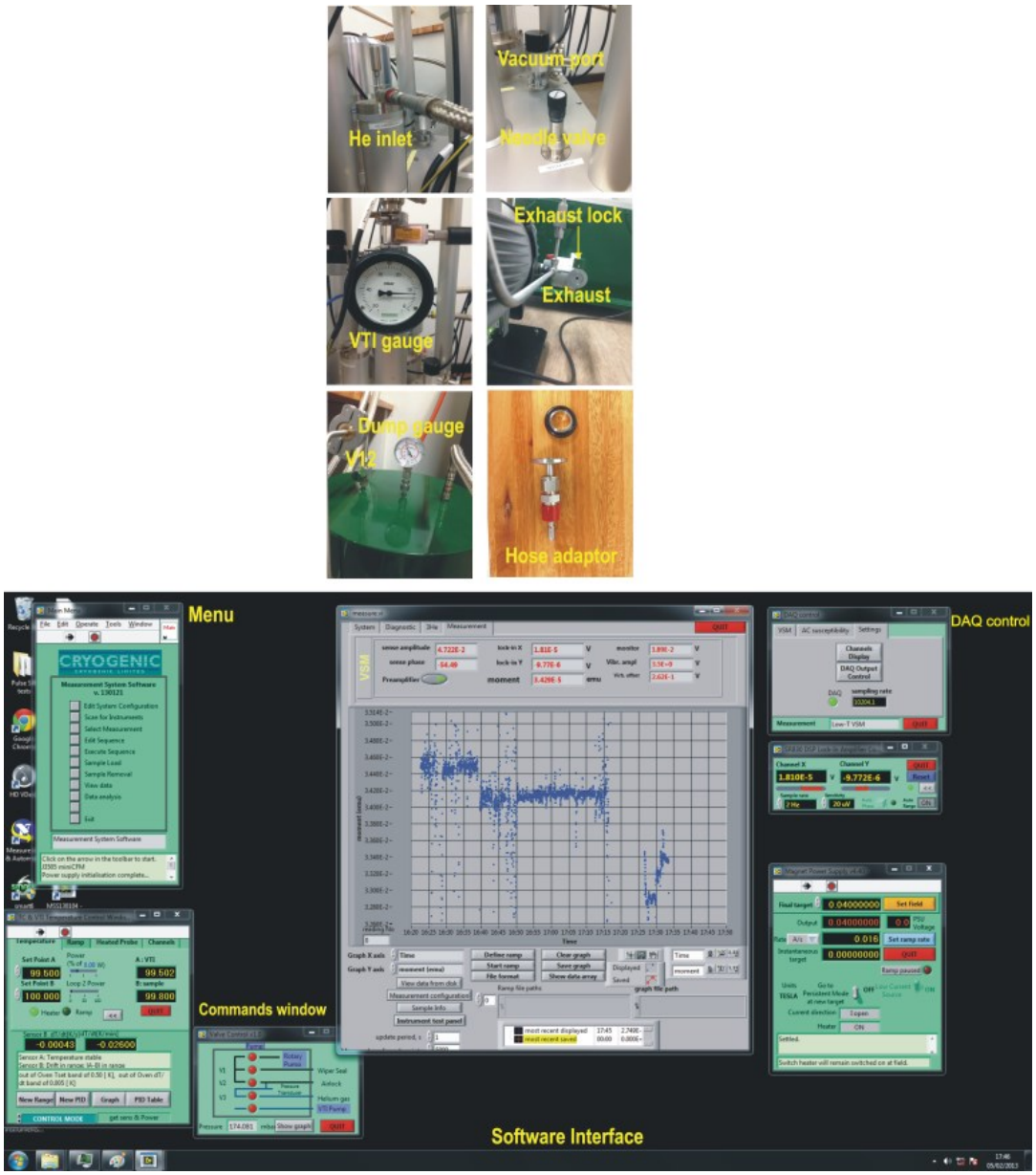

Figure 3.14: Components of the mini cryogen-free VTI system, Condensed Matter Physics Lab (WC), UKZN.

Figure 3.15: VTI VSM probe attached to a sample, Condensed Matter Physics Lab (WC), UKZN.

3.4.2.1 Evacuation procedure

To evacuate the VTI circuit and the helium inlet shown in Figure 3.12, the airlock hose in Figure 3.13 was disconnected from its position and connected to the helium inlet using the adaptor shown in Figure 3.14. This procedure evacuates the helium inlet by turning on the rotary pump and the airlock hose valve using the software commands; rotary pump and the valve V2 shown in the command window of Figure 3.14. The exhaust lock on the oil-free pump was opened and the connection between the oil-free pump and the VTI was opened by turning V11 open. The oil-free pump is turned on by using the software command; VTI pump. This allows the oil-free pump to evacuate the VTI from the top. This was allowed to run for a minimum of 6 hours. The VTI vacuum was evacuated separately by using an ultra high Vacutec pump which was connected to the vacuum port. This was pumped for a minimum of 24 hours until a pressure lower than 4.5×10^{-5} mbar was achieved. At this stage, the evacuation of the VTI circuit, helium inlet and VTI vacuum were complete. The rotary pump, airlock hose valve (V2) and the oil-free pump were turned off using the software commands. The airlock hose was disconnected from the helium inlet and re-connected to its original position (airlock hose position). The exhaust lock on the oil free pump was then closed.

3.4.2.2 Recharging the helium dump

From time to time approximately every two weeks, the helium dump needs to be evacuated and recharged with fresh helium gas. This is to ensure that only high purity helium gas (99.999%) is contained in the dump. Low temperature measurements are not possible when the helium dump is contaminated. The recharging of the dump is performed by connecting the airlock hose to the exhaust on the oil-free pump. The exhaust lock is manually opened to enable evacuation of the dump of old helium gas and contaminations. The helium inlet hose is disconnected from its normal position and connected to a fresh helium cylinder using an adaptable tubing. The helium dump lock (V12) is opened to evacuate the dump using the rotary pump. The rotary pump and the hose valve are turned on by using software commands; rotary pump and V2. The dump gauge pressure decreases drastically. The evacuation is allowed to run until a pressure of about -0.2 bar is achieved. The dump lock (V12) is closed and the helium cylinder opened to allow for fresh helium gas into the dump. The pressure in the helium dump is allowed to rise to about -0.5 bar after which the helium cylinder is closed. The V12 is again opened again to flush out the helium. This process is repeated for about 3 times to ensure that the dump is free from any possible contamination. The dump is finally recharged with the fresh helium gas up to about 0.25 bar and the exhaust lock is closed while V12 is kept opened. The airlock hose and the helium inlet hose were disconnected and reconnected back to their original positions. The sample space was flushed twice using the sample load option from the software. The VTI gauge pressure was maintained between 8 and 12 mbar by using the needle valve. However, V11 was slightly opened half way to prevent excess flow of helium gas. The cryo cooler system needs to be ramped down to 2 K so as to build up liquid helium.

3.4.2.3 Sample mount and centring

The procedure for mounting the sample probe is manually carried out by mounting the probe in the airlock space. The Low-T VSM option is selected from the data acquisition (DAQ) control window (Figure 3.14) for low temperature VSM measurements. The sample load option is selected from the menu window. This prompts

an automatic series of commands such as flushing the air space with helium gas, setting the sample space up to operating pressure and vibration of the sample rod. The centring of the sample in the CFS is critical so as to obtain the best signal sensitivity z in-between the pick up coils. A small magnetic field of 0.1 T is applied to the magnet power supply because most samples do not display a magnetic moment in zero field. The centring of sample is carried out by slowly moving the probe in-between the coil. This movement is monitored from the graphical interface of moment against time. The best moment is achieved by sliding the probe up an down to determine maximum possible moment. The sensitivity accuracy z of the centring position is verified by the auto-center command in the VSM option from the DAQ control window. The auto-center generates a curve almost sinusoidal in shape with best z value at 0.5. A value with ± 1 can be used depending on the magnetization of the sample. The key to centring the sample besides the accuracy value is to generate a good curve. After the centring of the sample, the required temperatures and fields for measurements are entered using the edit sequence command from the menu window. Finally the measurements are executed using the execute sequence command. The data is automatically saved inthe designated folder in the computer for further analysis.

3.5 Mössbauer spectroscopy

^{57}Fe Mössbauer spectroscopy is a versatile technique that is used to investigate the hyperfine interactions in iron-containing materials. The technique is able to distinguish between Fe^{2+} and Fe^{3+} ions and provides information about the magnetic state of a sample. The technique was discovered by Rudolph Mössbauer in 1957. The so-called Mössbauer effect is based on the recoilless ray emission and absorption of γ-rays in this case by ^{57}Fe isotopes. The resonant absorption is based on 2.12 % ^{57}Fe isotopes in a natural sample containing Fe atoms [24]

3.5.1 Mössbauer effect

The Mössbauer effect is the foundation upon which the spectroscopy technique is based. It relies on the excited state of ^{57}Fe after the decay of ^{57}Co by electron capture. During the decay ^{57}Fe nuclei undergo energy level transitions to the ground state. The spectroscopy is associated with emission or absorption of the 14.4 keV γ-rays by identical nuclei in the source and absorber without loss of energy [38]. The decay process is shown in Figure 3.16. The ^{57}Co nuclei decays to the ^{57}Fe excited energy state by electron capture with nuclear spin of excited state of $I_{ex} = 5/2$. This decays directly to the ground state I_g with $I_g = 1/2$ or to the excited state $I_{ex} = 3/2$ with a probability of 9 % or 91 % respectively. The transition from $I_{ex} = 3/2$ to the $I_{ex} = 1/2$ state has an energy difference of 14.4 keV. This is the transition that is associated with Mössbauer spectroscopy. During the emission or absorption of a γ-ray in a free nucleus with mass M, the nucleus recoils due to conservation of momentum with a recoil energy E_R [39] given as

$$E_R = \frac{E_\gamma^2}{2Mc^2}, \tag{3.5.1}$$

where c is the speed of light. For atoms that are bound in a crystal lattice, E_R will be very small because M in equation 3.5.1 is replaced by the mass of the crystal. The fraction of recoilless emission from a source can be obtained from the nuclei of atoms bound in solids. The recoilless fraction f is given by the equation

$$f = \exp(-\frac{E_\gamma \langle x^2 \rangle}{\hbar^2}), \tag{3.5.2}$$

where $\langle x^2 \rangle$ is the mean-square thermal displacement of the nucleus, E_γ is the γ-ray energy and $\hbar = h/2\pi$ where h is the Planck's constant. Resonance will occur when the transition energy E_T of the emitting and absorbing nucleus match exactly [40]. The E_T of an identical emitter and an absorber nuclei is expressed as

$$E_T = E_{es} - E_g = E_{es}^{'} - E_g^{'}, \tag{3.5.3}$$

where E_{es} and E_g are the excited state and ground state respectively for recoilless emission. $E_{es}^{'}$ and $E_g^{'}$ are the excited state and ground state respectively for res-

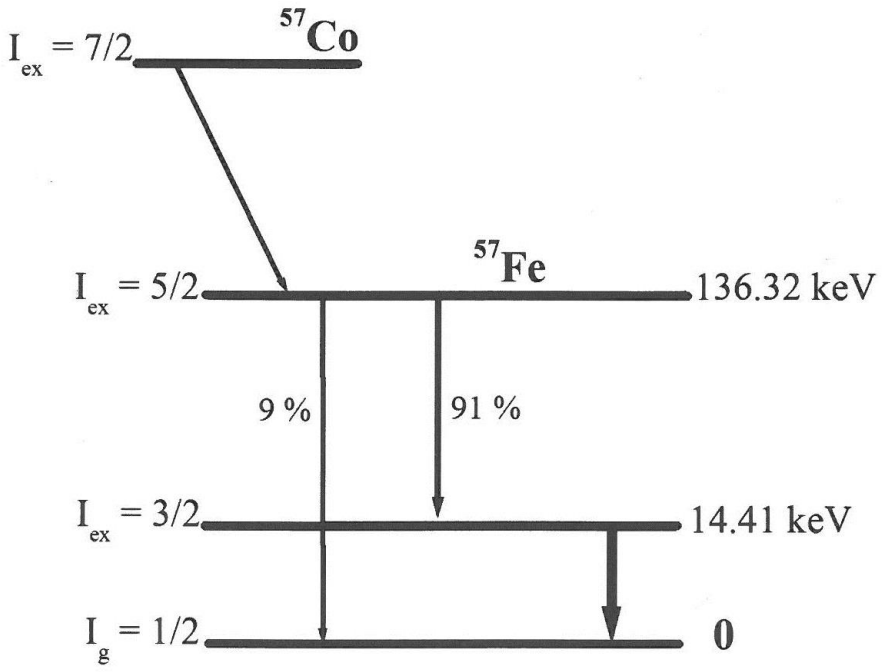

Figure 3.16: Schematic illustration of ^{57}Co nuclear decay [41].

onance absorption. Resonant absorption occurs in recoilless emission when E_T is equal to the γ-ray energy E_γ ($E_T = E_\gamma$). Figure 3.17 shows a graphical illustration of resonant absorption. The uncertainty in energy and time corresponds to the linewidth Γ of the γ-ray and the mean-life τ of the nuclear state [11] respectively. These are related to the Heisenberg relation by

$$\Gamma = \frac{\hbar}{\tau}. \tag{3.5.4}$$

When $E_R > \Gamma$, resonant absorption does not occur. Resonant absorption is therefore achieved by Doppler shifting the γ-ray energy using a vibrating source or emitter nucleus. This method is commonly used in Mössbauer experiments. The γ-ray energy of the source is easily Doppler shifted by the factor

$$\delta E = E_\gamma \frac{v}{c}, \tag{3.5.5}$$

vibrating the source with a velocity v of about 1 cm/s [38]. The Mössbauer spectrum generated is a plot of the transmitted intensity against velocity V. Information of

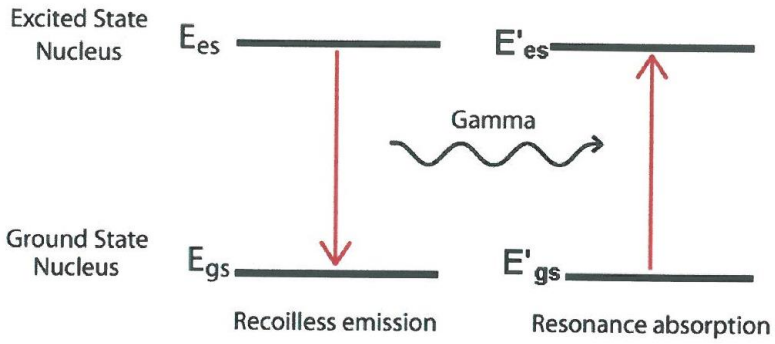

Figure 3.17: Diagram illustration of resonant absorption [42].

the magnetic state of the sample can be deduced from the analysis of the spectrum by suitable Mössbauer analysis software such as Recoil or Mosswinn.

3.5.2 Hyperfine interactions

Hyperfine interactions define the various types of interactions that exist between a nucleus and its environment. The interactions are either electric or magnetic interactions. The characteristics of these interactions can help to determine the magnetic state of a material by the information generated for the isomer shift δ, quadrupole splitting Δ and hyperfine splitting. In an ordered magnetic phase the valence state and site occupancy of iron ions can be determined.

Isomer shift δ is the change in nuclear energy levels which originates from electron charge densities different from the emitting and absorbing material [39]. This difference creates a shift in the whole spectrum either in the positive or negative direction depending on the s electron density. The shift is quoted relative to a known absorber. A 25 mCi ^{57}Co source sealed in Rh matrix was used in the current work as the γ-ray source. It was vibrated at constant acceleration and calibrated using an iron foil at room temperature. Hence the ^{57}Fe Mőssbauer spectra are quoted relative to alpha-iron. Figure 3.18 shows the shifts in nuclear energy levels and transmission spectra in the presence of an internal hyperfine field. The isomer shift in Figure 3.18 (a) can be seen to be a shift of the minimum away from zero velocity. Quadrupole splitting Δ arises due to splitting of nuclear energy levels as a result of the

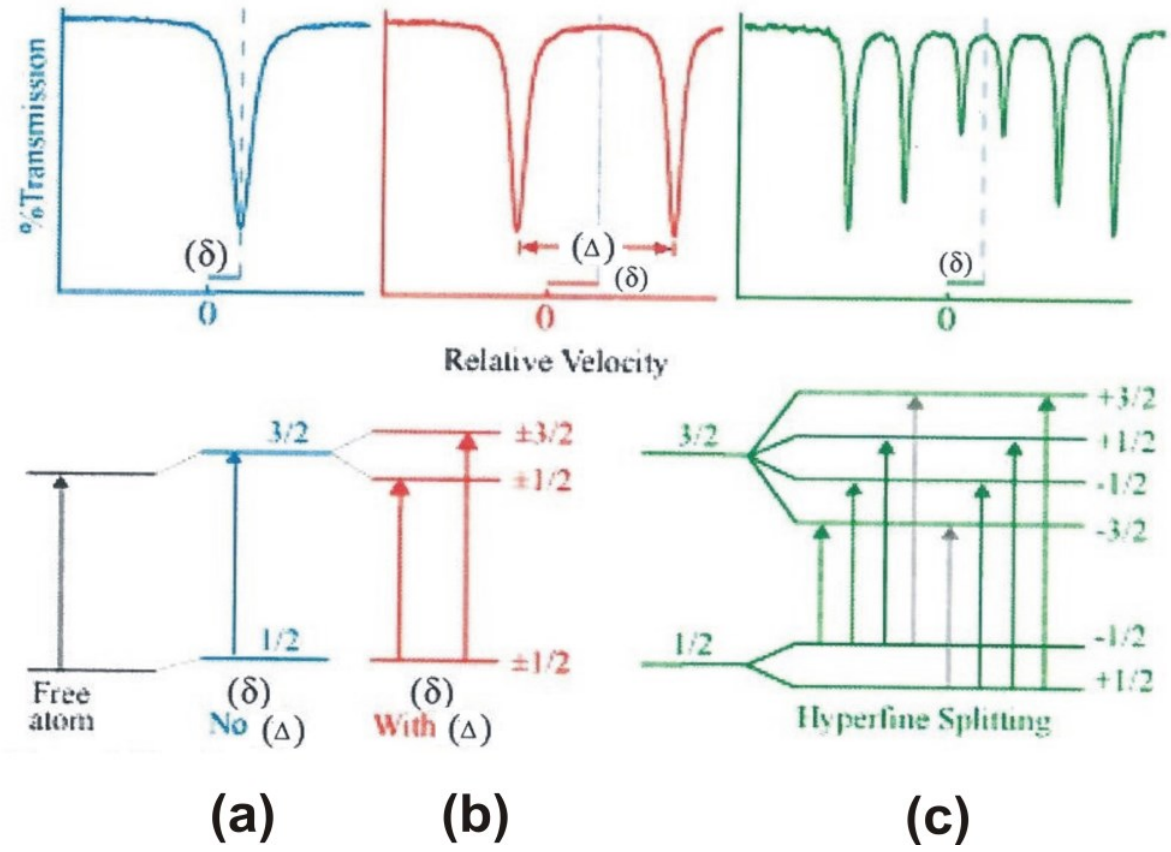

Figure 3.18: Shifts in nuclear energy levels and transmission spectra due to differences in Isomer shift δ, Quadrupole splitting Δ and Hyperfine splitting [44].

interaction of nuclear quadrupole moment with electric field gradient. This causes the individual peaks in the transmission spectrum of ^{57}Fe to split into doublets as shown in Figure 3.18 (b). The excited state with $I_{es} = 3/2$ splits into two substates as $\pm 1/2$ and $\pm 3/2$. The positions of the peaks in the sextet defines the hyperfine splitting of the nuclear energy levels. The magnitude of the splitting Δ, is related to the nuclear quadrupole moment Q and the principle component of the electric field gradient V_{zz} by

$$\Delta = \frac{QV_{zz}}{2}. \tag{3.5.6}$$

In the presence of a magnetic field at the nucleus, the splitting yields a sextet as shown in Figure 3.18 (c). This is known as the Zeeman splitting [44].

3.5.3 Experimental procedures

The Mössbauer spectroscopy used for measurements in the current work consist of an MR-351 Mössbauer drive unit (MDU), a CANBERRA amplifier, IIFAST ComTec pre-amplifier, 5 KV BIN power supply model 1000, an LND INC 45431 nuclear radiation detector and an ORTEC MCS-pci^{TM} data card with multichannel analyser (MCS) software version: 2.13 installed in a desktop computer. Figure 3.19 shows a block diagram of the Mössbauer spectrometer. A 25 mCi ^{57}Co source sealed in Rh matrix was attached to the transducer and shielded with about 1 cm thick lead block. The Mössbauer spectrometer was calibrated using an iron foil at room temperature. The MDU provides the mode of vibration of the transducer at constant acceleration to achieve resonant absorption. A sample of about 0.2 g was placed in a plastic sample holder and positioned in the sample space. The transmitted γ ray intensity corresponding to the 14.4 keV interacts with the nucleus of the sample and the transmitted rays through the sample are detected by the detector. These signals are amplified with amplifiers at high voltage (HV) and sent through a single channel analyser (SCA) which are further processed by the multi-channel analyser (MCA) for data capturing by the computer. The accumulated data are interpreted as spectra and displayed on the output screen of the computer using MCS software.

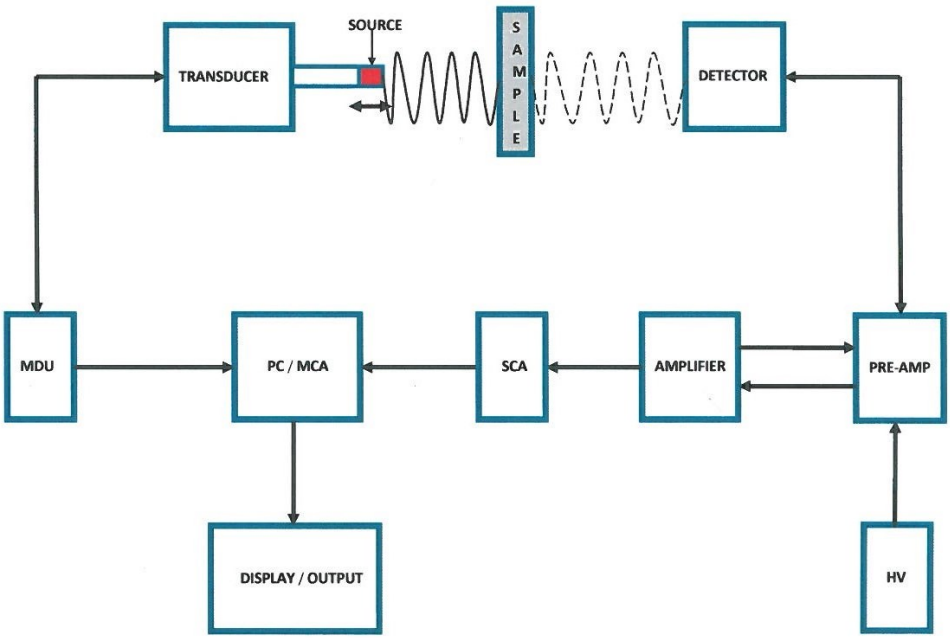

Figure 3.19: Block diagram of the Mössbauer spectroscopy used for measurements [11].

A minimum of 18 hours was allowed for data accumulation so as to generate good spectra for analysis. The spectra were fitted using recoil Mössbauer analysis software. The obtained results are discussed in Chapter 4 and 5.

Chapter 4

Structure and bi-magnetism of $CoFe_2O_4/CoFe_2$ nanocomposites

4.1 Introduction

Cobalt ferrite ($CoFe_2O_4$) is ferrimagnetic with unique properties which are suitable for fabrication of permanent magnets. This includes high crystalline anisotropy energy, high coercivity, moderate saturation magnetization, good chemical stability and wear resistance [22]. $CoFe_2O_4$ can also be reduced thermally by hydrogen gas and carbon to produce new materials [22, 45]. Complete reduction produces $CoFe_2$ alloy. $CoFe_2$ alloy is a ferromagnetic material with high saturation magnetization and low coercive field compared to $CoFe_2O_4$. Nanocomposites complexed by exchange coupling interaction between hard and soft phases of such nanoparticles create interesting and mutually compensating effects on the magnetic properties. This may lead to enhanced magnetic properties with respect to the saturation magnetization, coercivity and maximum energy product.

This chapter deals with the structural and magnetic studies of $CoFe_2O_4$ nano-ferrite, $CoFe_2O_4/CoFe_2$ nanocomposites and $CoFe_2$ alloy. The glycol-thermal method was used to synthesize the $CoFe_2O_4$ nano-ferrite which was subsequently reduced by activated charcoal (carbon fine powder) in flowing high purity argon gas as discussed in Chapter 3. The choice of activated charcoal was motivated by its relatively low cost and safety concerns compared to hydrogen gas. The use of activated charcoal

also provides a scalable means for possible large scale production of the nanocomposites and $CoFe_2$ alloys from $CoFe_2O_4$.

4.2 Results and discussions

4.2.1 X-ray powder diffraction

Figure 4.1 shows the X-ray diffraction (XRD) patterns of the as-prepared $CoFe_2O_4$ and reduced samples with activated charcoal for n_C = 0.5, 2, 4, 6 and 10. No impurity phases are detected in the parent sample, as all peaks are indexed with respect to the spinel structure (Joint Committee on Powder Diffraction Standards JCPDS No. 022-1086) associated with the space group Fd3m [46]. It is observed that as the amount of activated charcoal n_C increases, the peak intensity of the $CoFe_2$ alloy phase increases with subsequent decrease in the intensity of the $CoFe_2O_4$ spinel ferrite peaks. No $CoFe_2O_4$ peaks are observed beyond $n_C = 6$. The peaks not indexed may correspond to the intermediate phases [47] which disappears for $n_C \geqslant 6$ [22, 45]. Fe carbides are more likely to form when carbon is in a solid solution with Fe at appropriate temperatures. In the present case we have carbon in solution with ferrites. Carbide phases were not detected through XRD measurements. Reduction of the ferrites occurs instead. Our results show evidence of the systematic increase of the alloy phase at the expense of the ferrite phase. We have found no corresponding JCPDS for the nano-composites. However, the XRD peaks are indexed with respect to reported spinel structure and structure of intermetallic compounds.

The average lattice parameter, crystallite sizes and XRD density were calculated using equations 3.2.3, 3.2.5 and 3.2.4 respectively. The data are presented in Table 4.1. The X-ray density of the $CoFe_2$ alloy was obtained by assuming a bcc atomic arrangement and calculated by the formula

$$\rho_{XRD} = \frac{2}{a^3}(m_1 p_1 + m_2 p_2), \tag{4.2.1}$$

where m_1 and m_2 are the atomic mass of Co and Fe atoms respectively. The probabilities of finding Co and Fe atoms in the bcc space-lattice are assumed to be

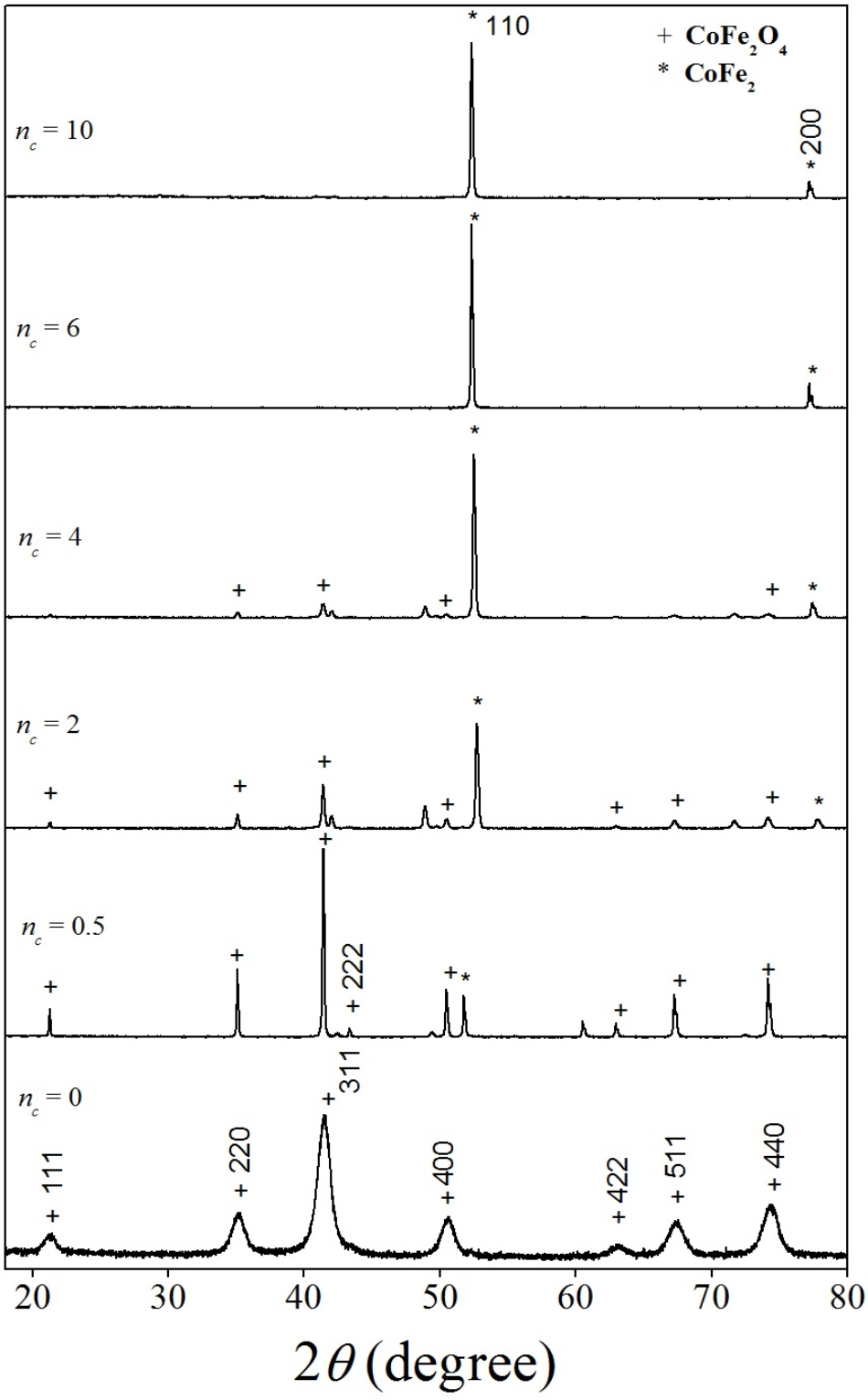

Figure 4.1: XRD patterns of $CoFe_2O_4$ reduced with n_C = 0, 0.5, 2, 4, 6, and 10.

Table 4.1: Crystallite sizes (D), lattice parameters (a) and X-ray densities (ρ_{XRD}) for as-prepared $CoFe_2O_4$ and $CoFe_2$ samples.

Sample	D(nm)	a(Å)	ρ_{XRD}(g/cm^3)
	±0.03	±0.005	±0.19
Parent $CoFe_2O_4$	9.68 from 311 peak	8.382	5.29
$CoFe_2$ at $n_C = 6$	64.83 from 110 peak	2.869	7.85

$p_1 = \frac{1}{3}$ and $p_2 = \frac{2}{3}$ respectively. The value for the lattice parameter of the ferrite sample is close to the value of 8.391 Å reported for bulk $CoFe_2O_4$ [48]. The lattice parameter value of 2.869 ±0.005 Å for $CoFe_2$ alloy at $n_C = 6$ is associated with the body centred cubic structure (Im3m space group) reported to have a value of a = 2.867 Å [49]. This supports the formation of the expected alloy phase after full reduction with activated charcoal for $n_C \geqslant 6$. Oxygen has an ionic radius of 1.40 Å which is larger than 0.65 Å for iron [50]. Hence a smaller lattice parameter is expected for the fully reduced sample compared to the parent $CoFe_2O_4$ nano-ferrite. Figure 4.2 shows the evolution of the average crystallite sizes *(D)* for $CoFe_2O_4$ and $CoFe_2$ components as a function of the reduction effect of activated charcoal calculated by the Scherrer's formula. The peak (311) for spinel structure and (110) for intermetallic compound were used for calculations for the full width at half maximum FWHM. The point of intersection shows equal crystallite sizes of the hard and soft phases corresponding to $n_C = 2$ which may be associated with a special nanocomposite phase.

4.2.2 Morphology studies

High resolution transmission electron microscope HRTEM measurements were performed for both $CoFe_2O_4/CoFe_2$ and $NiFe_2O_4$/NiFe nanocomposites. Estimates of particle sizes using both XRD and HRTEM were made for the $NiFe_2O_4$/NiFe nanocomposites only with comparable results (see chapter 5, section 5.2.2). Figure 4.3 shows the (HRTEM) images of the as-prepared $CoFe_2O_4$ nano-ferrite, $CoFe_2O_4$/ $CoFe_2$ nanocomposites and $CoFe_2$ alloy formed with different amounts of activated

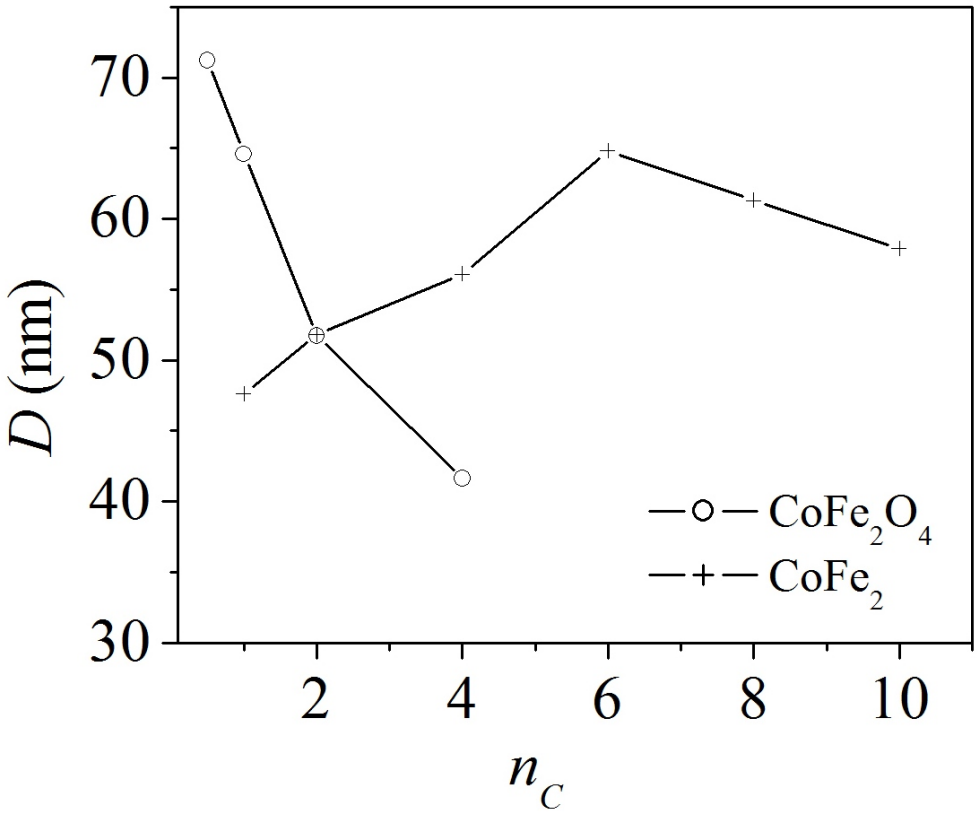

Figure 4.2: Crystallite size variations of $CoFe_2O_4$ and $CoFe_2$ phases with ratio of activated charcoal n_C.

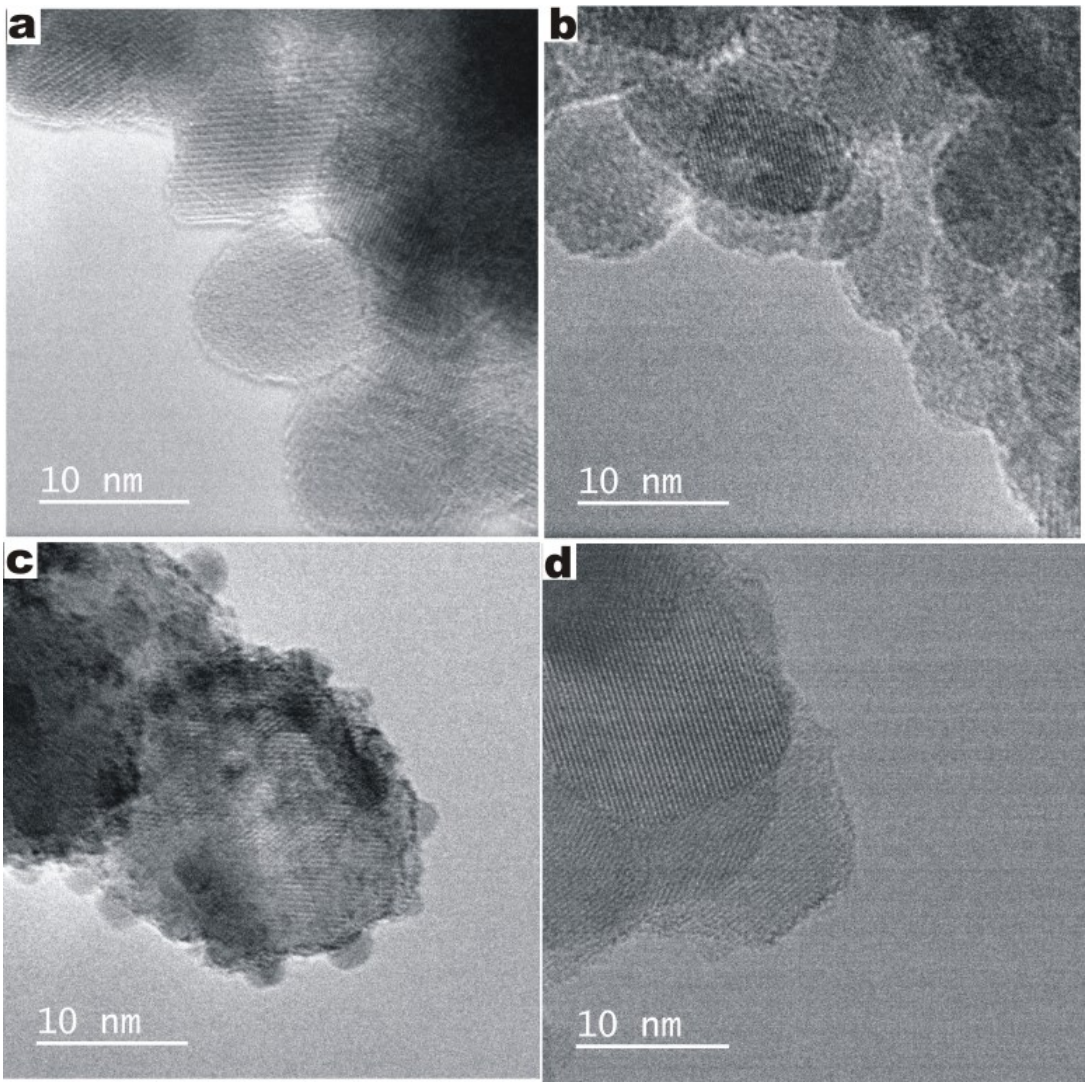

Figure 4.3: HRTEM images of (a) as-prepared $CoFe_2O_4$, (b) $CoFe_2O_4/CoFe_2$ nanocomposite at $n_C = 1$, (c) $CoFe_2O_4/CoFe_2$ nanocomposite at $n_C = 4$ and (d) $CoFe_2$ alloy at $n_C = 6$.

charcoal. The as-prepared sample in Figure 4.3(a) shows a crystalline structure with particles of almost spherical shape. This gives sharp contrast to the reduced samples in Figure 4.3(b)-(d). The particle clusters around the surface in Figure 4.3(b) is seen to have increased in numbers as shown in Figure 4.3(c). This is because the soft phase grows as more reduction takes place until the fully reduced product of $CoFe_2$ alloy which gives the best fine crystalline structure shown in Figure 4.3(d). The high resolution scanning electron microscopy (HRSEM) analysis performed on the samples also revealed the effect of reduction on the surface structure of the particles. The HRSEM images are presented in Figure 4.4. Figure 4.4 (a) shows spherically dispersed nanoparticles across the surface which differ significantly compared to reduced samples 4 (b) and 4 (c). This is not the case for the fully reduced sample in Figure 4.4(d) with images that appear to revert to spherical shapes which we can associate with the new crystalline phase of $CoFe_2$. The $CoFe_2$ alloy phase at full reduction was observed by energy dispersive X-ray spectroscopy (EDX) measurements. Figures 4.5 and 4.6 show how oxygen atoms are depleted due to the reducing effect of activated charcoal. The unlabelled peaks correspond to Au used for sample coating and the carbon tape for holding the sample.

4.2.3 Mössbauer spectroscopy

Room temperature ^{57}Fe Mössbauer spectroscopy measurements were carried out on the samples in order to observe how the spectra develop due to the reduction process by activated charcoal. The spectra reveal how the ordered phase of the nano-ferrite transform into the mixed complex phase for the nanocomposites and the ordered phase for the alloy. The spectra are presented in Figures 4.7 and 4.8 which show significant changes to the spectra with increasing n_C. This shows the power of ^{57}Fe Mössbauer spectroscopy to reveal finer details of changes in local environment of Fe atoms. The spectra for $n_C = 6$ and 8 show less mixed states of Fe atoms reflecting single phase for $CoFe_2$ alloy with the purest alloy phase obtained for $n_C = 8$. The evolution of the Mössbauer spectra does correlate with XRD results i.e. pure phases at $n_C = 0$ and $n_C = 8$ (higher symmetry) and mixed phases in between (lower symmetry). Table 4.2 shows the fitted parameters. The fits to the Mössbauer

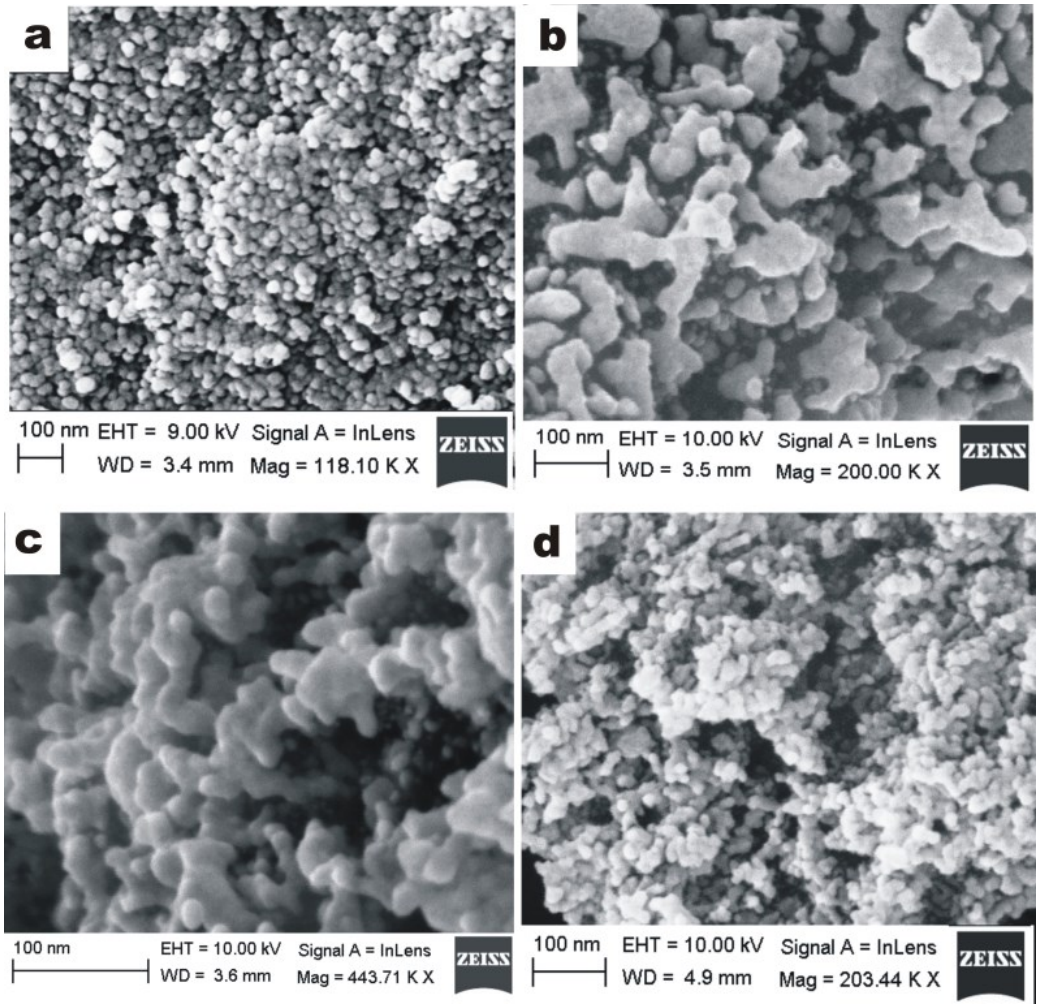

Figure 4.4: HRSEM images of (a) as-prepared $CoFe_2O_4$, (b) $CoFe_2O_4/CoFe_2$ nanocomposite at $n_C = 1$, (c) $CoFe_2O_4/CoFe_2$ nanocomposite at $n_C = 4$ and (d) $CoFe_2$ alloy at $n_C = 6$.

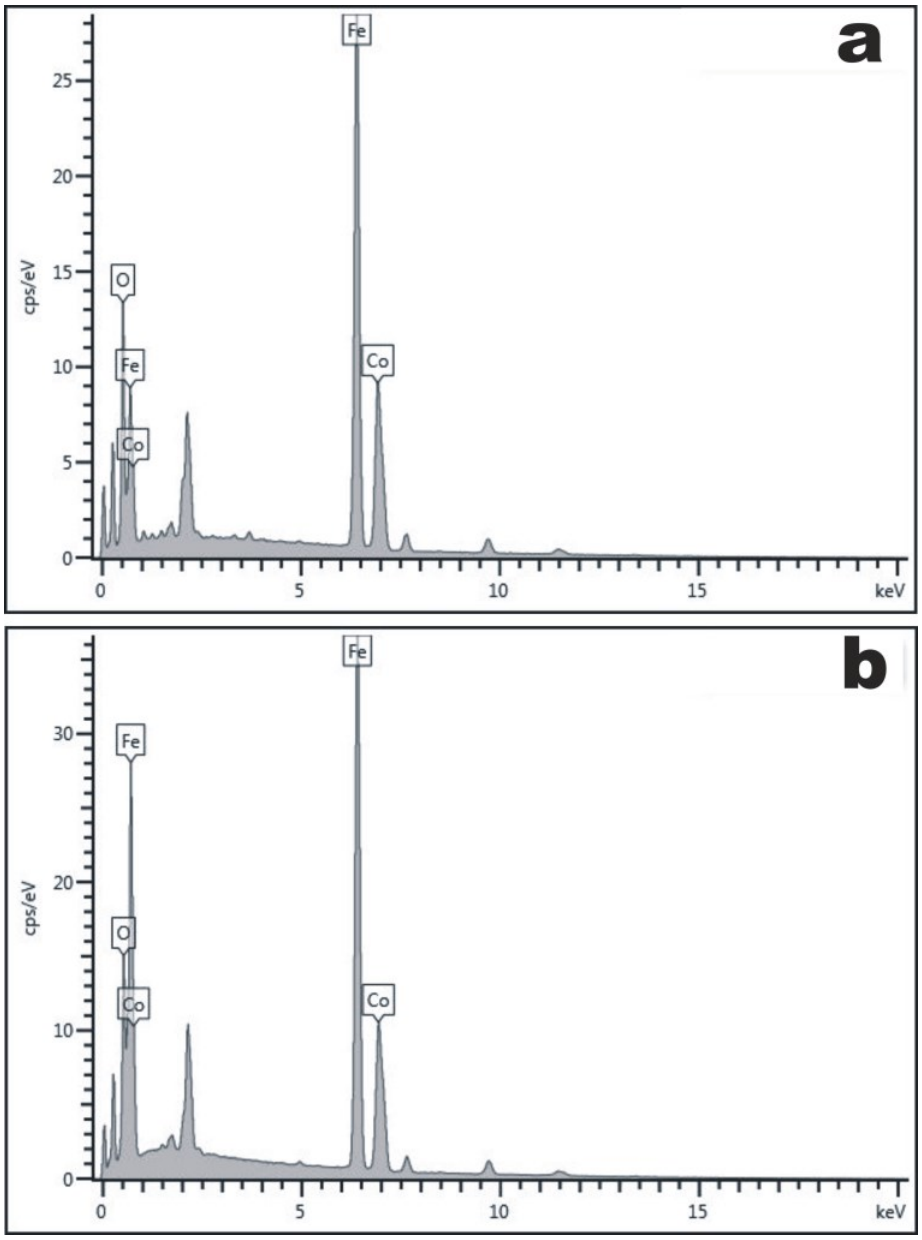

Figure 4.5: EDX spectra of samples (a) $n_C = 1$ and (b) $n_C = 2$.

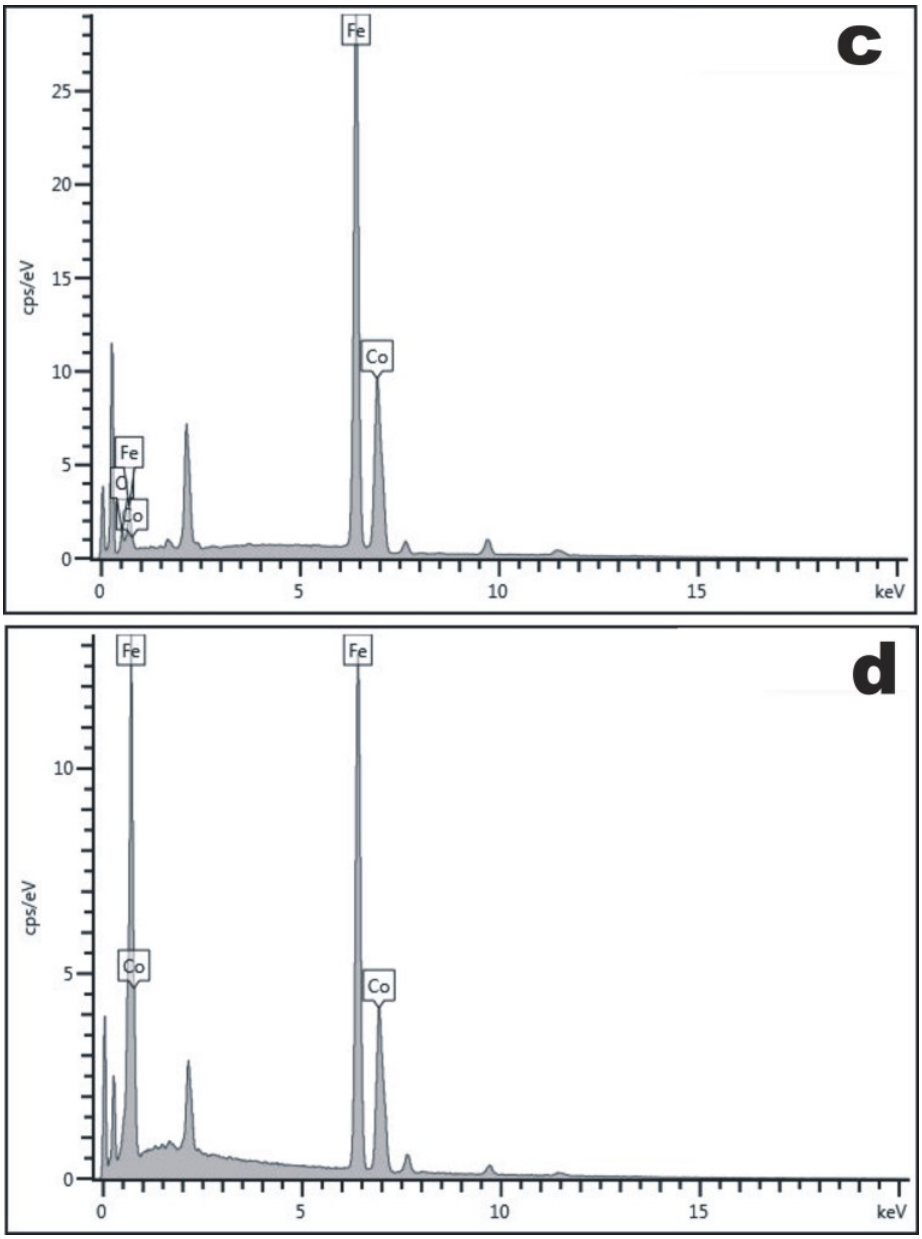

Figure 4.6: EDX spectra of samples (c) $n_C = 5$ and (d) $n_C = 6$.

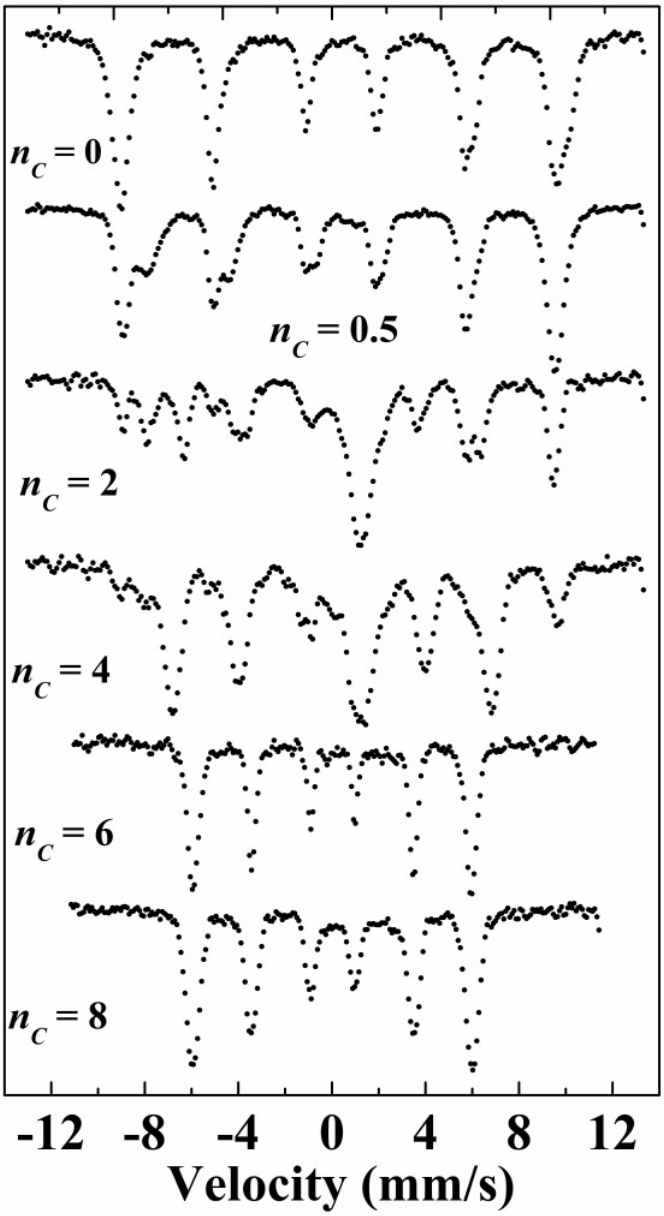

Figure 4.7: Mössbauer spectra of reduced $CoFe_2O_4$ with n_C = 0, 0.5, 2, 4, 6 and 8.

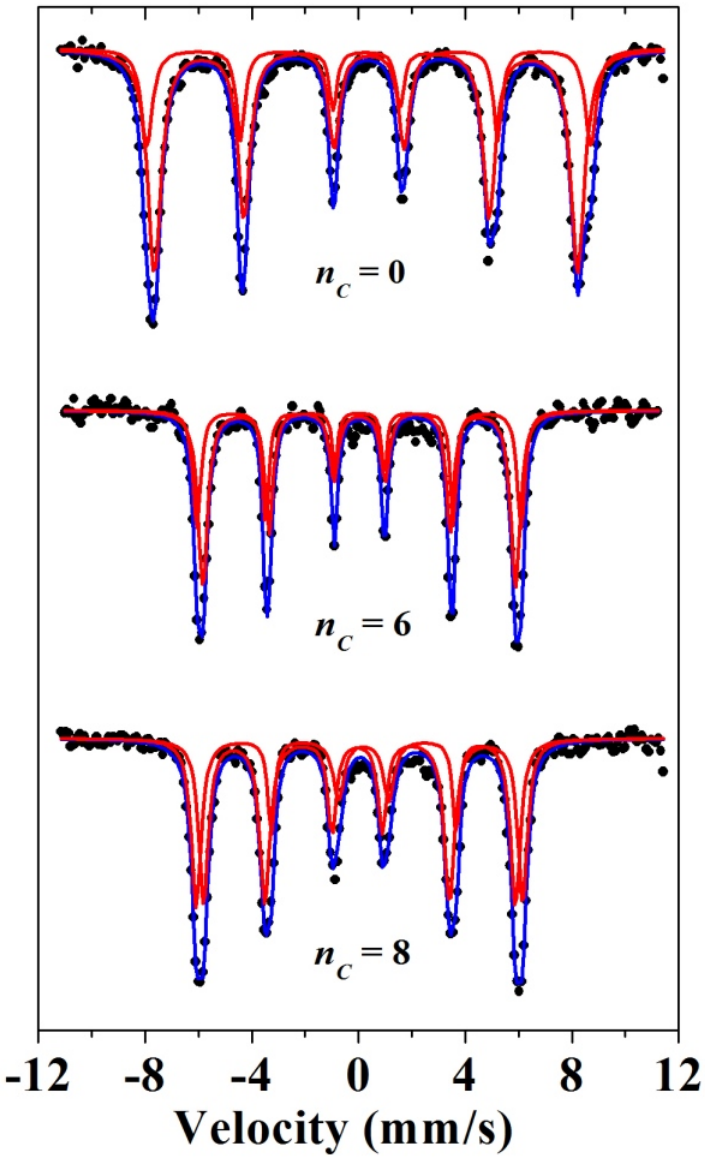

Figure 4.8: Fitted Mössbauer spectra of as-prepared $CoFe_2O_4$ nano-ferrite and $CoFe_2$ alloy formed at $n_C = 6$ and 8.

Table 4.2: Mössbauer parameters include hyperfine field (B_{hf}), isomer shifts (δ), quadrupole splitting (Δ_{EQ}), line widths (LW), fraction populations (f) and reduced chi^2 (c^2) of Fe ions of the parent sample and alloy composite at $n_C = 6$ and 8.

n_C	Sub-pattern	B_{hf} (kOe)	δ(mm/s)	Δ_{EQ}(mm/s)	LW(mm/s)	f(%)	c^2
		±1.3	±0.022	±0.019	±0.04	±2.3	
0	A	445.3	0.305	0.008	0.35	29.5	1.3110
	B	482.3	0.309	0.006	0.28	70.5	
6	C_1	377.0	0.026	-0.011	0.20	43.0	0.7601
	C_2	363.5	0.032	-0.008	0.11	57.0	
8	C_1	371.0	0.046	-0.150	0.247	42.0	1.0567
	C_2	370.7	0.061	-0.112	0.200	58.0	

spectra for the parent sample and the $CoFe_2$ alloy formed at $n_C = 6$ and 8 were deduce by two sextets using Recoil Mössbauer analysis software. The sextets for the parent sample are associated with Fe^{3+} ions at tetrahedral A-sites and octahedral B-sites of the spinel crystal structure [51]. The higher field of 482.1±1 kOe is attributed to the B-sites and A-sites to the lower field of 445±1 kOe. The isomer shift values are in the appropriate range for Fe^{3+} [52]. The sextets for the alloy phase are assumed to arise from two different sites for $CoFe_2$ corresponding to Fe atoms at the center C_1 and Fe atoms at the corners C_2 of the bcc lattice structure. The larger line width of the parent sample compared to the alloy is attributed to the electric quadrupole and magnetic dipolar effects [53, 54]. The values of the isomer shift at C_1 and C_2 for the alloy are close to 0 mm/s indicating metallic state for $CoFe_2$ [55]. The hyperfine fields are observed to decrease after reduction of $CoFe_2O_4$ to $CoFe_2$. In ferrite the interaction between magnetic moments occurs through superexchange interaction mediated by oxygen ions. This interaction is stronger in this case compared to the RKKY type of interaction expected in metallic $CoFe_2$. The hyperfine magnetic fields reported here are close to the reported values for $CoFe_2$ alloy [56].

4.2.4 Magnetization measurements

4.2.4.1 Room temperature measurements

Magnetization measurements at room temperature were performed on the as-prepared $CoFe_2O_4$ nano-ferrite, $CoFe_2O_4/CoFe_2$ nanocomposites and $CoFe_2$ alloy using the LakeShore model 735 VSM discussed in section 3.4. The magnetic properties such as coercivity H_C, saturation magnetization M_S and remanence M_R were estimated from the magnetic hysteresis loops presented in Figure 4.9. The inset in the figure is meant to illustrate evidence of finite low coercive fields in hysteresis loop measurements. The as-prepared $CoFe_2O_4$ nano-ferrite had a coercivity H_C of 0.198 kOe, saturation magnetization M_S of 32.8 emu/g and remanence M_R of 2.6 emu/g. The hysteresis loops obtained appear to show evidence of superparamagnetic behaviour associated with smaller particle sizes. Similar magnetization results for $CoFe_2O_4$ have been reported by Xing-Hua et al [57]. The data obtained for magnetization measurements are presented in Table 4.3. Significant enhancement of the saturation magnetization is observed with increasing n_C. The highest saturation magnetization of 104.75 emu/g was achieved for $n_C = 6$. This improved magnetization is attributed to the increasing inter metallic $CoFe_2$ phase. The increase in saturation magnetization M_S can be assumed as due to surface spin disorder caused by the evolution of the soft $CoFe_2$ phase [58]. The abrupt drop at $n_C = 2$ could be attributed to the formation of complex phases as indicated by the Mössbauer spectra in Figure 4.7. Beyond the optimum ratio for $n_C = 6$ of activated charcoal, dilution effect appear to set in as a continuous decrease is observed in the saturation magnetization. This loss in saturation magnetization has been attributed to surface effect [59] and the presence of non-magnetic or antiferromagnetic layer surfaces [60]. The nanocomposite of $CoFe_2O_4/CoFe_2$ at $n_C = 0.5$ of activated charcoal has a higher coercivity of 0.230 kOe with a moderate saturation magnetization of 48.8 emu/g. The variation of H_C, M_S, M_R and squareness ratio M_R/M_S as a function of reducing effect of activated charcoal n_C are shown in Figure 4.10.

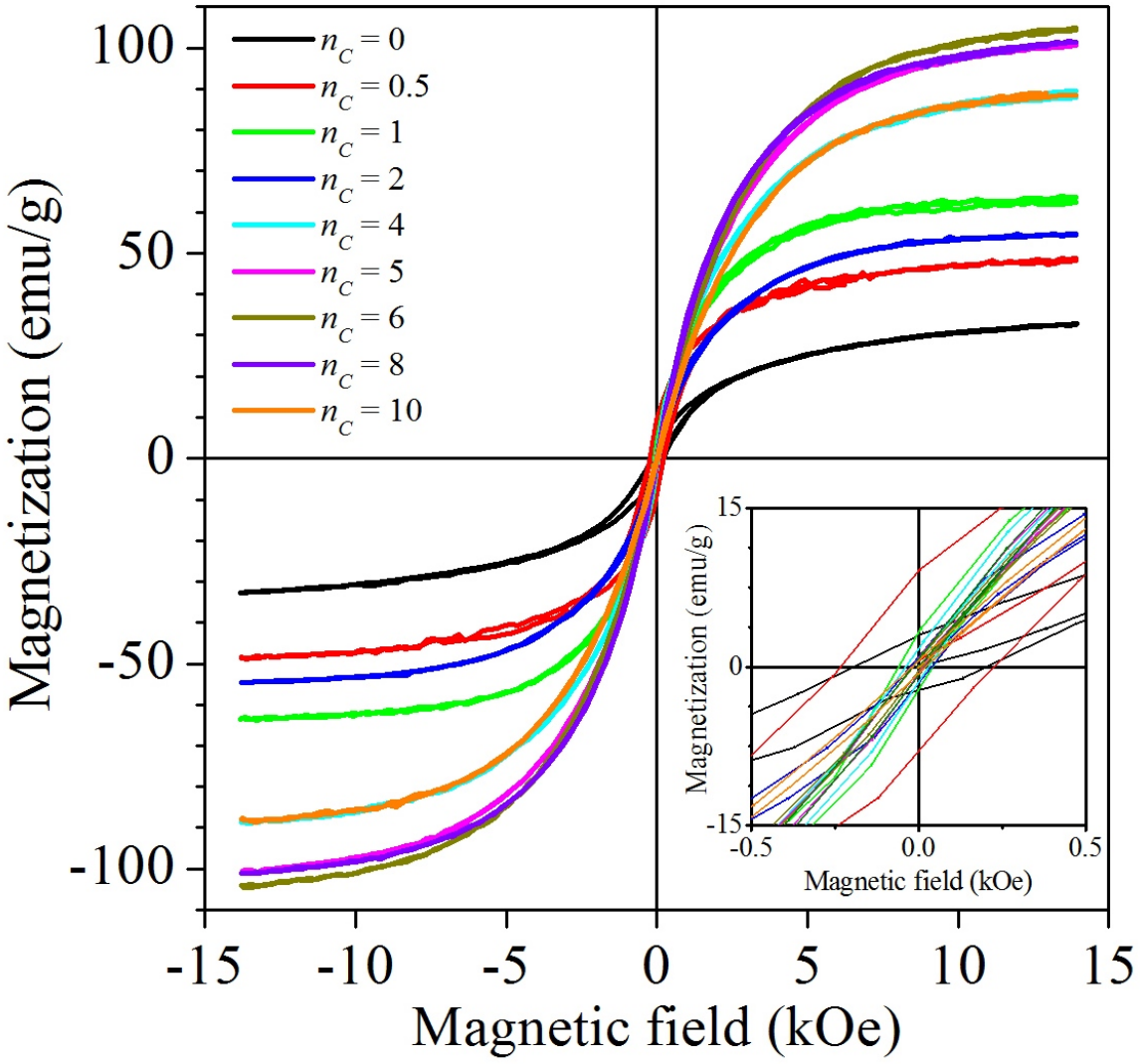

Figure 4.9: Magnetic hysteresis loops for the as-prepared $CoFe_2O_4$, $CoFe_2O_4/CoFe_2$ nanocomposites and $CoFe_2$ alloy samples measured at room temperature in applied field of 14 kOe.

Table 4.3: Coercivity H_C, saturation magnetization M_S, remanence magnetization M_R and squareness ratio (M_R/M_S) obtained at room temperatures in applied field of 14 kOe for $CoFe_2O_4$, $CoFe_2O_4/CoFe_2$ and $CoFe_2$ at different amounts of activated charcoal n_C.

n_c	H_C (kOe)	M_S (emu/g)	M_R(emu/g)	M_R/M_S
	±0.05	±0.87	±0.05	
0	0.198	32.76	2.59	0.079
0.5	0.230	48.84	8.53	0.175
1	0.051	63.85	2.71	0.042
2	0.032	54.75	1.25	0.023
4	0.035	89.24	1.58	0.018
5	0.018	101.09	0.76	0.008
6	0.131	104.75	0.52	0.004
8	0.019	101.47	0.77	0.008
10	0.021	89.40	0.61	0.007

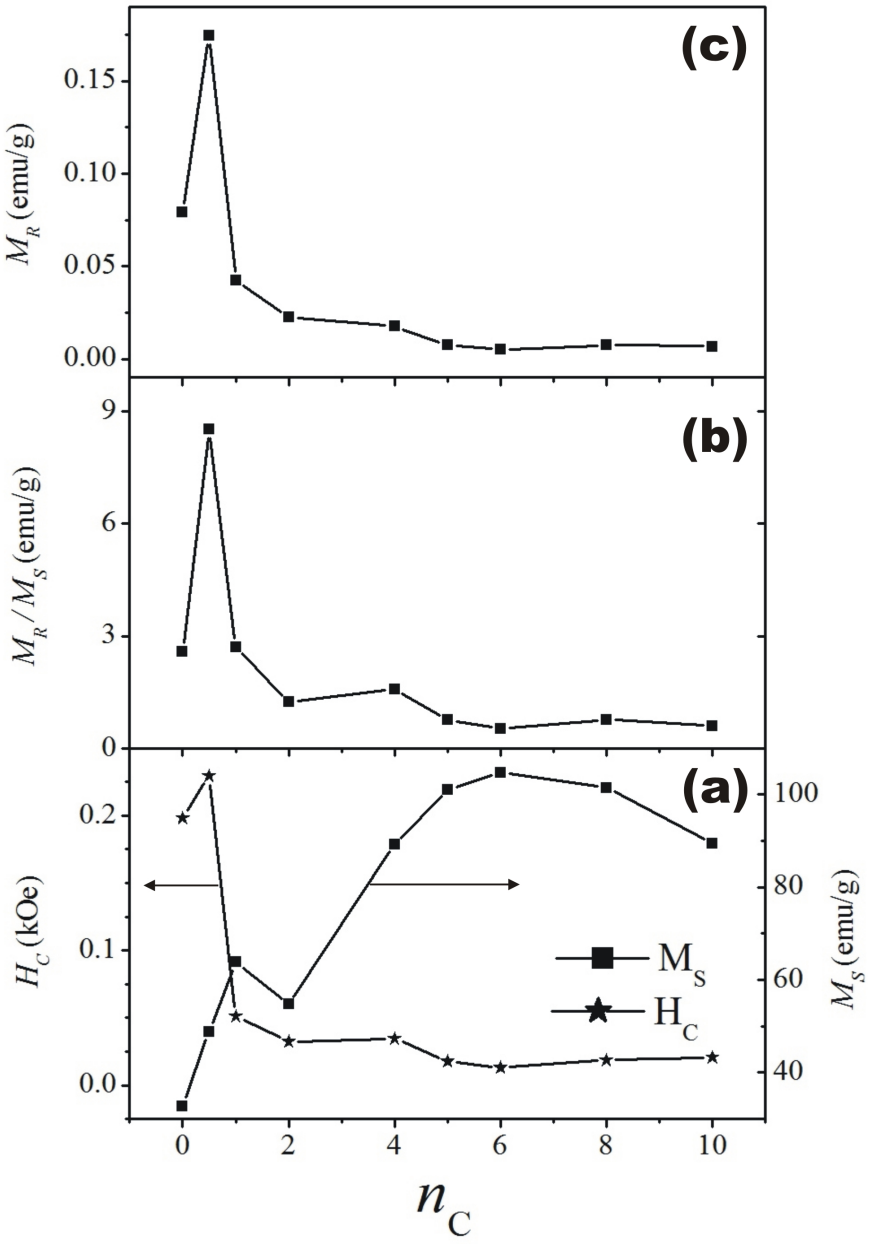

Figure 4.10: **(a)** Coercivity (H_C) and saturation magnetization (M_S), **(b)** squareness ratio (M_R/M_S) and **(c)** remanence magnetization (M_R) of reduced $CoFe_2O_4$ at different amounts of activated charcoal n_C measured in applied fields of 14 kOe.

Apart from M_S, the reduction effect on H_C, M_R/M_S and M_R follow similar trend. The results show an initial enhancement of the remanence for $n_C = 0.5$ with increased coercivity. The purer phases spinel or intermetallic compound affect domain wall movements less. XRD As the grain size of the soft alloy phase increases, a drop in the exchange length and the size of the coupled regions in the nanocomposites develops. The magnetic properties appear to be mainly determined by the dipolar interaction in the soft grains which give rise to a decrease in the remanence and in the coercive field. Comparing the crystallite size trend in Figure 4.2 with the saturation magnetization and coercivity in Figure 4.10(a), it is observed that as the crystallite size of the soft alloy phase increases, the saturation magnetization increases. The coercivity is observed to drop as the crystallite size of the hard ferrite phases decreases. The decreasing change in magnetization squareness ratio (M_R/M_S) has been attributed to long-range dipolar interactions [49]. The remanence (M_R) for $n_C = 0.5$ nanocomposites has an enhanced value of 8.53 emu/g compared to 2.59 emu/g for the parent $CoFe_2O_4$ nano-ferrite and 0.77 emu/g for $n_C = 6$ for the $CoFe_2$ alloy. Similar results have been observed in $CoFe_2O_4/CoFe_2$ microfibers [45] and FeNdB/α-Fe composites [61].

4.2.4.2 Temperature dependences measurements

Low temperature measurements were performed using the mini cryogenic free system (CFS) discussed in section 3.4. Samples for $n_C = 0$, 0.5, 5 and 6 were selected for low temperature measurements because of their optimum magnetic properties derived from room temperature measurements. However, room temperature measurements were performed on all samples using the CFS in order to take advantage of the higher saturating applied fields to 50 kOe. The magnetic hysteresis loops and the data for H_C and M_S derived from the loops are presented in Figure 4.11 and Table 4.4 respectively. The nanocomposite of $CoFe_2O_4/CoFe_2$ at $n_C = 5$ has a significantly enhanced saturation magnetization of 221 emu/g compared to 197 emu/g for $n_C = 6$ for $CoFe_2$ alloy. This was not the case when the measurements were performed in applied fields of only up to 14 kOe. More reliable values of M_S and H_C are normally deduced when measurements are performed in a saturating applied field.

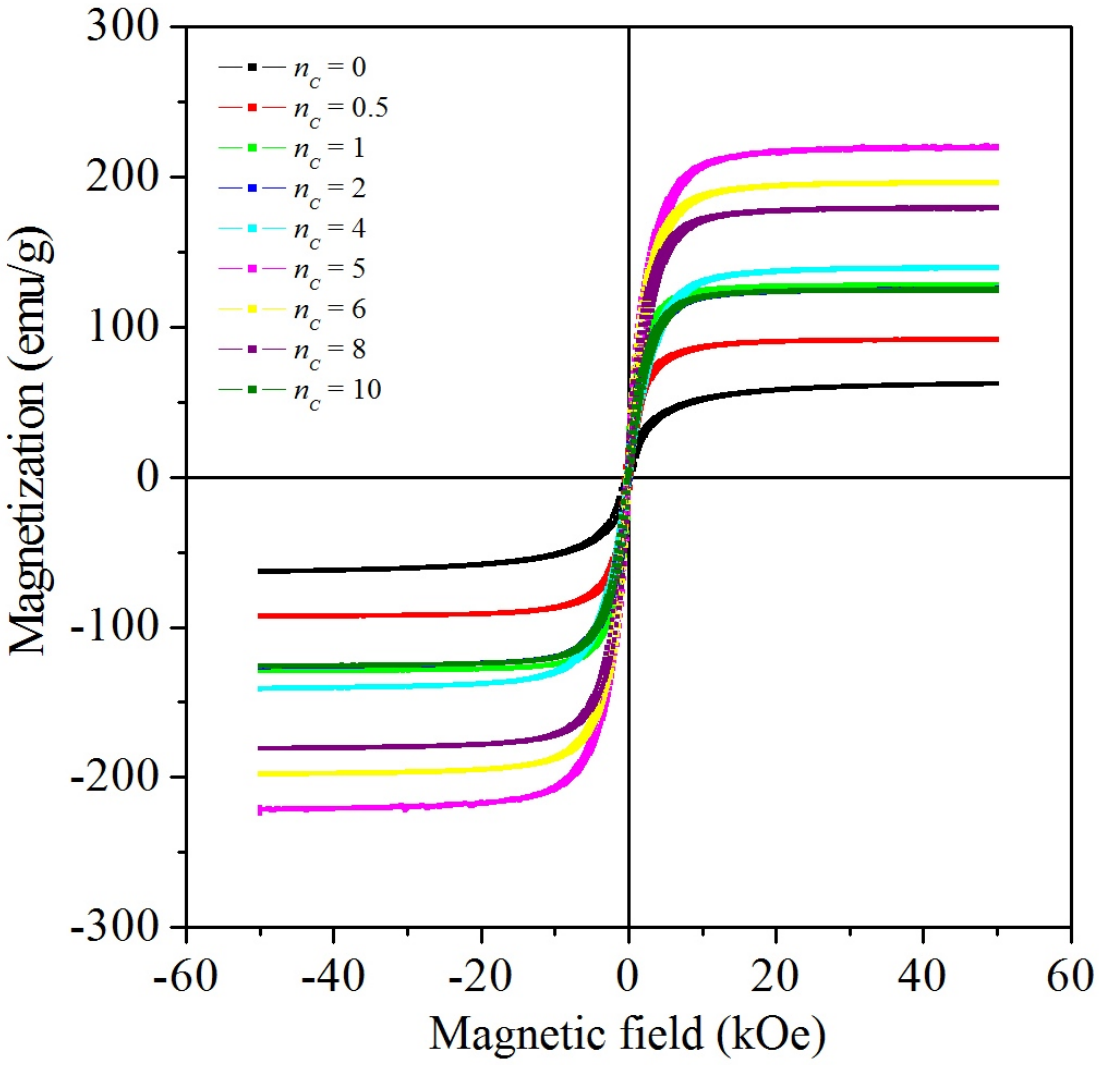

Figure 4.11: Magnetic hysteresis loops for the as-prepared $CoFe_2O_4$, $CoFe_2O_4/CoFe_2$ nanocomposites and $CoFe_2$ alloy samples measured at room temperature in applied field of 50 kOe.

Plots showing the variations of the coercive fields and the saturation magnetizations as a function of n_C are given in Figure 4.12 which we can compare with the trends obtained in Figure 4.10(a). The measurements in Figures 4.11-4.12 and Table 4.4 are for measurements in higher applied field of 50 kOe compared to 14 kOe for Table 4.3 and Figure 4.10. Similar trends are seen except that a significant increase in the saturation magnetization was achieved at $n_C = 5$ in applied fields of 50 kOe. Maximum saturation magnetization was achieved at $n_C = 6$ in applied fields of 14 kOe. This shows the enhanced magnetization properties derived from the mixed phase in the nanocomposite in high magnetic fields. Low temperature measurements were performed on the as-prepared $CoFe_2O_4$, $CoFe_2O_4/CoFe_2$ nanocomposites for $n_C = 0.5$, 5 and $CoFe_2$ alloy at $n_C = 6$. Figure 4.13 shows the corresponding magnetic hysteresis loops measured at 4 K. Low temperature measurements were done at n_C 0.5, 5 and 6 in order reveal and compare the behavior for purer phases and slightly reduced ferrites which reveal significant differences in properties. In Table 4.5 we present the results for the low temperature hysteresis loop measurements. Figures 4.14 and 4.15 show the coercivity and saturation magnetization at different measurement temperatures. The coercivity of the parent sample shows a significant temperature dependence. The nanocomposite at $n_C = 0.5$ shows a slight increase in H_C with decrease in temperature. The coercivity for $n_C = 5$ and 6 are almost temperature independent. All the reduced samples show significant enhancement of the magnetizations with respect to the parent $CoFe_2O_4$ sample. The data for the coercive field and magnetization at 4 K as a function of reduction by activated charcoal n_C are illustrated in Figure 4.16. The lines joining the points are guides to the eye. The highest magnetization of 232 emu/g at 4 K was obtained for $n_C = 5$. This is a significantly higher value of M_S compared to 75 emu/g and 203 emu/g for $n_C = 0$ and $n_C = 6$ respectively.

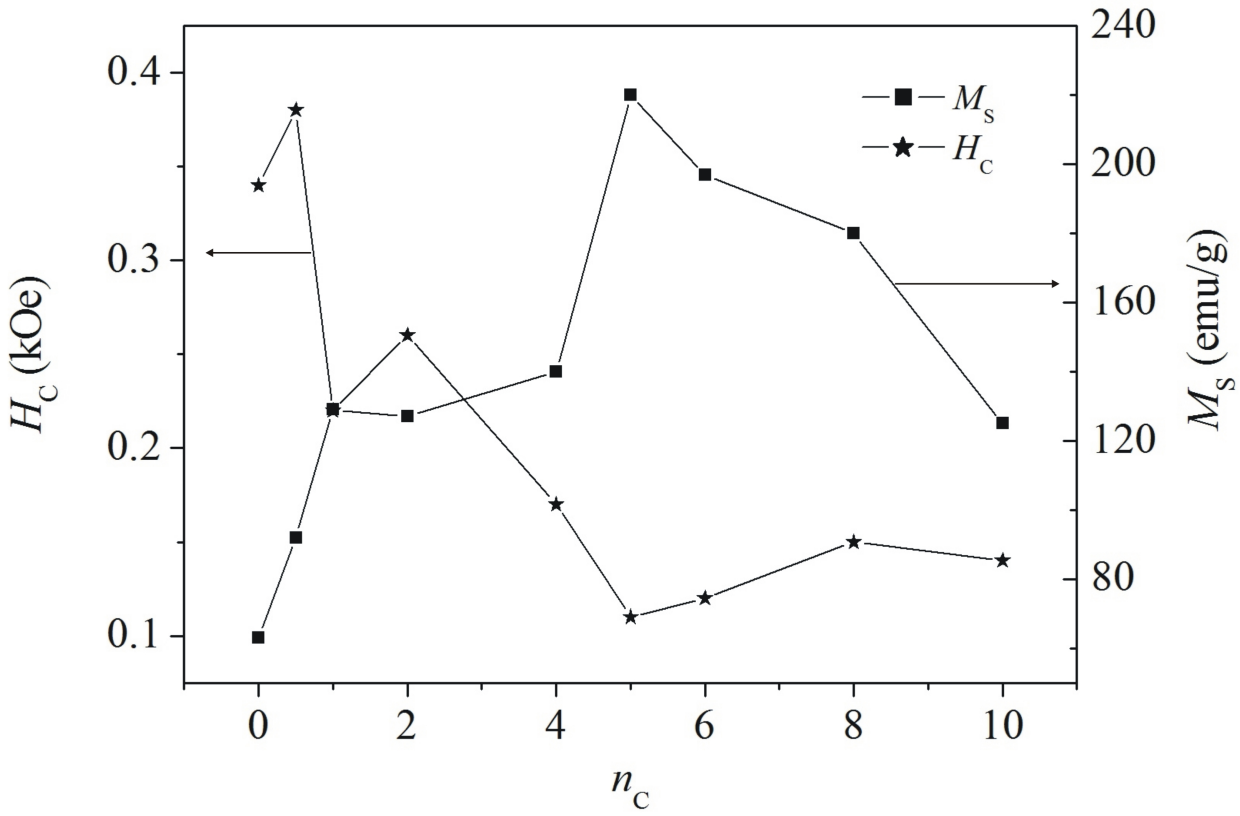

Figure 4.12: Coercivity (H_C) and saturation magnetization (M_S) of reduced $CoFe_2O_4$ at different amounts of activated charcoal n_C measured in applied fields of 50 kOe.

Table 4.4: Coercivity H_C and saturation magnetization M_S obtained at room temperature in applied field of 50 kOe for $CoFe_2O_4$, $CoFe_2O_4/CoFe_2$ and $CoFe_2$ at different amounts of activated charcoal n_C.

n_c	H_C (kOe)	M_S (emu/g)
	± 0.07	± 2
0	0.34	63
0.5	0.38	92
1	0.22	129
2	0.26	127
4	0.17	140
5	0.11	221
6	0.12	197
8	0.15	180
10	0.14	125

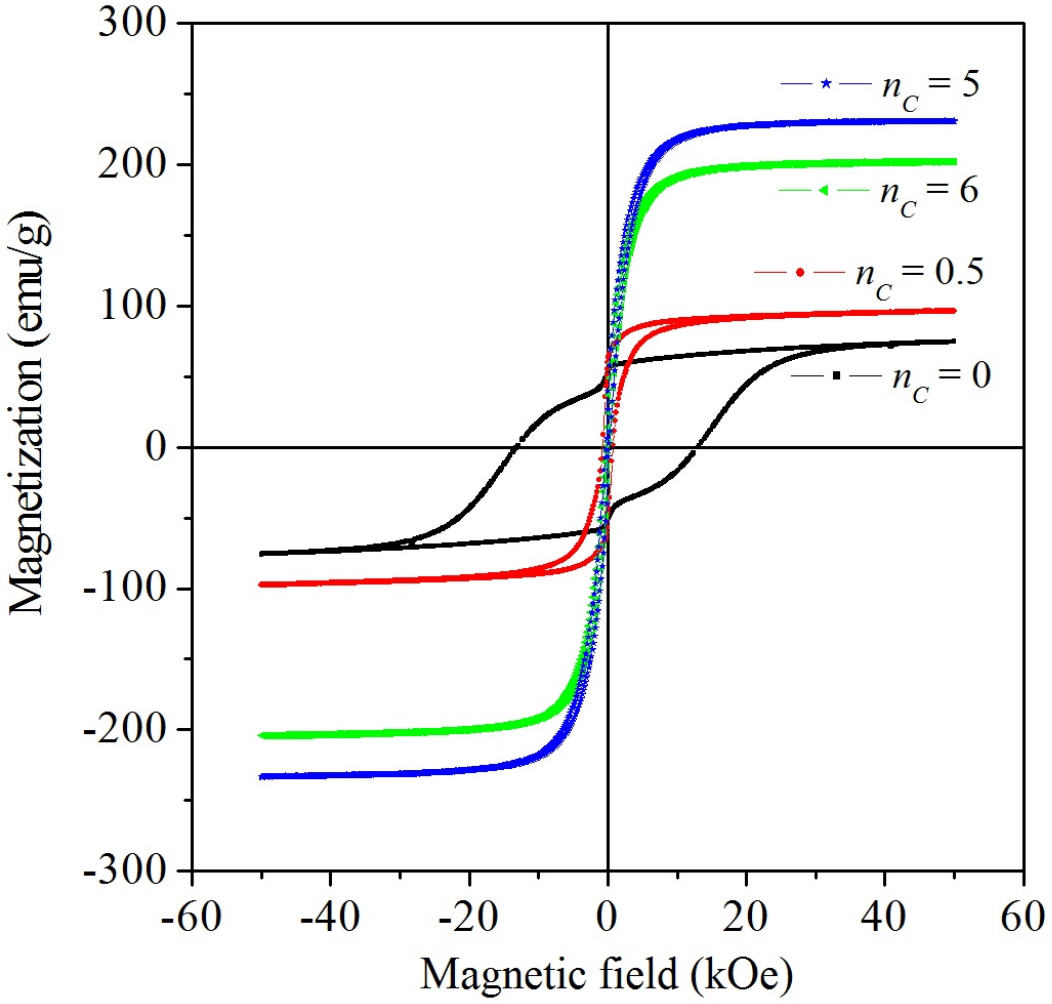

Figure 4.13: Magnetic hysteresis loops for the as-prepared $CoFe_2O_4$, $CoFe_2O_4/CoFe_2$ nanocomposites and $CoFe_2$ alloy samples measured at 4 K in applied field of 50 kOe.

Table 4.5: Coercivity H_C and saturation magnetization M_S measurements at low temperatures T, obtained for $CoFe_2O_4$, $CoFe_2O_4/CoFe_2$ and $CoFe_2$ at $n_C = 0$, 0.5, 5 and 6.

	$n_c = 0$		$n_c = 0.5$		$n_c = 5$		$n_c = 6$	
T (K)	H_C (kOe)	M_S (emu/g)	H_C (kOe)	M_S (emu/g)	H_C (kOe)	M_S (emu/g)	H_C (kOe)	M_S (emu/g)
	±0.09	±1	±0.05	±1	±0.09	±2	±0.02	±2
4	13.07	75	0.75	97	0.14	232	0.10	203
10	12.46	75	0.74	97	0.12	232	0.13	203
20	11.77	75	0.78	97	0.11	233	0.14	202
30	11.10	75	0.70	97	0.15	232	0.10	203
60	8.95	75	0.68	97	0.12	231	0.16	203
100	6.07	74	0.67	98	0.16	230	0.15	202
150	2.96	73	0.57	99	0.14	229	0.11	201
200	1.31	70	0.47	98	0.13	228	0.10	201
300	0.34	63	0.38	92	0.11	221	0.12	197

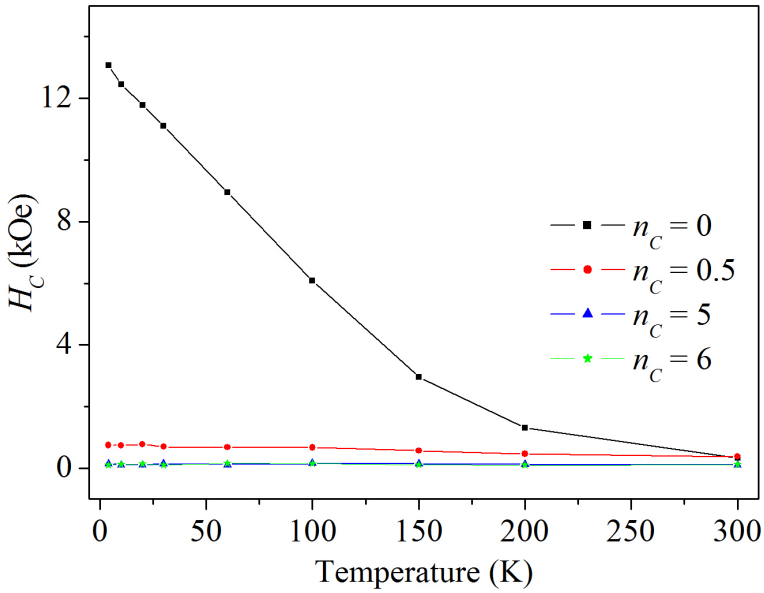

Figure 4.14: Temperature dependence of coercivity (H_C) of $CoFe_2O_4$ at $n_C = 0$, 0.5, 5 and 6.

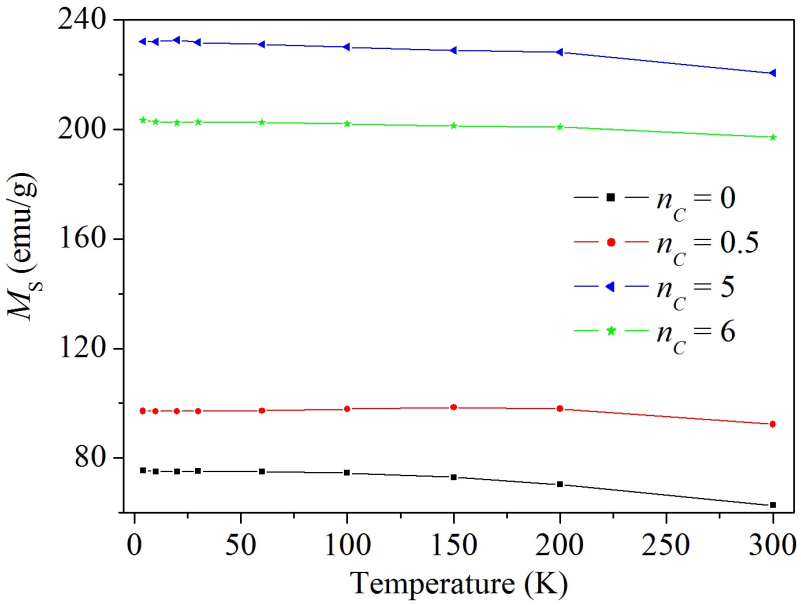

Figure 4.15: Temperature dependence of saturation magnetization (M_S) of $CoFe_2O_4$ at $n_C = 0$, 0.5, 5 and 6.

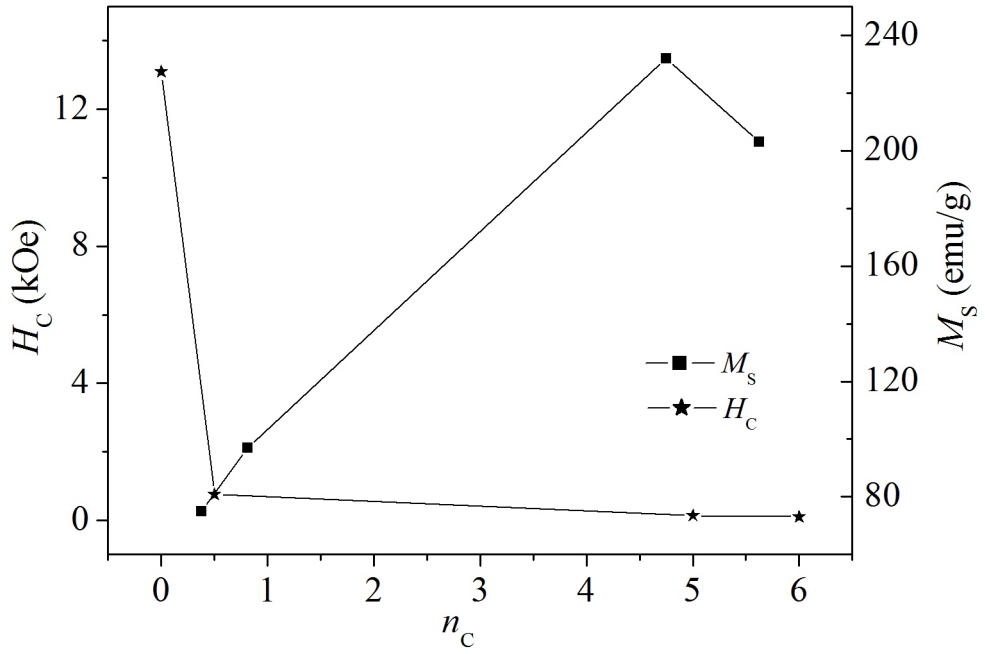

Figure 4.16: Coercivity (H_C) and saturation magnetization (M_S) of reduced $CoFe_2O_4$ at $n_C = 0$, 0.5, 5 and 6 measured at 4 K.

4.2.5 Conclusions

The XRD measurements show structural transformation from spinel to bcc structure by thermal reduction with activated charcoal. Full reduction to $CoFe_2$ alloy phase was achieved at a molar ratio $n_C = 6$ of activated charcoal as detected by XRD measurements. The high resolution transmission electron microscopy and scanning electron microscopy measurements showed clear differences between the morphology of the parent, partially reduced and fully reduced samples of $CoFe_2O_4$ nano-ferrites. Changes in the hyperfine fields of Fe atoms are revealed by ^{57}Fe Mössbauer spectroscopy. Higher fields at tetrahedral and octahedral sites are obtained in the parent $CoFe_2O_4$ sample. The reduced samples reflects different Fe-Fe co-ordinations. In addition the isomer shifts show changes of Fe^{3+} to Fe^{2+} induced by the reduction process. More collinear arrangement of magnetic moments with higher magnetization in the bcc phase is confirmed by magnetization measurements. The continuous drop of the coercive field in the hysteresis loop of $CoFe_2O_4$ to a narrow hysteresis loop for $CoFe_2$ shows that the fully reduced sample is a soft material with intermedi-

ate material obtained for the partially reduced samples. Significant enhancement of the magnetization is achieved for the intermediate $CoFe_2O_4/CoFe_2$ nanocomposites. Hence the results obtained suggest that it is possible to maximize the bi-magnetic properties of the nanocomposites.

Chapter 5

Structure and bi-magnetism of $NiFe_2O_4$/NiFe nanocomposites

5.1 Introduction

Soft ferrites are generally known to have good saturation magnetization with relatively low coercive fields. It is therefore interesting to find out how the properties of such materials are modified by reduction using activated charcoal in the formation of the nanocomposites and alloy. As before we expect that enhanced properties can be obtained when nanocomposites of ferrites and metal alloys are formed. This chapter explores the properties of $NiFe_2O_4$/NiFe nanocomposites and NiFe alloy. $NiFe_2O_4$ is a soft magnetic material [8] with Ni having much lower anisotropy effect than Co. The as-prepared $NiFe_2O_4$ was synthesized by a glycol-thermal method and reduced with activated charcoal (fine carbon powder) in flowing high purity Ar gas atmosphere as discussed in Chapter 3.

5.2 Results and discussions

5.2.1 X-ray diffraction

The X-ray diffraction (XRD) patterns for $NiFe_2O_4$ nano-ferrite, $NiFe_2O_4$/NiFe nano composites and NiFe alloy formed with various amounts of activated charcoal (n_C) are shown in Figure 5.1. The pure nano-ferrite ($n_C = 0$) conforms to the cubic spinel structure of bulk $NiFe_2O_4$ (JCPDS Card No. 10-0325) [8]. All the peaks can be indexed with respect to Miller indices (111), (220), (311), (400), (422), (511) and (440) without evidence of any impurity peaks. The lattice parameter of this compound was calculated to be $a = 8.362 \pm 0.007$ Å using equation 3.2.3 based on the (311) peak. This is close to a reported value of 8.339 Å [8]. The crystallite size of the $NiFe_2O_4$ nano-ferrite was also calculated from the prominent (311) peak using equation 3.2.5. The crystallite size was estimated to be $G = 10.48 \pm 0.08$ nm. The X-ray density of 5.3 ± 0.1 g/cm^3 was calculated using equation 3.2.4. The XRD diffraction results show that partial reduction occurs for $n_C = 1$ to 4 for activated charcoal to yield $NiFe_2O_4$/NiFe nanocomposites. The small unidentified peak close to the (311) peak for $n_C = 1$ is attributed to a possible transient impure phase which eventually disappears for $n_C > 4$. Complete reduction of the ferrite phase to NiFe alloy to form fcc and bcc phases [20] occurs for at least $n_C > 4$. The presence of FeO for $n_C = 1$ to 4 is attributed to the possibility of still unreacted iron ions in the sample crystallite interior with the carbon atoms reacting most effectively with surface nano-ferrites. In all reduced samples, NiFe alloy phase shows the coexistence of the austenite γ-Fe fcc (Ni-rich) indexed to the (111) peak and the martensite α-Fe bcc (Fe-rich) lattice structures indexed to the (110) peak [62]. Table 5.1 shows the computed data of the variation of the crystallite sizes and lattice parameters of the fcc and bcc phases in the nanocomposite and alloy. The (200) peak has a lattice parameter associated with the fcc lattice structure with a value of $a = 3.585$ Å. The value of the lattice parameter suggest the alloy composition to be Fe-Ni at 42 % Ni [63] because around this composition, the lattice parameter expands from 3.572 Å to 3.588 Å at room temperature. The (220) peak has a very low intensity and is indexed to the fcc phase. The (111) γ-Fe peak has the most predominant crystalline

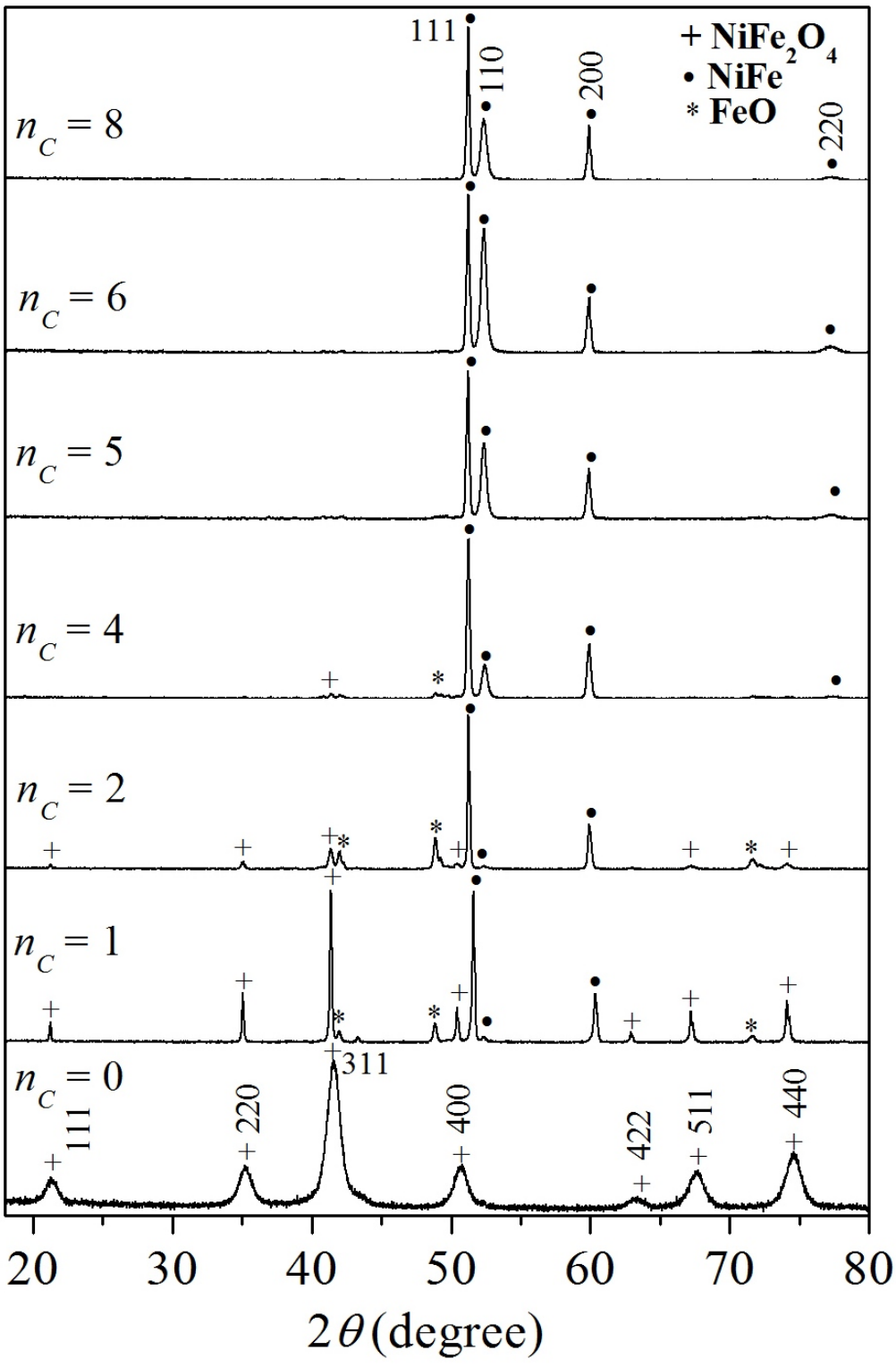

Figure 5.1: XRD patterns of $NiFe_2O_4$ reduced with n_C = 0, 1, 2, 4, 5, 6 and 8.

Table 5.1: Variation of crystallite size G and lattice parameter a of the fcc and bcc phases of NiFe alloy due to the reducing effect of the amounts of activated charcoal n_C.

	fcc phase		bcc phase	
n_C	G (nm)	a (Å)	G (nm)	a (Å)
	±0.09	±0.01	±0.09	±0.001
1	57.69	3.56	40.01	2.870
2	62.94	3.58	37.27	2.869
4	49.44	3.59	27.22	2.866
5	47.40	3.59	27.46	2.869
6	48.97	3.59	27.39	2.869
8	53.36	3.59	25.17	2.869

phase with no obvious change in peak growth compared to the bcc α-Fe phase. The crystallite sizes of γ-Fe and α-Fe nanoparticle were calculated from the (111) and (110) peaks respectively. The crystallite size of the bcc phase is smaller and decreases continually while that of the fcc phase is bigger as shown in Figure 5.2(a). The coexistence of the bcc and fcc phases give these nanocomposites and alloys a plasticity and lattice resistance to deformation advantage because fcc structure favors plasticity while bcc structure favors lattice resistance to deformation [64]. Such NiFe particles have a higher resistance to oxidation than separate Fe and Ni particles [62]. The lattice parameters of the bcc and fcc phases as a function of activated charcoal molar ratio are presented in Figure 5.2(b). The average values are close to the reported values of 2.87 Å and 3.52 Å respectively [20, 62]. The lattice parameter plot is made in nanometers so as to give a sharp contrast of the differences in values.

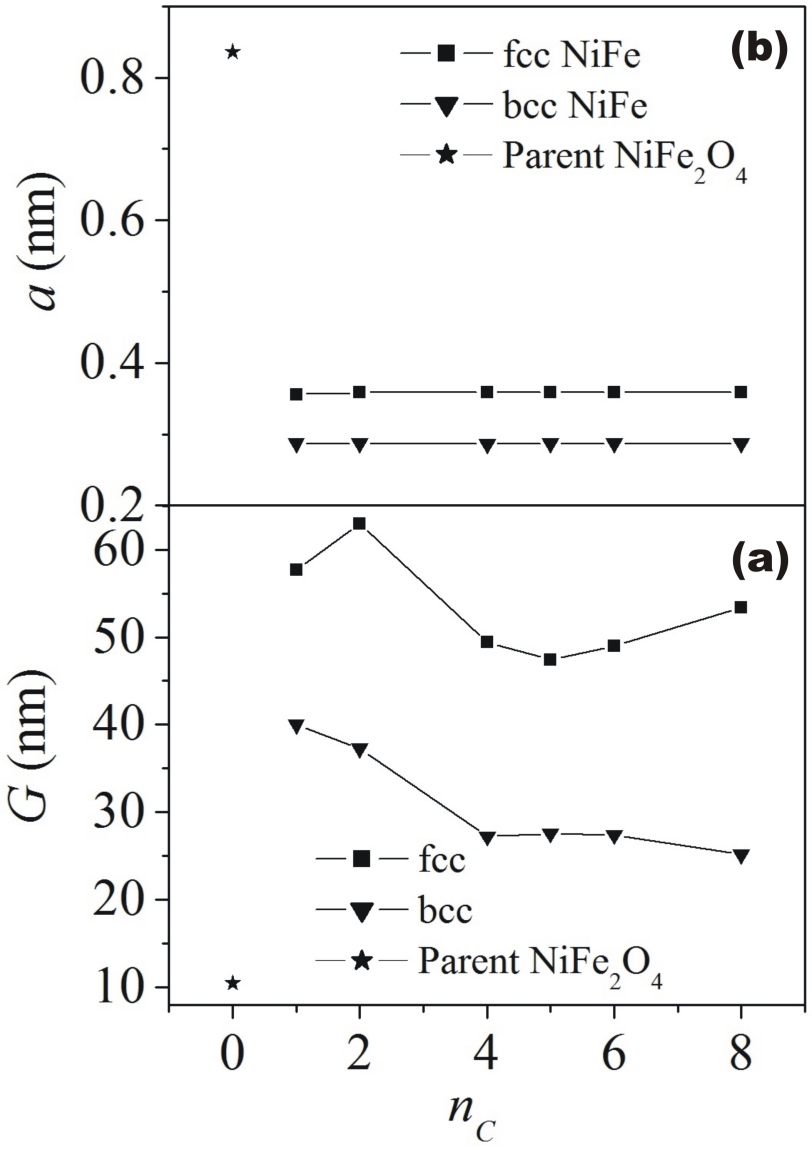

Figure 5.2: Variations of **(a)** crystallite size G and **(b)** lattice parameter a of the parent $NiFe_2O_4$, the bcc and fcc phases of the reduced samples at different amounts of activated charcoal n_C.

5.2.2 Morphology study

High resolution transmission electron microscopy HRTEM images of the as-prepared $NiFe_2O_4$, of $NiFe_2O_4$/NiFe formed at $n_C = 2$ and the NiFe alloys formed at $n_C = 5$ and 6 for activated charcoal are presented in Figure 5.3. The as-prepared sample in Figure 5.3(a) shows almost spherical particle shapes. The HRTEM morphologies of the reduced samples show contrasting images compared to the parent sample. The particle sizes were estimated from the HRTEM particle distribution shown in Figure 5.4. About 85 particles were counted for the distribution. The result show a bi-modal particle size distribution of the parent sample in the range of about 6.5 - 11.5 nm. The estimated arithmetic average of the crystallite sizes is about 9.6 nm. This is close to the crystallite size deduced from XRD measurements.

The surfaces of the as-prepared nano-ferrite ($n_C = 0$), nanocomposites formed at $n_C = 2$ and alloys formed at $n_C = 5$ and 6 were examined by high resolution scanning electron microscope HRSEM as shown in Figure 5.5. The as-prepared sample is observed to consist of rough spherical particles which are less compact compared to the reduced samples. The nanocomposites are more compact with significant growth in the size of the particles. For $n_C = 5$ and 6 the particles are more closely packed which we attribute to the presence of the NiFe alloy phase with higher density due to the presence of the fcc phase [63]. Similar images but less compacted were observed for FeNi alloy synthesised by chemical co-precipitation method [20]. The presence of the NiFe alloy phase at full reduction was observed by energy dispersive X-ray spectroscopy measurements. Figures 5.6 and 5.7 show how oxygen atoms are depleted due to the reducing effect of activated charcoal. The spectra displayed in the figures show the elemental compositions corresponding to $n_C = 0$, 1, 4 and 5. As before the labels for the peaks for Au used for sample coating and the carbon tape for sample holding are not indicated in the figures.

5.2.3 Mössbauer spectroscopy

^{57}Fe Mössbauer spectra measurements were performed at room temperature. The spectra for $n_C = 0$ to 6 of activated charcoal are shown in Figure 5.8. The figure

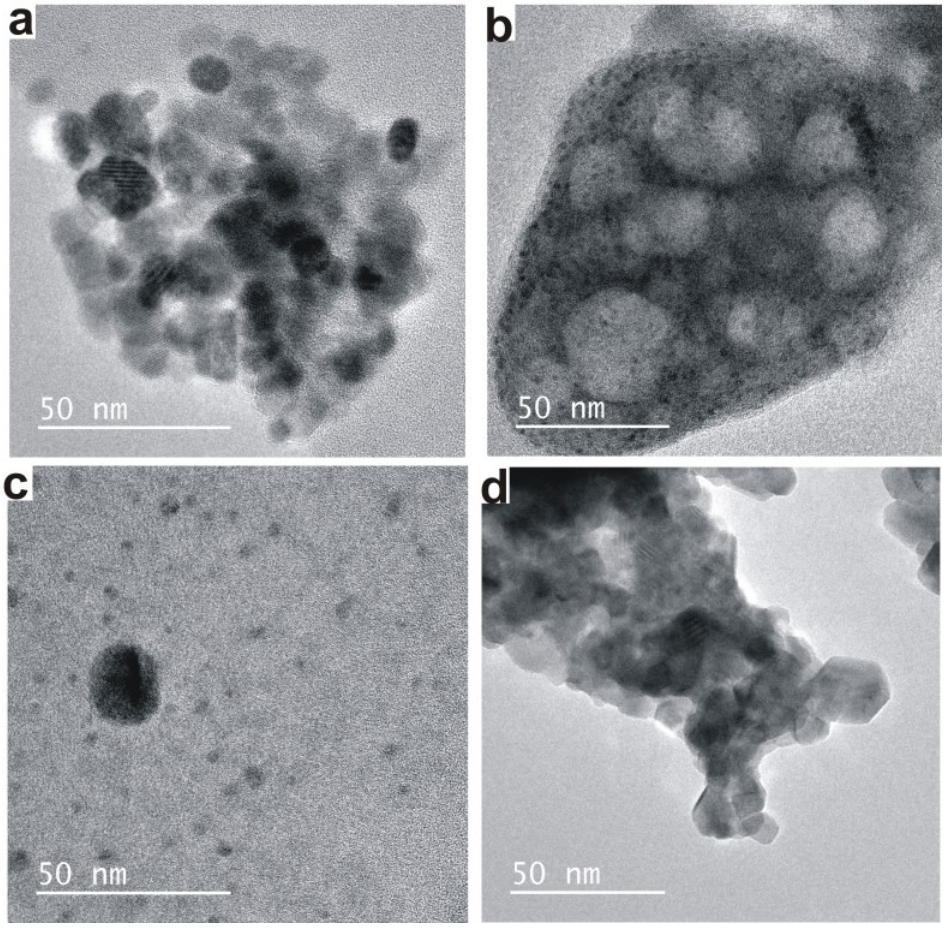

Figure 5.3: HRTEM images of: (a) the as-prepared $NiFe_2O_4$, (b) $NiFe_2O_4$/NiFe at $n_C = 2$, (c) NiFe at $n_C = 5$ and (d) NiFe at $n_C = 6$.

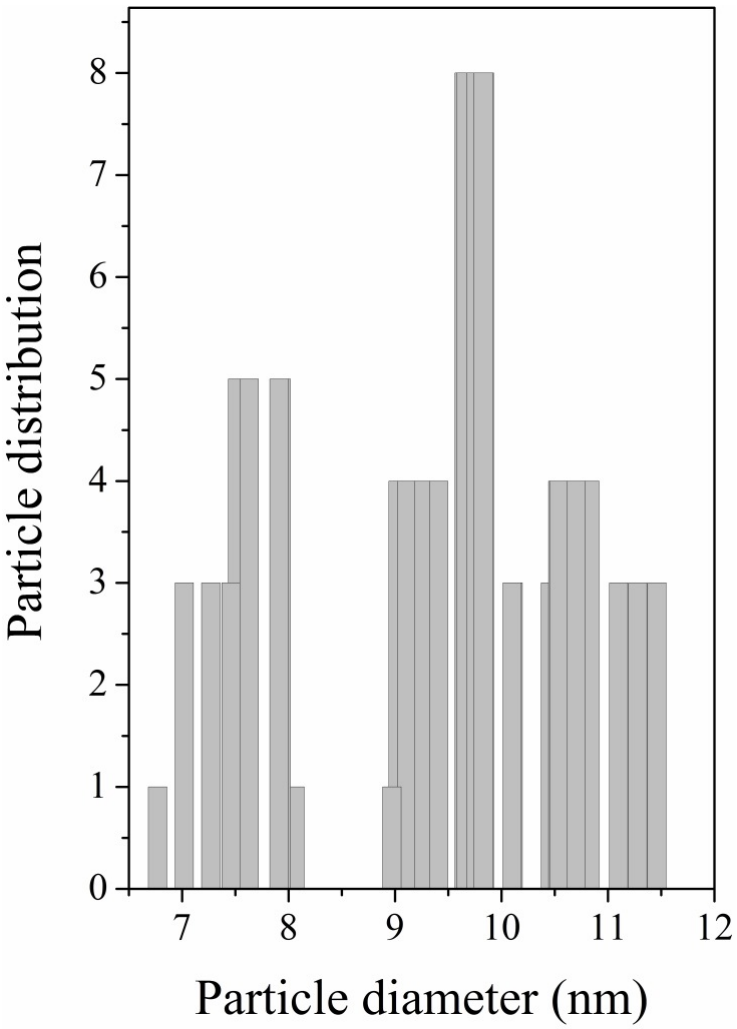

Figure 5.4: Particle size distributions of $NiFe_2O_4$ nano-ferrite.

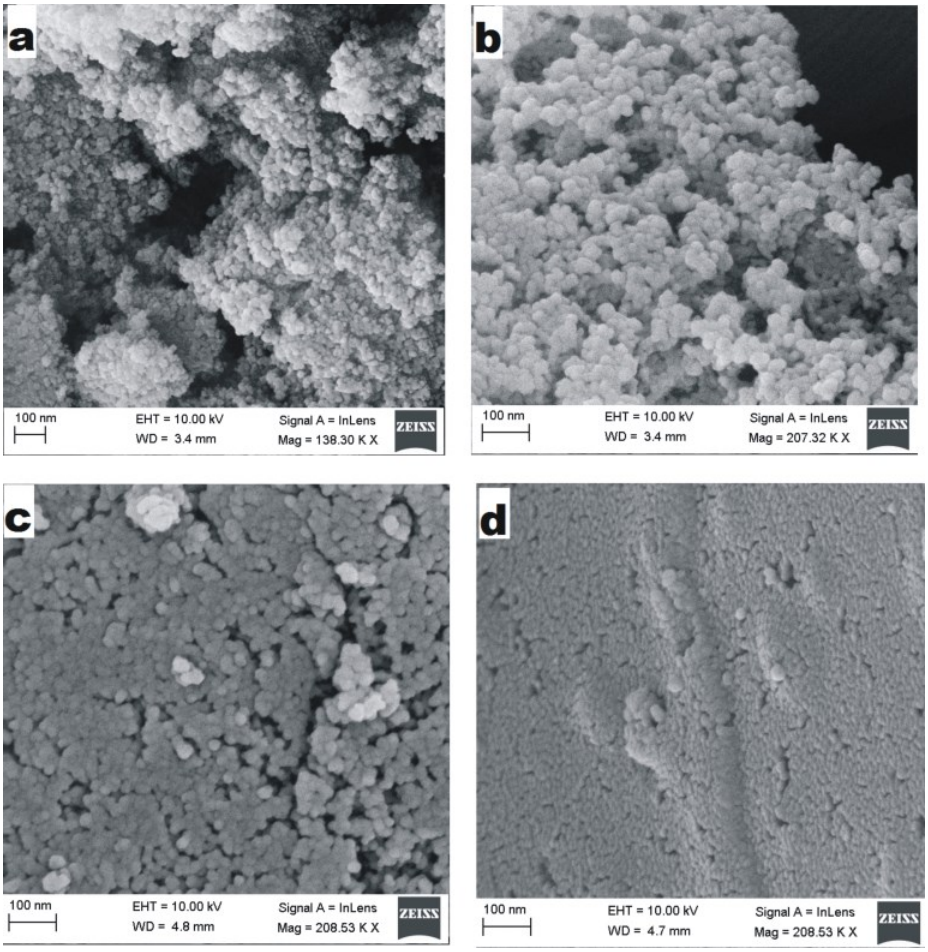

Figure 5.5: HRSEM morphology of: (a) the as-prepared $NiFe_2O_4$, (b) $NiFe_2O_4$/NiFe at $n_C = 2$, (c) NiFe at $n_C = 5$ and (d) NiFe at $n_C = 6$.

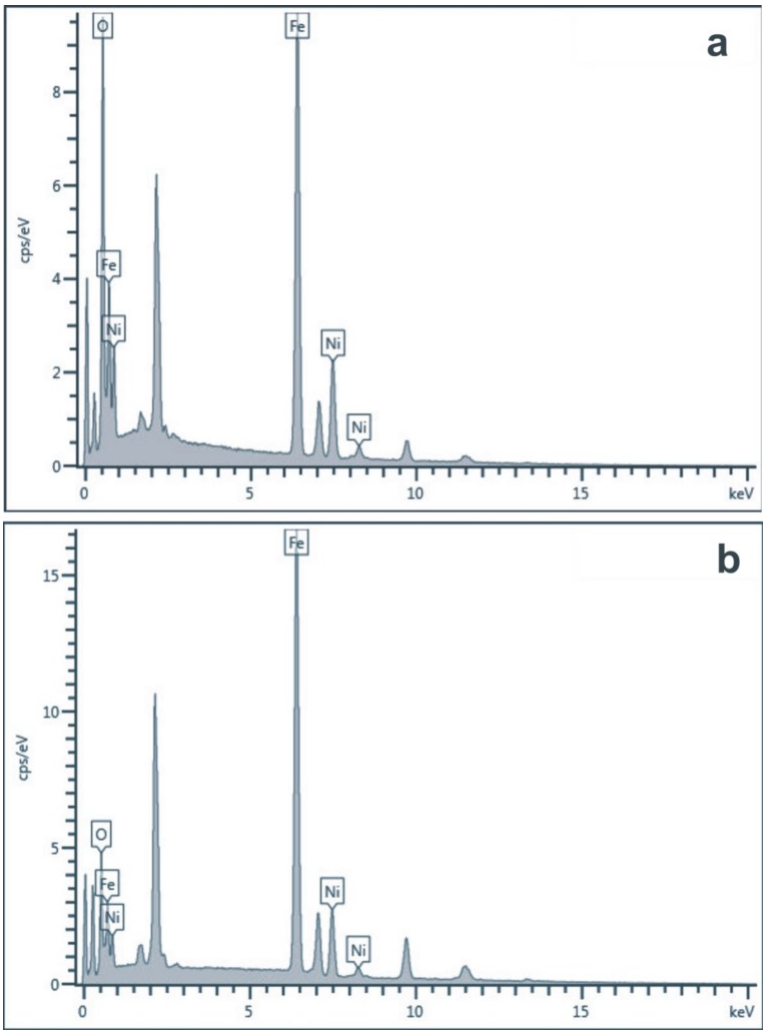

Figure 5.6: EDX spectra of samples (a) $n_C = 0$ and (b) $n_C = 1$.

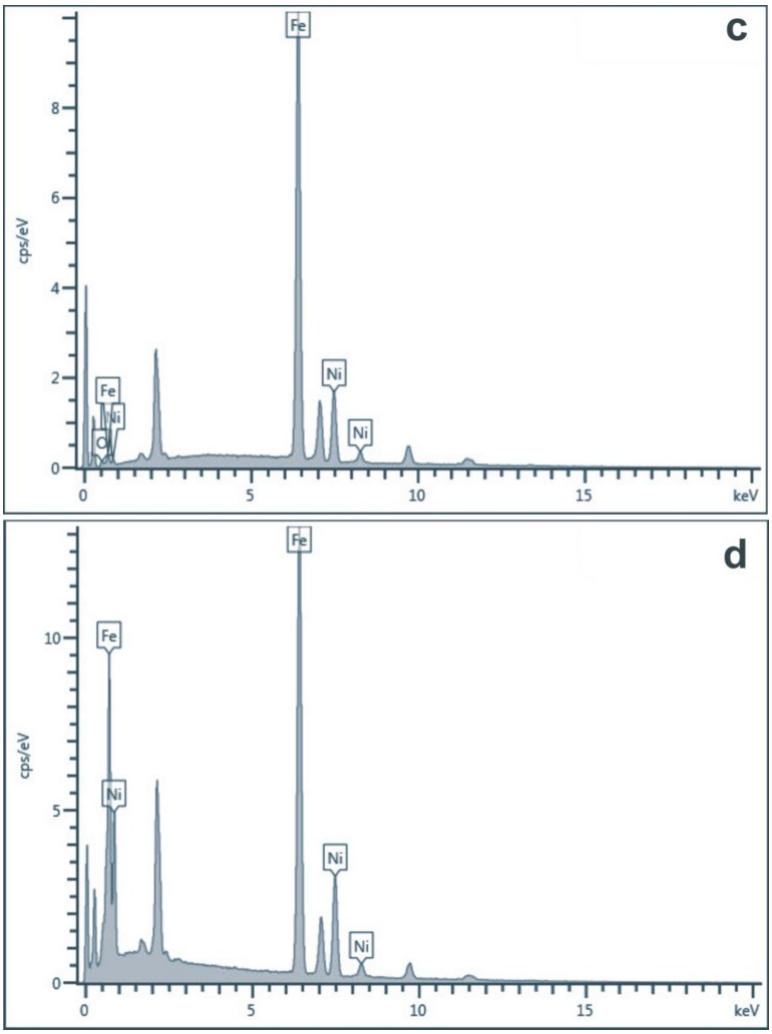

Figure 5.7: EDX spectra of samples (c) $n_C = 4$ and (d) $n_C = 5$.

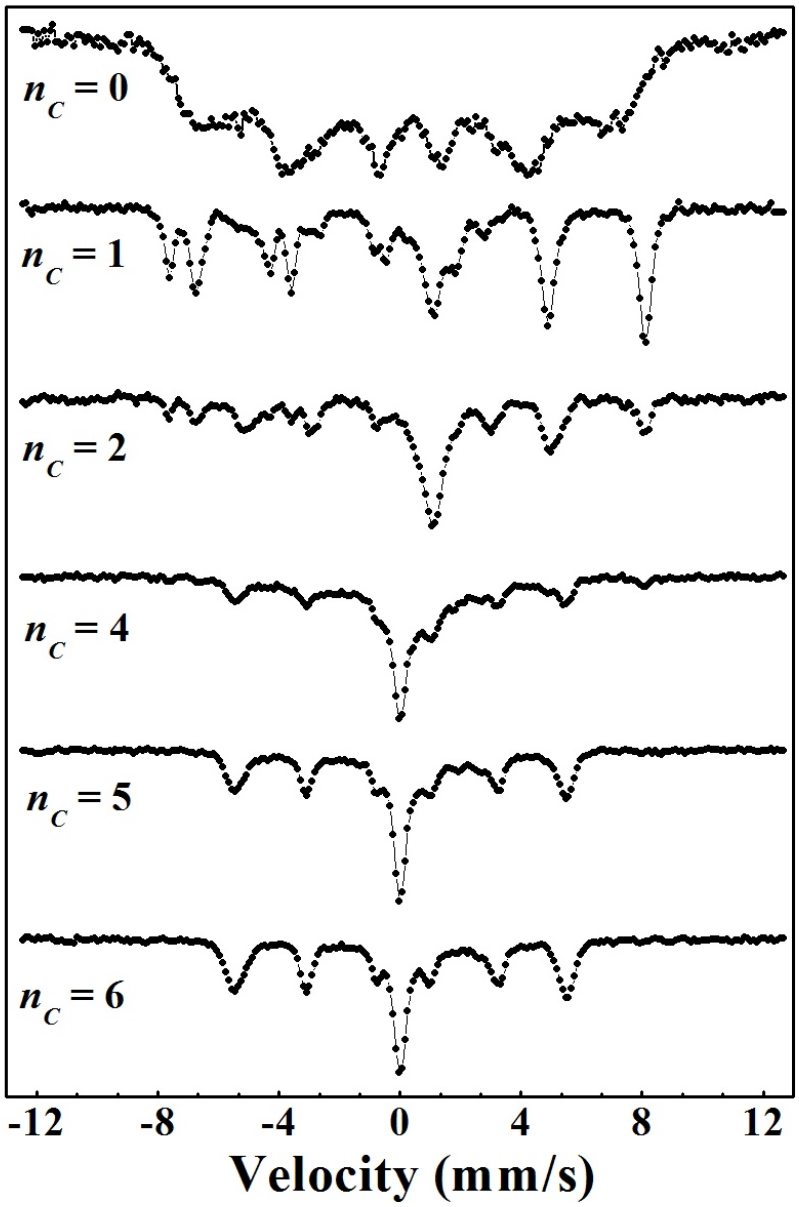

Figure 5.8: Mössbauer spectra of $NiFe_2O_4$ reduced with moles of activated charcoal n_C = 0, 1, 2, 4, 5 and 6.

shows how the spectra develop with increasing reduction by activated charcoal. The spectra for partially reduced samples from $n_C = 1$ to 4 appear to show more complex Fe environments as the samples evolve from spinel structure. At a reduction ratio for $n_C > 2$, the less complex Mössbauer spectra are obtained which we associate with the unique formation of fcc and bcc NiFe phases. The fitted Mössbauer spectra for $n_C = 0$, 5 and 6 are presented in Figure 5.9. Table 5.2 gives the values of the fitted parameters. The doublets in the reduced samples account for the coordination of Fe^{3+} and Fe^{2+} at both sites. As before the as-prepared $NiFe_2O_4$ Mössbauer spectrum was best fitted with two sextets corresponding to tetrahedral A- and octahedral B-sites. The hyperfine magnetic field B_{hf} values of 239 kOe and 420 kOe are consistent with α-Fe with comparable isomer shifts δ of 0.339 mm/s and 0.272 mm/s associated with Fe^{3+} ions [22, 20, 65]. The slightly smaller value of the isomer shifts at B-sites is due to larger covalency. The low quadrupole splitting values at both sites is indicative of the cubic symmetry around the Fe^{3+} ions [66]. The added doublet D accounts for the superparamagnetic relaxation effects due to the nano-size of the sample. Three sextets C_1, C_2 and C_3 are required to fit the spectra for $n_C = 5$ and two sextets C_1 and C_2 for $n_C = 6$ which we associate with the bcc and fcc phases. The high field components C_1 has a B_{hf} value of 339 kOe and 345 kOe which is attributed to the bcc FeNi and the lower field components C_2 has a value of 325 kOe and 327 kOe attributed to the fcc phase [63, 67] for $n_C = 5$ and 6 respectively. Sextet C_3 accounts for the small mixed phase denominated by fcc phase with a B_{hf} value of 274 kOe. These results are close to reported values of 343 kOe, 320 kOe and 273 kOe for an FeNi alloy [20, 63, 68]. The isomer shift values obtained for the fully reduced samples are significantly different and appear to confirm change from Fe^{3+} to Fe^{2+} [69].

5.2.4 Magnetization measurements

Room temperature magnetic hysteresis loops of the parent sample, nanocomposites and NiFe alloys recorded in applied magnetic fields of up to 50 kOe are presented in Figure 5.10. Magnetic properties such as coercivity (H_C) and saturation magnetization (M_S) were calculated from the hysteresis loops. The obtained data are

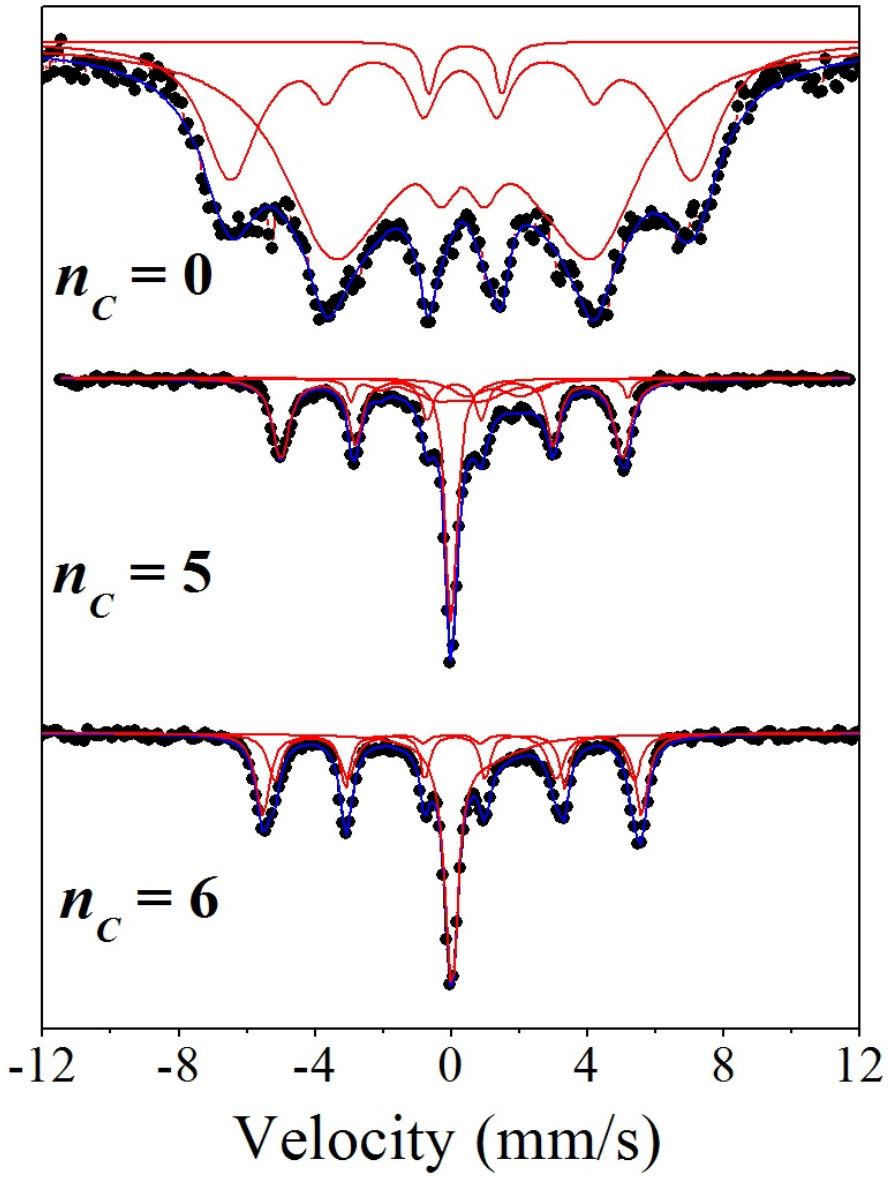

Figure 5.9: Fitted Mössbauer spectra of $NiFe_2O_4$ nano-ferrite at $n_C = 0$, 5 and 6.

Table 5.2: Mössbauer parameters include hyperfine field (B_{hf}), isomer shifts (δ), quadrupole splitting (Δ_{EQ}), line widths (LW), fraction populations (f) and reduced chi^2 (c^2) of Fe ions of the parent sample and alloy composite at $n_C = 5$ and 6 of activated charcoal.

n_C	Sub-pattern	B_{hf} (kOe)	δ(mm/s)	Δ_{EQ}(mm/s)	LW(mm/s)	f(%)	c^2
		±3	±0.009	±0.002	±0.01	±0.6	
0	A	293	0.339	0.005	0.58	68.0	0.7825
	B	420	0.272	0.014	0.49	30.0	
	D	-	0.420	2.150	0.23	1.9	
5	C_1	339	0.049	-0.048	0.19	39.5	1.3207
	C_2	325	0.900	-0.737	0.44	11.3	
	C_3	274	0.786	0.455	1.16	24.1	
	D	-	-0.017	0.139	0.22	25.0	
6	C_1	345	0.067	-0.042	0.16	35.1	0.9815
	C_2	327	0.053	0.032	0.19	24.5	
	D	-	0.540	1.080	-	40.4	

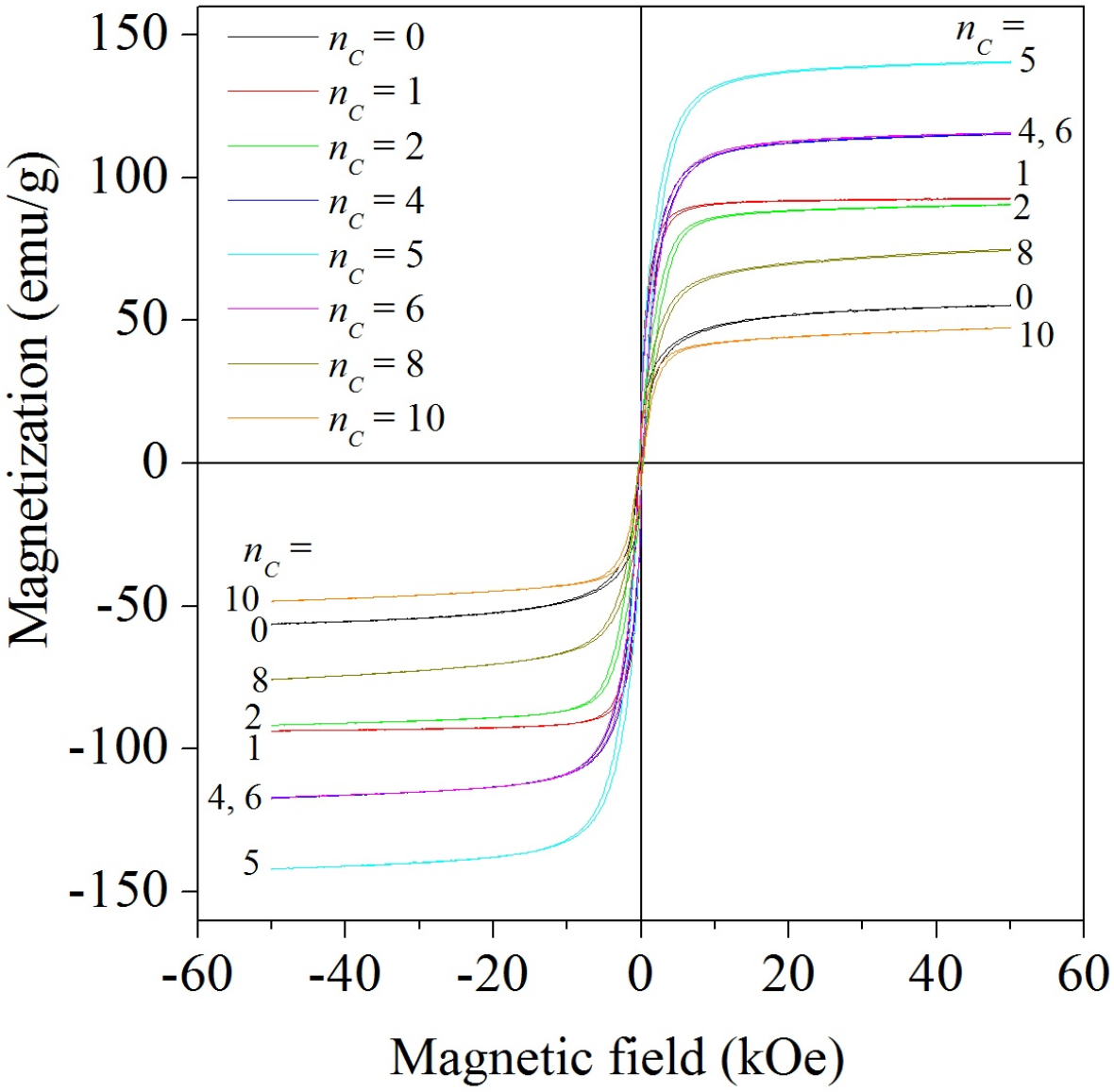

Figure 5.10: Magnetic hysteresis loops for the as-prepared $NiFe_2O_4$, $NiFe_2O_4$/NiFe nanocomposites and NiFe alloy samples measured at room temperature.

given in Table 5.3. The samples exhibit soft magnetic hysteresis loops and the maximum magnetization at 50 kOe is herewith regarded as the estimate for saturation magnetization at a particular temperature. The as-prepared nano-ferrite has a coercivity of 0.10 kOe and saturation magnetization of 57 emu/g. The variation of the magnetization and coercivity with n_C ratios of activated charcoal are presented in Figure 5.11. The reduction of $NiFe_2O_4$ nano-ferrite appear to enhance the magnetizations and coercive fields. The magnetization attain a maximum value of 141 emu/g at $n_C = 5$ while the coercive field has a maximum of 0.31 kOe at $n_C = 2$. For $n_C > 5$ magnetization decreases which we associate with the onset of the NiFe bcc and fcc phases with weaker internal hyperfine fields as deduced from Mössbauer spectroscopy. Higher magnetization and coercive fields are therefore obtained in the $NiFe_2O_4$/NiFe nanocomposites which begin to decline as inter metallic NiFe phase begins to dominate more and more. Low temperature measurements were also performed on the cryogen free measurement system. Typical hysteresis loops obtained at 4 K are presented in Figure 5.12. The data deduced from the hysteresis loops are presented in Table 5.4. Figure 5.13 shows the coercivity and saturation magnetization dependence on temperature. The magnetization are observed to increase gradually with decreasing temperature. A more significant increase in coercive fields is observed in the $NiFe_2O_4$ nano-ferrite which appears to follow the typical behaviour for the spinel ferrites [70, 71]. The nanocomposite sample $NiFe_2O_4$/NiFe at $n_C = 4$ had the highest magnetization below about 100 K compared to the parent nano-ferrite or fully reduced sample. The coercivity of the NiFe alloy seems to be slightly affected by temperature change compared to the nanocomposite or the $NiFe_2O_4$.

Table 5.3: Coercive fields H_C and saturation magnetization M_S obtained at room temperature for different amounts of activated charcoal n_C.

n_C	H_C (kOe)	M_S (emu/g)
	± 0.03	± 1
0	0.10	57
1	0.15	93
2	0.31	91
4	0.14	116
5	0.18	141
6	0.12	116
8	0.18	75
10	0.21	48

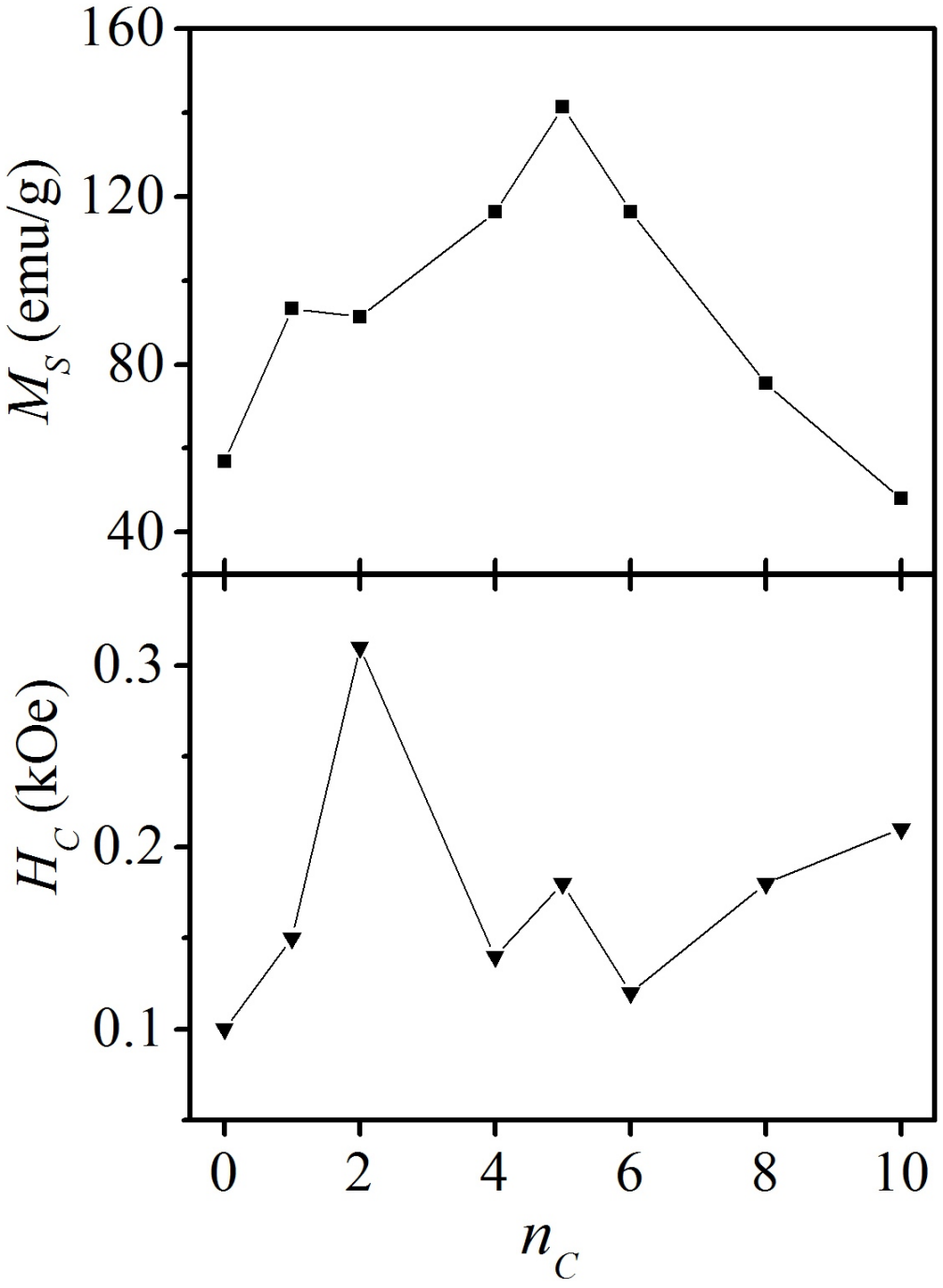

Figure 5.11: Variations of saturation magnetization M_S and coercivity H_C with n_C.

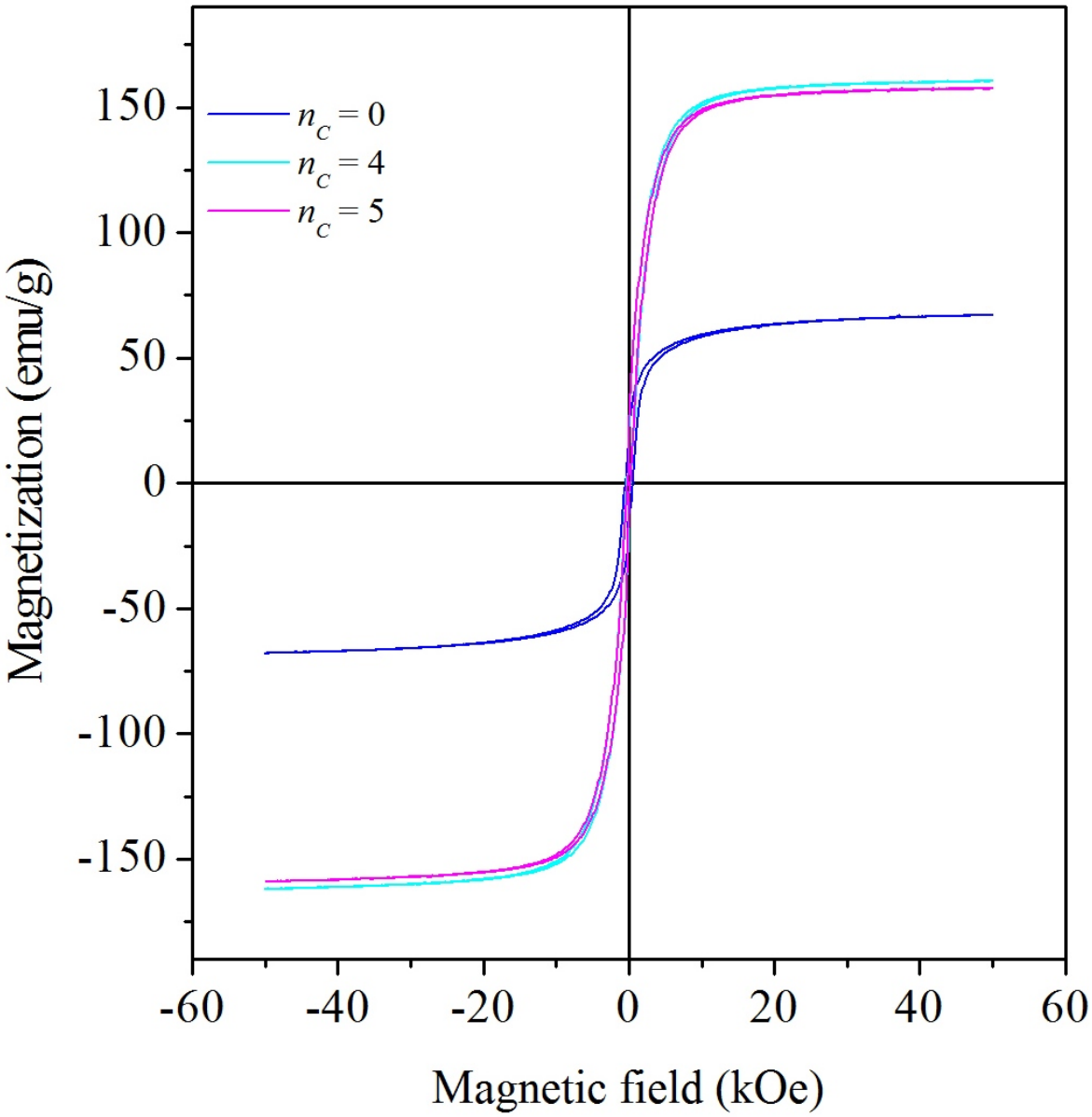

Figure 5.12: Magnetic hysteresis loops for as-prepared $NiFe_2O_4$ nano-ferrite, $NiFe_2O_4$/NiFe nanocomposite and NiFe alloy samples measured at 4 K.

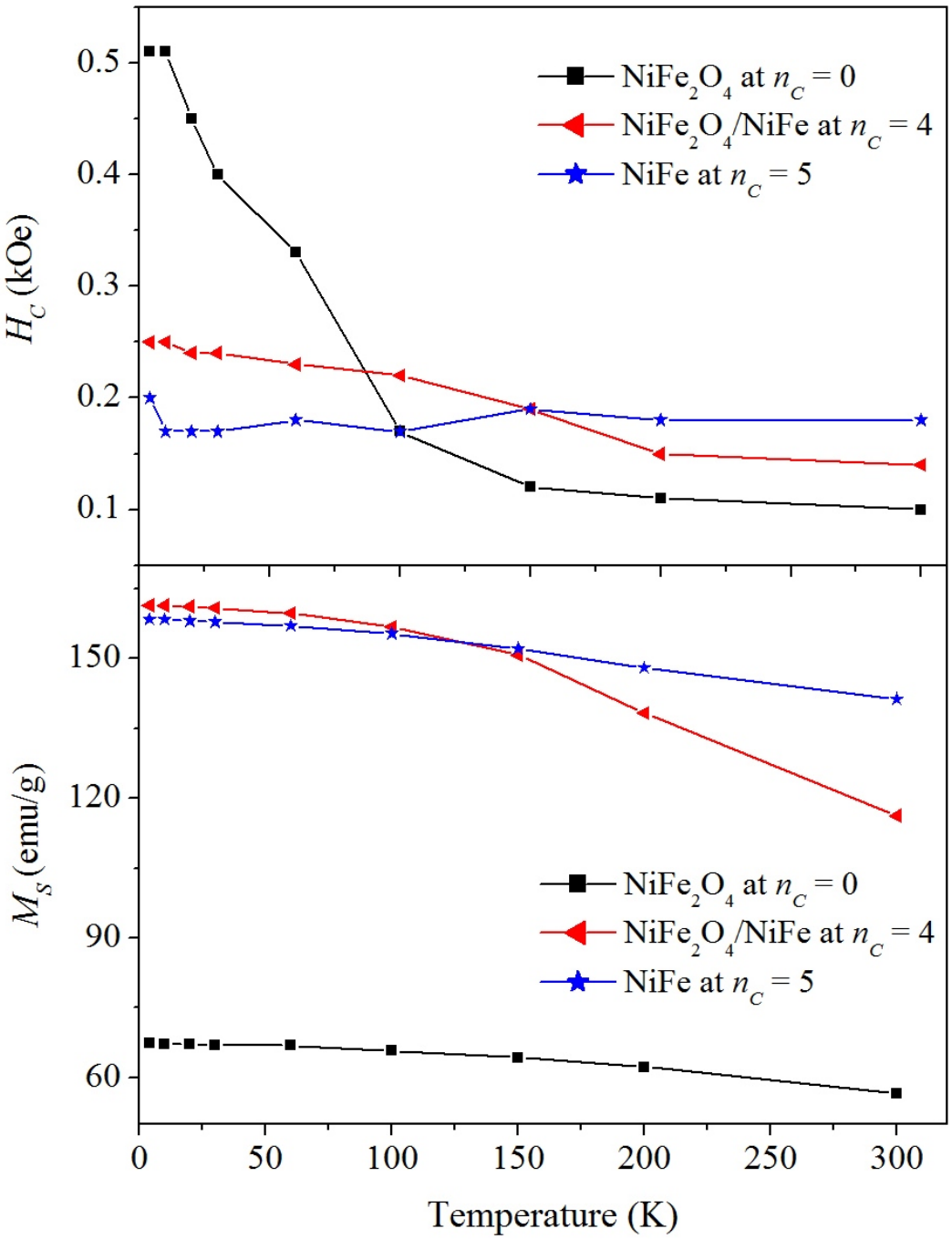

Figure 5.13: Coercivity H_C and saturation magnetization M_S dependence on temperature T for as-prepared $NiFe_2O_4$ nano-ferrite, $NiFe_2O_4$/NiFe nanocomposite and NiFe alloy.

Table 5.4: Coercive fields H_C and saturation magnetization M_S measurements at low temperature T obtained for $NiFe_2O_4$, $NiFe_2O_4$/NiFe and NiFe at $n_C = 0$, 4 and 5 respectively.

	$n_c = 0$		$n_c = 4$		$n_c = 5$	
T(K)	H_C (kOe)	M_S (emu/g)	H_C (kOe)	M_S (emu/g)	H_C (kOe)	M_S (emu/g)
	±0.07	±0.9	±0.05	±2	±0.09	±1
4	0.51	67.5	0.25	161	0.20	158
10	0.51	67.2	0.25	161	0.17	158
20	0.45	67.1	0.24	161	0.17	158
30	0.40	67.1	0.24	161	0.17	158
60	0.33	66.9	0.23	160	0.18	157
100	0.17	65.8	0.22	157	0.17	155
150	0.12	64.3	0.19	151	0.19	152
200	0.11	62.3	0.15	138	0.18	148
300	0.10	56.7	0.14	116	0.18	141

5.3 Conclusions

Nanocomposites of $NiFe_2O_4$/NiFe and NiFe alloy were successfully synthesized by the reduction of $NiFe_2O_4$ nano-ferrite using activated charcoal. XRD measurements showed fully reduced samples of the NiFe alloy for $n_C = 5$ and 6 of activated charcoal. The XRD peak for the reduced samples were indexed to the bcc α-Fe and fcc γ-Fe lattices for the NiFe alloy. Fitted Mössbauer analysis for $n_C = 5$ and 6 show high hyperfine magnetic fields associated with the bcc phase while the lower field component is associated with the fcc phase of NiFe. High resolution transmission electron microscopy measurements showed different morphology of the parent sample to the reduced samples. The surface morphology for $n_C = 5$ and 6 have their particles closely packed and compacted which we attribute to the presence of NiFe alloy phase with high density of fcc packing. ^{57}Fe Mössbauer spectroscopy results at room temperature show transformation to lower hyperfine fields for the NiFe phase. The isomer shift values also indicate change to Fe^{2+} from Fe^{3+} in the spinel phase. Room temperature measurements of magnetization showed enhanced saturation magnetizations. The $NiFe_2O_4$/NiFe nanocomposites exhibited the highest magnetization at low temperatures with an optimum value of 161 emu/g at 4 K for $n_C = 4$. The coercivity of the fully reduced samples was found to be less dependent on temperature.

Chapter 6

General conclusions

Bi-magnetic nanocomposites of $CoFe_2O_4/CoFe_2$, $NiFe_2O_4$/NiFe and intermetallic powders of $CoFe_2$, NiFe alloys were successfully synthesized by reduction of $CoFe_2O_4$ and $NiFe_2O_4$ nano-ferrites respectively. The ferrites were reduced with activated charcoal (fine granular carbon powder) at 900 °C for 3 hours. 0.5 g of $CoFe_2O_4$ or $NiFe_2O_4$ was each reacted with different molar ratios n_C of activated charcoal to produce their respective nanocomposites and alloys. The choice of $CoFe_2O_4$ and $NiFe_2O_4$ nano-ferrites was based on significant differences in anisotropy due to Co and Ni ions. The synthesized samples were studied using X-ray powder diffraction (XRD), high resolution transmission electron microscope (HRTEM), high resolution scanning electron microscope (HRSEM), ^{57}Fe Mössbauer spectroscopy, LakeShore vibrating sample magnetometer (VSM) and mini cryogen free system (CFS). XRD measurements of the nano-ferrites showed a single phase spinel structure. Structural transformations from spinel to alloy phases were observed. The reduction of $CoFe_2O_4$ yielded the $CoFe_2$ alloy at activated charcoal molar ratio of $n_C = 6$. The fully reduced NiFe alloy was obtained at $n_C = 5$. The HRTEM and HRSEM measurements showed clear differences between the morphology of the parent nano-ferrites and the reduced samples. ^{57}Fe Mössbauer spectra measurements on the reduced samples revealed the presence of mixed phases in the nanocomposites. A small amount of mixed phase was detected for $CoFe_2$ alloy at $n_C = 6$ and for NiFe at $n_C = 5$. These phases could not be detected by XRD. This confirms the power of Mössbauer spectroscopy in revealing minute changes in local Fe environments. Higher hyperfine

fields at tetrahedral and octahedral sites are obtained in the parent nano-ferrites compared to the alloy phases. The isomer shifts show change from Fe^{3+} to Fe^{2+} due to the reduction effect of activated charcoal. Magnetization measurements of $CoFe_2O_4/CoFe_2$ nanocomposites in saturating fields of 50 kOe showed significant enhancement of magnetic properties. Significant enhancement of the magnetization was achieved as the $CoFe_2O_4/CoFe_2$ nanocomposites transform from hard to soft magnetic phases. The coercivity of the fully reduced samples is observed to be less dependent on temperature. The saturation magnetization increases with decrease in temperature. The results show the successful synthesis of a nanocomposite with a hard and soft magnetic phases. The XRD measurements of the fully reduced samples of $NiFe_2O_4$ showed that the samples consist of the bcc α-Fe and fcc γ-Fe lattice structures of NiFe alloy in coexistence. The surface morphology for $n_C = 5$ and 6 have their particles closely packed and compacted which is attributed to the presence of NiFe alloy phase and the high density of fcc packing. Fitted Mössbauer analysis for $n_C = 5$ and 6 moles has a high hyperfine magnetic field associated with the bcc while the lower field component is associated with the fcc phase of NiFe. Room temperature measurements of magnetization showed best enhanced magnetization of NiFe alloy for $n_C = 5$ while low temperature measurements showed best enhanced magnetization for $NiFe_2O_4$/NiFe nanocomposite for $n_C = 4$. The coercivity of the fully reduced samples are also observed to be less dependent on temperature. The saturation magnetization showed significant dependence on temperature.

6.1 Future work

Our study has shown improved magnetizations of the nanocomposites compared to the parent nano-ferrites or the alloys. The reduction process can also be performed using hydrogen gas. The hydrogen reduction process is expected to provide purer samples without the combustive effect from activated charcoal. Unfortunately a facility for hydrogen reduction was not available. Further investigations by electrical, zero field cooling and field cooling measurements of the samples stands to provide further details for the microwave and high frequency properties. Our investigations

suggests how the different anisotropy of Co and Ni affects the amounts of activated charcoal needed to fully reduce $CoFe_2O_4$ and $NiFe_2O_4$ nano-ferrites to $CoFe_2$ and NiFe alloys respectively. The results of the study have been distilled into two research papers which are currently under review [72, 73]. Further investigations on the reduction of the ferrites of other transition metals is required to firmly ascertain the effects of anisotropy on reduction and sample properties. Transition metal alloys are useful catalysts. They can be used as catalyst in the synthesis of carbon nano tubes. Preliminary studies on the effectiveness of the use of the synthesized alloy powders as catalysts for nano-tubes synthesis are in progress.

Bibliography

[1] P. Lorrain, F. Lorrain, S. Houle, *Magneto-Fluid Dynamics*, Springer Science + Business Media, 1st Ed (2006) 4-13.

[2] V. G. Harris, N. C. Koon, C. M. Williams, Q. Zhang, M. Abe, J. P. Kirkland, Appl. Phys. Lett. **68** (1996) 15.

[3] S. Akhter, D. P. M. Saha, M. Mamun and A. Parveen, Materials Sciences and Applications **2** (2011) 1675.

[4] J. Z. Msomi and T. Moyo, Hyperfine Interact. **176** (2007) 93.

[5] H. Lawrence Van Vlack, *Elements of Material Science and Engineering*, 6^{th} Ed. Addison-Wesley Co.Publishers Ltd., New York (1989) 450-459.

[6] K. Landfester and L. P. Ramirez, J. Phys. Condens. Mater. **15** (2003) 1345.

[7] A. Goldman, *Modern ferrite Technology*, 2^{nd} Ed. Springer (2010) 9-14, 17-21, 52, 55.

[8] P. Sivakumar, R. Ramesh, A. Ramanand, S. Ponnusamy, C. Muthamizhchelvan, J. Mater Res. **46** (2011) 2204-2207.

[9] V. G. Roullin, J. R. Deverre, L. Lemaire, F. Hindre, M. C. V. Julienne, R. Vienet, J. P. Benoit, Eur. J. Pharm. Biopharm. **53** (2002) 293.

[10] J. Z. Msomi, *Synthesis, Structural and Magnetic Properties of Bulk and Nano-sized (Zn, Cd, Cu)*$_{0.5}Ni_{0.5}Fe_2O_4$ *and* $NiFe_2O_4$ *Ferrites,* University of KwaZulu-Natal (2007) PhD thesis.

[11] P. P. Masina, *Magnetic Properties of Magnesium-Zinc Nanoferrites and Tetracycline-ferrite Nanocomposites* University of KwaZulu-Natal (2013) MSc thesis.

[12] A. Lu, E. L. Salabas, F. Schüth, Angew. Chem. Int. Ed. **46** (2007) 1222-1244.

[13] A. Mansour, Turk J. Phys. **28** (2004) 391-396.

[14] R. Roy, R. A. Roy, D. M. Roy, Mater. Let. **4(8-9)**(1986) 323-328.

[15] C. C. H. Pedro, S. G. Kestur, W. Fernando, Mater. Res. **12** (2009) 1-39.

[16] F. E. Kruis, H. Fissan, A. Peled, J. Aerosol Sci. **29 (5-6)**(1998) 511-535.

[17] R. Y. Muhammad, P. Liqing, J. Qurat-ul-ain, I. Z. Muhammad, Y. Lihong, J. Nanopart. Res. **14** (2012) 1189.

[18] I. S. Jurca, N. Viart, C. Meny, C. Ulhaq-Bouillet, P. Panissod, G. Pourroy, J. Surf. Sci. **529** (2003) 215-222.

[19] R. Sayed Hassan, C. Meny, N. Viart, C. Ulhaq, G. Versini, J. L. Loison, G. Pourroy, New J. Phys. **9** (2007) 364.

[20] F. H. Rawwagah, A. F. Lehlooh, S. H. Mahmood, S. Mahmoud, A. R. El-Ali, M. R. Said, I. Odeh, I. Abu-Aljarayesh, Jord. J. Phys. **5** (2012) 9-14.

[21] X. G. Liu, D. Y. Geng, C. J. Choi, J. C. Kim, J. Z. D. Zhang, Nanopart. Res. **11** (2009) 2097-2104.

[22] G. C. P. Leite, E. F. Chagas, R. Pereira, R. J. Prado, A. J. Terezo, M. Alzamora, E. B. Saitovitch, J. Magn. Magn. Mater. **324** (2012) 2711-2716.

[23] J. Hu, A. Chen, J. Advn. Mater. Res. **486** (2012) 65-69.

[24] J. M. D. Coey, *Magnetism and Magnetic Materials*, Cambridge University Press (2010) 7-8, 24-25, 50-56, 63, 195-203, 330, 329.

[25] A. P. Guimaräes, *Magnetism and Magnetic Resonance in Solids*, John Wiley & Sons, Inc. (1998) 12-18, 27-35, 47-49, 119-141.

[26] C. M. Hurd, *Contemporary Physics* **23 No. 5** (1982) 469.

[27] C. Kittel, *Introduction to Solid State Physics*, 2nd Ed. John Wiley and Sons (1956) 207.

[28] M. M. Bruce, *Hitchhiker's Guide to Magnetism*, Environmental Magnetism Workshop held 5-8 June 1991 at the Institute for Rock Magnetism, University of Minnesota USA.

[29] C. Kittel, *Introduction to Solid State Physics*, 7th Ed. John Wiley and Sons (1996) 424-425.

[30] C. D. Graham, Cullity, *Introduction to Magnetic Materials*, 2nd Ed. Wiley-IEEE New York (2008) 116.

[31] M. Farle, Rep. Prog. Phys. **61** (1998) 755.

[32] W. F. Brown, Phys. Rev. **58** (1940) 736.

[33] A. B. Gadkari, T. J. Shinde, P. N. Vasambekar, Mater. Chem. Phys **114** (2009) 505-510.

[34] H. M. I. Abdallah, T. Moyo, J. Alloys Comp. **562** (2013) 156-163.

[35] D. B. Cullity, *Elements of X-ray Diffraction*, 2nd Ed. Addison- Wesley publishing company (1977) 356-102.

[36] K. Thomas, *lecture note on Practical X-Ray Diffraction*, School of Materials Engineering, Purdue University Indiana.

[37] www.cryogenic.co.uk

[38] N. N. Greenwood and T. C. Gibb, *Mössbauer Spectroscopy,* Chapman and Hall, London, UK (1971) 16-65.

[39] G. K. Wertheim, *Mössbauer Effect: Principle and Applications,* Academic Press Inc., New York, London (1964) 3-82.

[40] www.rsc.org

[41] M. I. Hafiz Abdallah, *Synthesis, Magnetic and Electrical Characterizations of Nanoparticle Ferrites,* University of KwaZulu-Natal (2012) PhD thesis.

[42] www.chemwiki.ucdavis.edu

[43] J. M. D. Coey, *lecture note on Magnetic Resonance*, Dublin (2007).

[44] www.serc.carleton.edu

[45] G. Liping, S. Xiangqian, S. Fuzhan, L. Mingquan, Z. Yongwei, J. Sol-Gel Technol. **58** (2011) 524-529.

[46] C. H. Park, J. G. Na, N. H. Heo, S. R. Lee, J. Kim, K. Park, J. Magn. **3(1)** (1998) 31-35.

[47] M. V. C. Sastri, R. P. Viswanath, B. Viswanathan, Int. J. Hydrogen Energy, **7** (1982) 951-955.

[48] E. Tirosh, G. Shemer, G. Markorvich, Chem. Mater. **18** (2006) 465-470.

[49] M. Mohan, V. Chandra, S. M. Sundar, J. Mater, Res. **23** No. 7 (2008) 0230.

[50] www.environmentalchemistry.com

[51] A. M. Gismelseed, H. M. Mohammed, H. M. Widatallah, A. D. Al-Rawas, M. E. Elzain, A. Yousif, J. Phys: Conf. Ser. **217** (2009) 012138.

[52] B. P. Rao, P. S. V. S. Rao, G. V. S. Murthy, K. H. Rao, J. Magn. Magn. Mater. **268** (2004) 315-320.

[53] D. van, Physica **86-88B** (1977) 955.

[54] B. J. Evans, S. P. Lu, AIP Conf. Proc. **34** (I976) 181.

[55] J. Nishimura, K. Nomura, Hyperfine Int. DOI 10.1007/s10751-011-0472-8.

[56] C. E. Johnson, M. S. Ridout, T. E. Cranshaw, Proc. Phys. Soc. **81** (1963) 1079-1090.

[57] L. Xing-Hua, X. Cai-Ling, Q. Liang, W. Tao, L. Fa-Shen, Nanoscale Res. Lett. **5** (2010) 1039-1044.

[58] S. M. A. Radmanesh, S. A. E. Seyyed, J. Supercond. Nov. Magn. **26** (2013) 2411-2417.

[59] Q. A. Pankhurst, R. J. Pollard, Phys. Rev. Lett. **67** (1991) 248.

[60] Z. J. Gu, X. Xiang, G. L. Fan, F. Li, Phys. Chem. **C 112** (2008) 18459.

[61] J. Bauer, M. Seeger, A. Zern, J. Appl. Phys. **80** (1996) 1667-1673.

[62] X. L. Dong, Z. D. Zhang, X. G. Zhao, Y. C. Chuang, J. Mater. Res. **14** (1999) 398-406.

[63] J. F. Valderruten, G. A. Pérez Alcázar, J. M. Greneche, J. Appl. Phys. Condens. Matter **20** (2008) 485304.

[64] Y. Zhang, T. Zuo, Y. Cheng, P. K. Liaw, J. Sci. Rep. **38** (2013) 1455.

[65] A. Guittoum, A. Layadi, H. Tafat, A. Bourzam, N. Souam. O. Lenoble, J. Phil. Magn. **88** (2009) 1085-1098.

[66] S. S. Umare, R. S. Ningthoujam, S. J. Sharma, S. S. S. Kurian, N. S. Gajbhiye, Hyperfine Interact. **184** (2008) 235-243.

[67] R. R. Rodriguez, J. L. Valenzuela, J. A. Tabares, Hyperfine Interact. DOI 10.1007/s10751-013-0834-5.

[68] D. A. Lehlooh, H. S. Mahmood, Hyperfine Interact. **139-140** (2002) 387-392.

[69] M. Y. Hassan, M. M. El-Desoky, H. Masuda, S. Kubuki, T. Nishida, Hyperfine Interact. DIO 10.1007/s10751-011-0478-2.

[70] K. Mazz, A. Mumtaz, S. K. Hasanain, M. F. Bertino, J. Magn. Magn. Mater. **322** (2010) 2199-2202.

[71] D. Chunhui, W. Gaoxue, G. Dangwei, J. Changjun, X. Desheng, Nanoscale Res. Lett. **8** (2013) 196.

[72] *Enhanced magnetic properties of $CoFe_2O_4/CoFe_2$ nanocomposites and $CoFe_2$ alloy*, Itegbeyogene P. Ezekiel, Thomas Moyo, Hafiz M. I. Abdallah.

[73] *Structural and magnetic characterizations of $NiFe_2O_4/NiFe$ bi-magnet and NiFe alloy synthesized from thermal reduction $NiFe_2O_4$ nano-ferrite*. Itegbeyogene P. Ezekiel, Thomas Moyo, Hafiz M. I. Abdallah .